The High Resolution Imaging Channel of the SIMBIO-SYS suite aboard the BepiColombo mission to Mercury

Ing. Michele Zusi

Ph.D. thesis

2009

Aerospace Engineering Department

University of Naples – Federico II

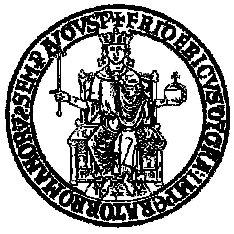

CONTENTS

Introduction ..... **i**

First chapter

BepiColombo space mission to Mercury

1.1 Scientific interest in studying terrestrial planets 1
1.2 A peculiar terrestrial planet: Mercury 3
1.3 From Mariner-10 to MESSENGER: Mercury exploration evolution 8
1.4 Bepicolombo space mission overview 11

Second chapter

SIMBIO-SYS suite and the high spatial resolution camera

2.1 SIMBIO-SYS overview 17
2.2 The High spatial Resolution Imaging Channel (HRIC) 20
2.2.1 Scientific objectives *20*
2.2.2 Optical-mechanical design *25*
2.2.3 Images acquisition and transmission *29*

Third chapter

HRIC imaging performances

3.1 The Radiometric Model of the HRIC 31
3.1.1 Basic theory *31*
3.1.1.1 Mercury Radiance 31
3.1.1.2 Image signal 38
3.1.1.3 Noise 46
3.1.1.4 Spurious charge 51
3.1.2 The Radiometric Model as HRIC performance analysis tool *52*
3.2 HRIC Simulator 57
3.2.1 HRIC optical PSF, MTF and image quality *57*
3.2.2 System MTF *65*
3.2.3 The simulator *68*
3.2.3.1 Input image 69
3.2.3.2 System MTF estimation 70
3.2.3.3 Noise 72

3.2.3.4 Degradation evaluation: Relative Edge Response (RER) ... 73
3.2.4 HRIC imaging performance analysis ... 75
3.2.4.1 Real Image ... 76
3.2.4.2 Synthetic scenarios ... 78
3.2.4.2.1 Impulse ... 78
3.2.4.2.2 Edge ... 81
3.2.4.2.3 Bars ... 84
3.2.4.3 Relative Edge Response (RER) simulation ... 89
3.3 Analyses of HRIC key optical elements ... 93
3.3.1 HRIC filters ... 94
3.3.1.1 Filters optical specifications and optical performance analysis ... 95
3.3.1.2 Filter ghosts: definition and analysis ... 97
3.3.2 HRIC external baffle ... 100
3.3.2.1 HRIC external baffle optical response ... 101

Fourth chapter

HRIC science operations

4.1 HRIC operation definition strategy ... 106
4.2 HRIC operative modes ... 107
4.2.1 Mode 1: Panchromatic High Resolution Imaging ... 108
4.2.2 Mode 2: Panchromatic High Resolution Imaging (low compression) ... 109
4.2.3 Mode 3: Panchromatic Low Resolution Imaging ... 110
4.2.4 Mode 4: Broadband Filters High Resolution Imaging ... 111
4.2.5 Mode 5: Full Acquisition ... 112
4.3 Coverage and image quality analysis ... 113
4.4 Data volume distribution simulation ... 116
4.4.1 Starting assumptions ... 116
4.4.2 Simulation results ... 120
4.4.3 Stressing operative conditions ... 126

Conclusions ... 128

Bibliography ... 132

Glossary ... 136

A Colui che ha creato l'universo intero...

perché attraverso le scoperte di ogni giorno

ci mostra la vastità dei Suoi pensieri.

Introduction

On May 10, 1946 a cosmic radiation experiment was launched by the USA on a V2: it was the first scientific exploration from space. In the same year, the first image of Earth was taken by a 35-millimeter motion picture camera riding on a V2 missile. These two suborbital experiments represented the beginning of the space exploration programme.

The USSR's Sputnik-1 (launch on 04/10/1957) was the first scientific man-made object to orbit the Earth. By means of two radio transmitters (20 and 40 MHz), which emitted "beeps" that could be heard by radios around the globe, it provided to the Russian laboratory the measure of ionosphere electron density, temperature and pressure.

Russian success led to an escalation of the American space program (Explorer-1 launch on 31/10/1958), due to the geopolitical rivalries between USA and URSS during the Cold War.

American Luna-2 probe (1959) was the first artificial object to reach another celestial body (the Moon), while the first automatic landing was performed by Luna-9 (1966).

American Luna programme demonstrated the possibility of interplanetary journey to reach Solar System celestial bodies. This aerospace engineering success led to an increased scientific interest in the space exploration programme thanks to the possibility to perform more complete and precise scientific measurements of celestial body properties. This incredible opportunity pushed the development of the modern planetology science and the progress of Solar System formation and evolution models.

With the Mariner programme (10 robotic probes – last two became the Voyager-1 and Voyager-2), the American space agency (National Aeronautics and Space Administration – NASA) started an ambitious project to investigate all the terrestrial planets of our Solar System. After some initial problems (probe 1, 2, 3 failed), the Mariner programme was a complete success: Mariner-4 was the first probe to successfully attempt a flyby manoeuvre around Mars; Mariner-5 analysed the Venus' atmosphere (Ultra-Violet scan) and sampled the solar particles and magnetic field fluctuations above the planet; Mariner-6 and Mariner-7 observed the surface of Mars; Mariner-9 was the first artificial satellite around

Mars; Mariner-10 was the first probe to use gravity assist (around Venus) to reach with three flybys the fleeting Mercury.

After the Mariner probes, the space exploration programme was extended including the other celestial bodies of the Solar System (Jupiter and Saturn with their satellite systems, Uranus, Neptune and Pluto), but maintaining a great attention on the terrestrial planets to perform comparative analysis on the evolution of these Earth-like bodies.

At present, many have been the missions towards Mars and Venus that have provided a lot of interesting information about their interior, surface and atmosphere. Conversely, after the Mariner-10 close approach, Mercury remained in a second rank for a lot of time due to the technological criticalities to develop a spacecraft able to remain in orbit around the planet (e.g., great solar gravitational perturbations, thermal and radiation constraints).

With the improvements of the aerospace engineering (e.g., launchers, electrical propulsion engines, solar-panel power support, etc.), the establishment of international partnership between space agencies (European Space Agency – ESA, NASA, Japanese Aerospace eXpolration Agency – JAXA and the new Indian and Chinese ones) and research institutes and the development of new mission definition approach (e.g., NASA Discovery Programme – smaller and cheaper missions) new opportunities to explore our Solar System raised.

In this context, MESSENGER and BepiColombo represent the return to the Mercury exploration:

- MESSENGER is the American probe launched in 2004, that will explore Mercury (for the first time) to perform measurements of the internal, superficial and atmospheric structure and composition and to analyse the magnetosphere dynamics;
- BepiColombo is the ESA's cornerstone mission planned at launch in 2014, that will characterise in detail the Mercury internal structure, superficial geological units, exosphere composition, gravity and magnetic field and polar deposits with unprecedented sensitivities and resolution.

The research activities presented in this thesis refer to the development of one of the most important scientific instrument aboard the European mission to Mercury (BepiColombo). It consists of the High Spatial Resolution Camera (HRIC), part of the SIMBIO-SYS (Spectrometer and Imagers for MPO Bepicolombo Integrated Observatory – SYStem) instrument suite, which will characterise in detail the surface geological units in order to supply key information to reconstruct the past superficial evolution of the planet due to endogenic and exogenic processes. In particular, HRIC will reveal short scale features like scarps, rims, graben, small craters etc. Moreover, high spatial resolution observations by HRIC will be of paramount importance to support the libration experiment to measure the anomalies in orbital and rotational motion of the planet.

In the first chapter, after a brief introduction on the scientific interest in studying terrestrial planets, with particular emphasis on their common origin and different destiny, the most interesting scientific themes on Mercury evolution are reported. Past and present exploration programmes to Mercury are, then, discussed: the three fly-bys of the American probe Mariner-10 in the early 70s, the present American MESSENGER mission (2004-2012) and the future European-Japanese mission BepiColombo. For each mission the scientific objectives and instrumentation are reported with particular emphasis on the European-Japanese one where the scientific instrument discussed in this thesis is accommodated.
In the second chapter, the core of the present thesis research theme is presented: after a brief introduction on planetary surface radiance principles, the mathematical description of an instrument radiometric model is discussed. The first analysed component is the photo-electron output signal with respect to the optical design, filter transmission properties and detector specification. In the following, all the noise terms at pixel and frame level are presented. Finally, some simulation results are reported to show the HRIC imaging system performance in terms of Signal-to-Noise-Ratio (SNR).
The most important tool developed during the Ph. D. research work is presented in the third chapter. It consists on a simulator by which it is possible to study instrument imaging performances directly on images. Starting from a mathematical description of the

instrument optical design, the previously described radiometric model, some post-processing algorithms and different types of (realistic or synthetic) input scenes, the instrument simulator is able to produce an estimation of the possible produced image. With this tool it is possible to evaluate the real imaging system performances by analysing the outputs of standard image features extraction algorithms (i.e., features loose). The third chapter reports also the results of the HRIC design optical performance analysis in terms of filter efficiency, ghosts and external baffle ray-trace.

The last chapter reports the study of the imaging system performances in terms of coverage and data volume production. In particular, the results of two developed tools based on ESA Mapping And Planning Payload Science (MAPPS) simulations are reported: the first tool is able to show the amount of allowed observations for a selected target during mission lifetime, with estimation of the quality of each observation in terms of Signal-to-Noise-Ratio (SNR). The second tool considers a representative operative scenario, with several scientific targets uniformly distributed on the planet surface, in order to estimate the HRIC data rate and the cumulative data volume production during the mission lifetime. Results of both tools are of paramount importance to support the definition of scientific operative strategies compatible with allocated resources of power and mass memory.

The scientific activity described in this thesis has been reported in national and international conferences. The obtained results have also been presented in many technical meetings related to the BepiColombo mission. Finally, part of the obtained results have been used to prepare refereed papers already published.

CHAPTER 1

BepiColombo space mission to Mercury

BepiColombo mission to Mercury is the next cornerstone mission of the European Space Agency. In this chapter we introduce the scientific interest in studying the terrestrial planets and Mercury, the innermost planet of our Solar System, in particular. The most interesting properties of Mercury are discussed, also based on results obtained by space exploration thanks to Mariner-10 in the past, and the presently ongoing MESSENGER mission. Finally we report the main steps in BepiColombo mission definition from the initial proposal in 1993 to the final acceptance in 2000 as ESA's 5th Cornerstone mission.

1.1 *Scientific interest in studying terrestrial planets*

Mercury, Venus, Earth and Mars are the innermost planets of our Solar System (SS). They are also known as *terrestrial planets* due to their rocky structure and thin atmosphere (Earth like bodies). In particular, *terrestrial planets* are characterised by [1]:

1. roughly the same internal structure with a central metallic core, mostly iron surrounded by a silicate mantle;
2. secondary atmosphere (the giant planets possess a primary atmosphere), containing heavy molecules (e.g.: CO_2, N_2, H_2O) originated by internal volcanism or comet impacts.
3. long periods of planetary activities (endogenic and exogenic processes) that have profoundly modified their internal structure and surface aspect such as volcanic activities, tidal stresses, meteoritic impacts, etc.

Formation of rocky planets was possible around second-generation stars due to the presence of heavy elements such as C, N, O, Si and Fe. Formation happened at the same time as the rest of the SS and involved matter at about 700-1500 K. Such warm environment produced a magma ocean (liquid rock) globally distributed on the proto-planet. Volatiles and gases (CO_2, CO, H_2O) were delivered by comets determining the formation of a primitive atmosphere (CO, CO_2, H_2O, and H_2) at 50-200 bar.
During accretion process, terrestrial planets experimented repeated comets and asteroids bombardment that increased the abundance of such chemical compounds. In particular:

- asteroids, formed inside the snow line[1] (5 Astronomical Unit – AU), that are rich in silicates, iron, nickel, carbon and water
- comets, formed behind the snow line, that contains significant amounts of H_2O, CO_2, and other ices with C, N, and O (the same molecules as in interstellar clouds).

In these chaotic conditions planets started to experiment endogenic processes like volcanism and, for some of them, tectonic displacements, that altered their surface aspect

[1] the minimum distance from the Sun at which water ice could have condensed, at about 150 K.

producing different geological units (e.g., hills, scarps, volcano domes etc.). Volcano eruptions also influenced the atmosphere enriching it with gases like water vapour (H_2O), carbon dioxide (CO_2) sulphur dioxide (SO_2) or hydrogen sulphide (H_2S), methane (NH_4), nitrogen oxide (NO_x), etc.

This evolutionary phase took several million years and involved planet positioning in the SS (depending on their size), impactors flux intensity and magnitude, Sun corona activities, compound distribution in the SS primordial nebula, intensity and length of endogenic processes etc., leading to different planet configurations: Mercury warm surface, Venus acid atmosphere, Mars dry atmosphere and Earth life-supporting environment.

Another important aspect about the *terrestrial planets* evolution regards the origin, evolution and diffusion of life. After planets consolidation (end of accretional process and surface solidification), all *terrestrial planets* had the right chemical ingredients to allow life origin and evolution. However, not all of them presented the right combination of planet size, solar distance (and so solar irradiance) and atmosphere composition and/or had experienced the same endogenic and exogenic processes. As a result, even if with similar life-support requirements, life diffusion and evolution have been strongly conditioned. Present knowledge about life forms indicates that only on the Earth life could origin and evolve even if several global events had seriously attempted to its diffusion.

In summary, studying the *terrestrial planets* is of paramount importance in planetary science for two reasons:

1. to deepen knowledge about their formation and to reconstruct their evolution path with respect to planet size, position, impacts etc. Planetary events arrangement is also important to understand affinities and differences among the rocky planets;
2. with their rocky structure, thin atmosphere and the right combination of chemical compounds they are the ideal candidates to hold life origin, diffusion and evolution. On this topic, the study *terrestrial planets* is of paramount importance to understand the mechanisms that govern life implantation and so the reasons for a different biological history.

1.2 *A peculiar terrestrial planet: Mercury*

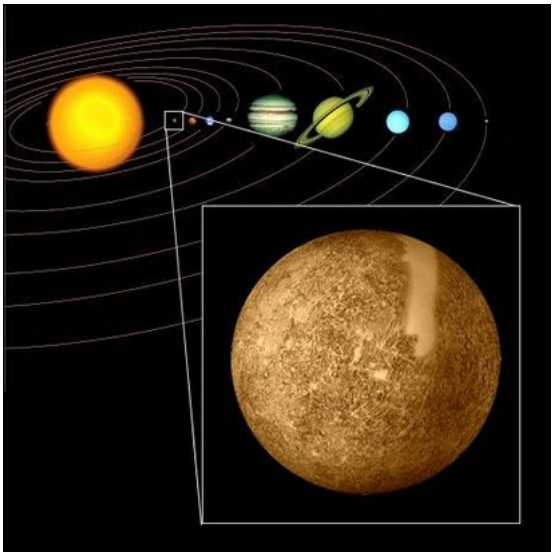

Figure 1: Mercury planetary position in the Solar System.

Mercury is an extreme of our planetary system (Figure 1). Since its formation, it has been subjected to the highest temperatures and has experienced the highest diurnal temperature variations of any other object in the Solar System (presently, 100 K at the night side and 700 K at the dayside). It is both the planet closest to the Sun (0.3 AU) and has the highest uncompressed density of all planets (5.4 g/cm^3). It presents (as the Earth) a magnetic field (300 nT) probably due to an unexpected still melt core. Mercury's surface has been altered during the initial cooling phase and its chemical composition has been modified by heavy bombardment in its early history. In addition, solar tides have influenced its rotational state fixing a 3:2 spin-orbit resonance (Table 1).

MERCURY			
Physical properties		**Orbital parameters**	
Mass [10^{24} kg]	0.3302	Aphelion distance [AU]	0.467
Volume [10^9 km^3]	60.83	Perihelion distance [AU]	0.308
Mean density [kg/m^3]	5427	Eccentricity	0.20563
Mean radius [km]	3439.7	Orbital inclination [°] (over Ecliptic)	7
Mean albedo	0.119	Orbital period [days]	87.969
Superficial temperature (min ÷ max) [K]	100 ÷ 688.5	Sidereal rotation period [days]	58.646

Table 1: Mercury physical properties and orbital parameters.

Seen from Earth, Mercury's maximum elongation from the Sun is about 28° making it visible only for just two hours preceding sunrise and following sunset. Before Pitagora studies (4th century BC), such particular property was interpreted by the ancient Greeks as the planet to be two separate objects: one visible only at sunrise, which they called Apollo, the other visible only at sunset, which they called Hermes.

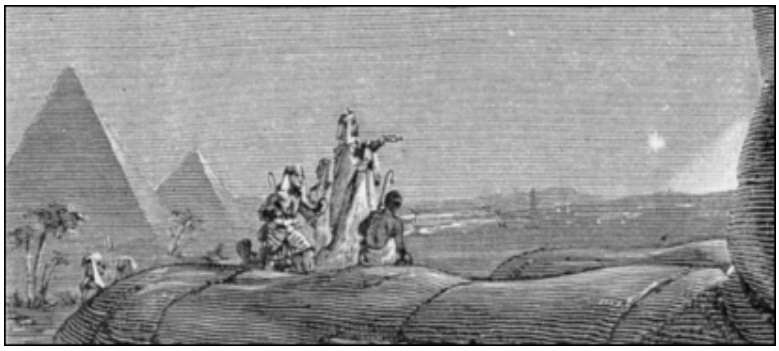

Figure 2: Engraving of Régnier Barbant in G. Flammarion, Astronomie Populaire, 1881.

Even though Mercury was already known to the ancient Egyptians (Figure 2), it is still largely unexplored. Its proximity to the Sun, makes it a difficult target for ground-based and space-born observations: Earth-based observations are normally performed in front of a strong sky background; Earth-orbiting optical telescopes (e.g., Hubble Space Telescope) usually cannot target Mercury either, because of the high potential risks to instruments when they are pointed so close to the Sun.

On the other hand, inserting a spacecraft into orbit around Mercury is not a trivial task, because of the large difference between the gravitational potentials of the Sun at the orbits of Earth and Mercury. In addition, the solar irradiation is about 10 times larger than on the Earth and the heat flux is further increased at the dayside because of reflected sunlight and infrared emission, which place enormous thermal constraints on any orbiter.

The scientific data available so far derive from the NASA probe Mariner-10, which made only three flybys on Mercury in 1974-1975 obtaining images of somewhat less than half its surface and discovering an unexpected magnetic field. These data have been fully exploited but many gross features remain unexplained leaving open many critical aspects discussed synthetically here after.

1. Several models of Mercury's formation assume that the proximity of the Sun and the high ratio between the huge ferrous core (1800-1900 km) and the thick silica mantle (600-700 km) dimensions are linked. Different evolutionary scenarios could lead to such a large Fe/Si ratio: the materials concurring to Mercury's formation could have been enriched in metallic iron, or its basaltic crust might have been stripped away by impacts [2], or a high temperature phase in the solar nebula might have sublimated and blow off silicates [3], thereby leaving only materials with higher condensation temperatures.

2. The relatively large size of the core and its evolution are closely related to the existence of the bipolar 11° tilted magnetic field (one of the most remarkable discoveries of Mariner-10). The field is weak but suggests an internal dynamo ([4], [5]) with a (partially – a shell of at least 500 km is sufficient) molten core; its existence is a challenge because the core of such a small planet should have frozen out early in its history. Thermal and compositional models compatible with the existence of a still (partially) molten core and so a planetary dynamo are [6]:
    a. core enrichment of radioactive elements such as Uranium or Thorium that increase the internal temperature;
    b. core enrichment of elements such as Sulphur that reduce the freezing temperature;
    c. anomalies in core-mantle convection flow boundaries that govern the heat transfer in the planet.

3. The three Mariner-10 fly-bys revealed a surface covered by craters of all sizes. In terms of exogenic processes, this means that the surface of Mercury has mainly been exposed to the steady state secondary flux of impactors in the inner SS, which results from gravitational perturbations and collisional processes within the three reservoirs of surviving planetesimals (the main belt of asteroids, the Kuiper belt and the Oort cloud) [7].

4. Mercury is not likely to have been tectonically active recently, but the features observed on its surface bear evidence of past tectonic evolution [8]. It is considered that Mercury was originally spinning at a much faster rate. When its rotation period increased from a few hours to its present value (59 days) the stresses produced by the relaxation of the equatorial bulge would have created a network of lineaments with preferential NW-SE and NE-SW orientations [9]. The cooling of Mercury's mantle and the partial freezing of the core are likely to have induced a contraction of its radius by 1 – 2 km since the end of the heavy bombardment; lobate scarps [10] resulting from thrust faults provide evidence for this early crustal evolution. The intercrater plains [7], which cover most of the surface, postdate the end of the accretionary tail, 4 billion of years ago. They are the most widespread unit on Mercury and consist of levels to gently rolling plains with a high density of superposed craters.

5. Caloris Basin is one of the largest impact craters in the SS; this basin is 1300 km across and was discovered by Mariner 10, but only half of it has been imaged. The formation of Caloris Basin probably led to a peculiar tectonic patterns: seismic waves caused by the impact travelled through the interior and were focussed by the core [11]. Upon hitting the surface these waves probably generated at the antipode the observed pattern of hills and troughs, 5 to 10 km across and 100 m to 2 km high.

6. Indirect evidences suggest that Mercury has experienced considerable melting during its history [12]. Ground-based observations have led to the conclusion that Mercury has a relatively basalt-free surface, and thus, a magmatic history characterized mainly by intrusion rather than eruptions [13]. Moreover, the presence of a magnetic field implies that a remnant inner portion of the planet is still molten, as mentioned earlier. Volcanism may have been active for a short time on Mercury, because of the cooling of the lithosphere, and core global compression that closed off magma conduits and inhibited volcanism [7]. On the other hand, the large presence of plains on the surface of Mercury may be the result of volcanic activity in the past.

Mercury plains seem to be coincident with the heavy bombardment areas, so another process that can explain the volcanic emplacement of such huge smooth plains could be crustal fracturing caused by the impact cratering which facilitated the upwelling of magma.

7. Mercury is surrounded by a very tenuous atmosphere, with a measured upper dayside density of less than 10^7 atoms/cm^3 [14]. Due to the very low density, the atmosphere is collisionless (i.e., the mean free path of the atoms is larger than the value of the scale height of the atmosphere). Therefore, the whole atmosphere is comparable to an exosphere having the exobase coincident with the planet's surface. The existence of an atmosphere around Mercury was discovered for the first time by the Mariner-10 spectrometers, that revealed three atomic elements: H, He and O. The presence of Na, K and Ca was discovered later using ground-based telescopes [15], [16], [17]. The lifetime of the species in the exosphere is governed by the ballistic time of each of them. The ionised atoms are drifted away from the planet by the solar wind, or aimed back to the surface along the lines of the Mercury's magnetic field. To maintain the present exosphere, the lost atoms must be replaced by some source mechanisms. Processes of endogenic and exogenic origin are supposed to act in repopulating the exosphere: neutralization of solar wind ions (in the case of H and He), radioactive decaying (He), impact vaporization of meteoroids, regolith (Na, O, K) photo-sputtering and photo-desorption (Na, K) and ion sputtering (Ca, Na, K).

1.3 *From Mariner-10 to MESSENGER: Mercury exploration evolution*

Presently all available scientific data about Mercury derive from Earth observations (on-ground and orbital) and from the Mariner-10 probe, that in the beginning of '70s performed three fly-bys with the innermost planet of our SS (Figure 3).

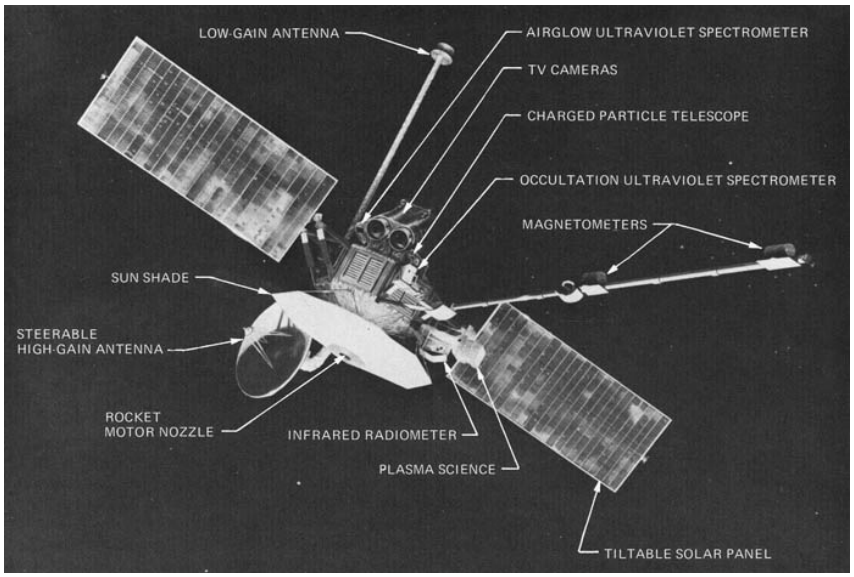

Figure 3: Mariner-10 scientific payload accommodation.

Mariner-10 probe was originally planned to study Venus planet but, thanks to the planetary gravity assist studies of the Italian mathematician Giuseppe Colombo, it was extended to the possibility of three fly-bys around Mercury. The trajectory chosen placed Mariner-10 into solar orbit with exactly twice the planet's orbital period, so it made further approaches to Mercury, which were in the same relative position to the Sun in each occasion.

Such operative conditions determined that Mariner-10 imaging system was able to produce maps of about 45% of the surface with a spatial resolution of the order of about 1 km/pxl and a few images at about 100 m/pxl.

Another important measurement performed by the Mariner-10 probe regarded the Mercury magnetic field. The magnetometer aboard revealed a weak magnetic field (300 nT) which was really unexpected: although the average density of Mercury had strongly suggested the presence of a core rich in iron, its small mass seemed to indicate that it should have been solid.

The MErcury Surface Space ENvironment GEochemistry and Ranging (MESSENGER) mission, launched by NASA on 3 August 2004, will be the first spacecraft to orbit the planet Mercury [18] (Figure 4 – left). Between 2008 and 2009 it has started the Mercury Orbit Insertion (MOI) with periodic one terrestrial year planetary fly-bys, while in March 2011 it will start its operative phase for one Earth year of scientific measurements (Figure 4 – right) on 12-h quite-polar (80°) orbits (200 ÷ 15000 km of altitude).

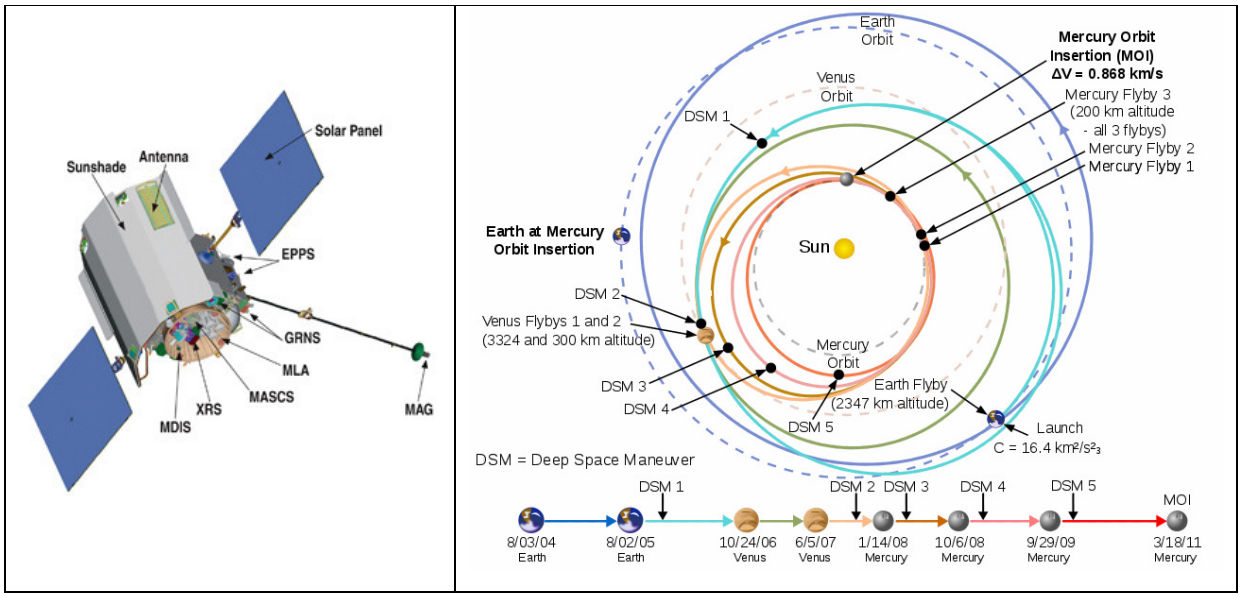

Figure 4: MESSENGER probe (left) and interplanetary journey trajectory (right).

The seven scientific instruments listed in Table 2 are onboard the spacecraft to satisfy the scientific objectives of the mission.

Instrument	Objective
Mercury Dual Imaging System (MDIS) [19]	Wide-angle plus narrow-angle imagers that will map landforms, track variations in surface spectra and gather topographic information.
Gamma-Ray and Neutron Spectrometer (GRNS) [20]	It will be used to map the relative abundances of gamma-rays and neutrons emitted from the planet surface and will help to determine if there is ice at Mercury's poles.
X-Ray Spectrometer (XRS) [21]	It will detect emitted X-rays to measure the abundances of various elements in the materials of Mercury's crust.
MAGnetometer (MAG) [1]	It will map Mercury's magnetic field and will search for regions of magnetized rocks in the crust.
Mercury Laser Altimeter (MLA) [23]	It will produce highly accurate descriptions of Mercury's topography.

Mercury Atmospheric and Surface Composition Spectrometer (MASCS) [24]	It will measure the abundances of atmospheric gases, as well as detect minerals on the surface.
Energetic Particle and Plasma Spectrometer (EPPS) [25]	It will measure the composition, distribution, and energy of charged particles (electrons and various ions) in Mercury's magnetosphere.
Radio Science (RS) [26]	It will use the Doppler effect to measure very slight changes in the spacecraft's velocity due to Mercury's mass distribution anomalies, including variations in the thickness of its crust.

Table 2: MESSENGER scientific payload.

In addition, regions not explored by Mariner-10 will be observed for the first time and new data will be available on Mercury's exosphere, magnetosphere, and surface composition.

1.4 *Bepicolombo space mission overview*

A proposal for a multidisciplinary mission to the planet Mercury was submitted to the European Space Agency in early 1993 in response to a "Call for Ideas". The mission was selected as a cornerstone candidate in the Horizons 2000 scientific programme of the Agency in 1996 with the aim of:

1. Improving scientific knowledge about the origin and evolution of a planet close to the parent star;
2. Determining the internal structure and composition of Mercury (especially the anomalous high Fe/Si ratio) to extract crucial information about planetesimals accretion process in the innermost region of the primitive solar nebula;
3. Characterizing principal Mercury's geological units to better understand the role of terrestrial planet size as a governor of magmatic and tectonic history [27];
4. Linking Mercury's magnetic field measurements with Mercury's core size and state estimation to improve present planetary magnetic dynamos energetic and lifetime models;
5. Identifying the volatile species in Mercury's polar deposits, exosphere, and magnetosphere to provide information about their inventories, sources, and sinks in the inner solar system;
6. Testing Einstein's theory of general relativity.

Based on an independent study carried out by the Mercury Exploration Working Group (MEWG) within the Institute of Space and Astronautical Sciences (ISAS) a spinning Mercury orbiter was proposed.

The involvement of Japan in BepiColombo was discussed at the Inter-Agency Consultative Group (IACG) and stated in a letter from the Director General of ISAS (now JAXA) to the Director of the Scientific Programme of ESA, dated July 2000. On October 2000, ESA's Science Programme Committee (SPC) approved BepiColombo as ESA's 5th Cornerstone mission with launch in 2009/2010.

The International Mercury Exploration Mission in the framework of the BepiColombo programme was approved by the Steering Committee of Space Science (SCSS) of ISAS in January 2002, followed by the formal approval by the Space Activities Commission in June 2003.

On November 2003 the SPC approved the BepiColombo mission design consisting in two probes:

1. The Mercury Planetary Orbiter (MPO), a three-axis stabilized and nadir pointing module, aimed at orbiting around the planet on a polar orbit (400 ÷ 1500 km of altitude) and dedicated to planet-wide remote sensing and radio science (Figure 5).

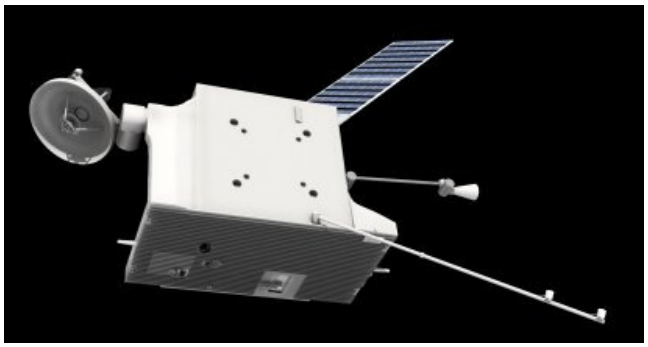

Figure 5: MPO probe.

In the early 2004, ESA issued the MPO payload request for proposals. In November 2005 the SPC definitively approved the list of payload instruments reported in Table 3.

Instrument	Objective
BEpicolombo Laser Altimeter (BELA) [28]	It will measure the Mercury figure parameters, tidal deformation, surface roughness; together with the radio science and imaging experiments it constitutes the geodetic and geophysics study package of the mission.
Mercury Orbiter Radio science Experiment (MORE) [29]	It will provide crucial information useful for Mercury gravity field characterisation, as well as the size and physical state of its core. In addition, it will perform experimental measurements to test theories of gravity with unprecedented accuracy.
Italian Spring Accelerometer (ISA) [30]	Together with the MORE instrument, it will give information on Mercury's interior structure as well as test Einstein's theory of the General Relativity.

MERcury MAGnetometer (MERMAG-MAG) [31]	It will provide a detailed description of Mercury's planetary magnetic field in order to better understand its origin, evolution, current state and its interaction with the solar wind.
MERcury Thermal Infrared Spectrometer (MERTIS) [32]	It will measure with high spectral resolution the mineralogical composition of Mercury's surface for determining a valid model for origin and evolution of the planet.
Mercury Gamma ray and Neutron Spectrometer (MGNS) [33]	It will determine the elemental composition of the surface and subsurface of Mercury, as well as the regional distribution of volatile depositions in the polar areas.
Mercury Imaging X-ray Spectrometer (MIXS) [34]	It will produce a global map of the surface atomic composition at high spatial resolution using the "X ray fluorescence" analysis method.
Solar Intensity X-ray Spectrometer (SIXS) [35]	It will perform measurements of X rays and particles of solar origin at high time resolution and a very wide field of view.
Probing of Hermean Exosphere by Ultraviolet Spectrometer (PHEBUS) [36]	It will characterise the composition and dynamics of Mercury's exosphere. It will also search for surface ice layers in permanently shadowed regions of high-latitude craters.
Search for Exosphere Refilling and Emitted Neutral Abundances (SERENA) [37]	It will study the gaseous interaction between surface, exosphere, magnetosphere and solar wind.
Spectrometer and Imagers for Mpo Bepicolombo Integrated Observatory – SYStem (SIMBIO-SYS) [38]	It will examine the surface geology, volcanism, global tectonics, surface age and composition, and geophysics.

Table 3: MPO scientific payload.

2. The Mercury Magnetospheric Orbiter (MMO), an electromagnetically clean spinner on a relatively eccentric orbit, accommodates mostly the field, wave and particle instruments (Figure 6).

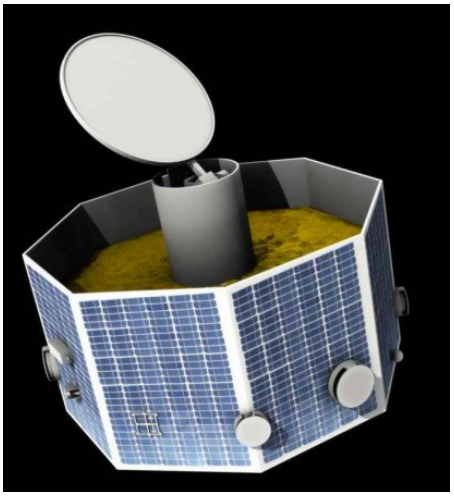

Figure 6: MMO probe.

The payload for the MMO selected by the Japanese space exploration agency JAXA is listed in Table 4.

Instrument	Objective
MERcury MAGnetometer (MERMAG-MGF) [39]	It will provide a detailed description of Mercury's magnetosphere and of its interaction with the planetary magnetic field and the solar wind.
Mercury Plasma Particle Experiment (MPPE) [40]	It will study low- and high-energetic particles in the magnetosphere.
Plasma Wave Instrument (PWI) [41]	It will make a detailed analysis of Mercury's magnetosphere structure and dynamics.
Mercury Sodium Atmospheric Spectral Imager (MSASI) [42]	It will measure the abundance, distribution and dynamics of sodium in Mercury's exosphere.
Mercury Dust Monitor (MDM) [43]	It will study the distribution of interplanetary dust in the orbit of Mercury.

Table 4: MMO scientific payload.

The method for transporting the spacecraft elements to their destinations results from a trade-off between mission cost and launch flexibility. It combines ion propulsion, chemical propulsion and gravity assists. The interplanetary transfer is performed by a Solar Electric Propulsion Module (SEPM) which is jettisoned upon arrival. The orbit injection

manoeuvres are then realized with a Chemical Propulsion Module (CPM) which is also jettisoned once the deployment of the spacecraft elements is completed.

The spacecraft concept is modular and lends itself to a large variety of schemes. Two specific scenarios have been studied in detail:

1. a dual-launch scenario, where the spacecraft is divided into two composites with nearly identical propulsion elements which are launched separately with smaller rockets, such as Soyuz-Fregat;
2. a single-launch scenario, where the two spacecraft elements and the two propulsion modules are injected together into an interplanetary orbit with a large rocket, such as Ariane 5.

Even though the two approaches have been proven feasible and compatible with the given mission objectives and scientific instrumentation, the second solution has been selected due to SEPM and CMP volume and mass requirement to guarantee the correct instrument alimentation and spacecraft attitude control manoeuvres.

Planned at launch in 2013-2014 from the ESA base of Kourou (French Guiana), the BepiColombo spacecraft will set out an interplanetary journey of six years (Figure 7) in which several Earth and Venus fly-bys are foreseen to guarantee the right trust. It will arrive at Mercury in 2019-2020 and it will gather data during 1 year of nominal mission, with a possible 1 year extension.

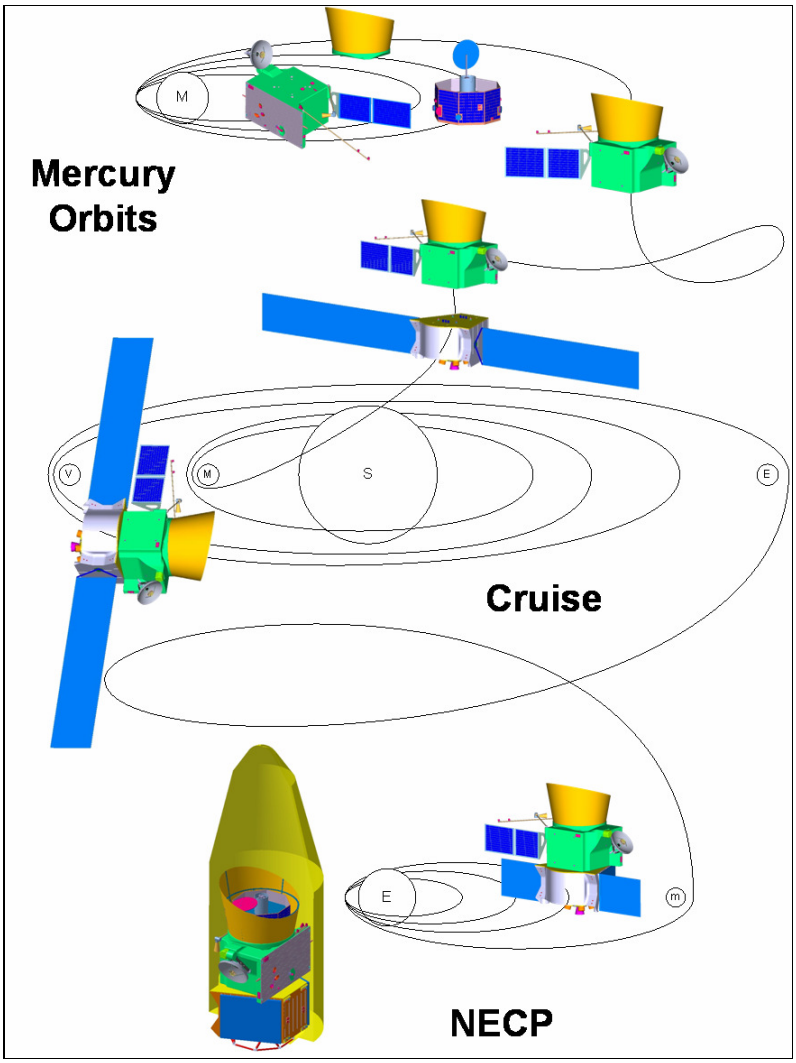

Figure 7: BepiColombo interplanetary journey.

CHAPTER 2

SIMBIO-SYS suite and the high spatial resolution camera

The Spectrometer and Imagers for MPO Bepicolombo Integrated Observatory – SYStem (SIMBIO-SYS) suite is the multi-channel imaging system onboard the BepiColombo mission to Mercury. In this chapter the technical characteristics of the system are introduced. The second part of the chapter is devoted to a detailed presentation of the scientific objectives and the optical-mechanical characteristics of the High Resolution Imaging Channel (HRIC) of SIMBIO-SYS.

2.1 *SIMBIO-SYS overview*

SIMBIO-SYS is an instrument suite aiming at imaging and spectroscopic investigation of Mercury, in order to analyze the geological, mineralogical and chemical characteristics of the surface and the exosphere [38].

The baseline approach used in the SIMBIO-SYS Instrument Front End (IFE) design is oriented to the best sharing of tasks between the different optical channels for imaging and spectroscopic observations in order to maximize the scientific return, while minimising the overall resource allocation. The suite is aimed to provide a simplified interface to the spacecraft, by handling internally the needs of the management of the various channels.

SIMBIO-SYS IFE is constituted by three channels (see Figure 8):

- STereo imaging Channel (STC): it will provide the global colour coverage of the surface at 50 m/pixel resolution with the aim of defining the main geological units, large scale tectonic features, impact crater population and, if present, volcanic edifices. The STC stereo channel will be a useful tool to define with high detail the topography, which is a critical measurement for tectonic features characterization, geological units lateral boundaries definition and for measuring important geophysical parameters. The STC will also provide the context for the narrow angle camera.
- High Resolution Imaging Channel (HRIC): its main objective is the characterization of special surface targets at 5 m/pxl scale from periherm (400 km from planet surface), in different bands in the visible. It will provide high spatial resolution images of selected areas of about 20% of the surface. This approach shall allow us to identify key surface features (e.g., craters, scarps, lava flows and plains) and to study their relation with geological, geophysical and geochemical internal processes, as well as the effects produced by meteoroid bombardment;
- Visual and Infrared Hyper-spectral Imager (VIHI) channel: it will map the planet in order to provide the global mineralogical composition of the surface. The selected spectral characteristics (range 400 – 2000 nm, spectral sampling 6.25 nm) and the

imaging capability (100 m spatial resolution at periherm) will permit to unambiguously correlate the surface composition with the morphological features.

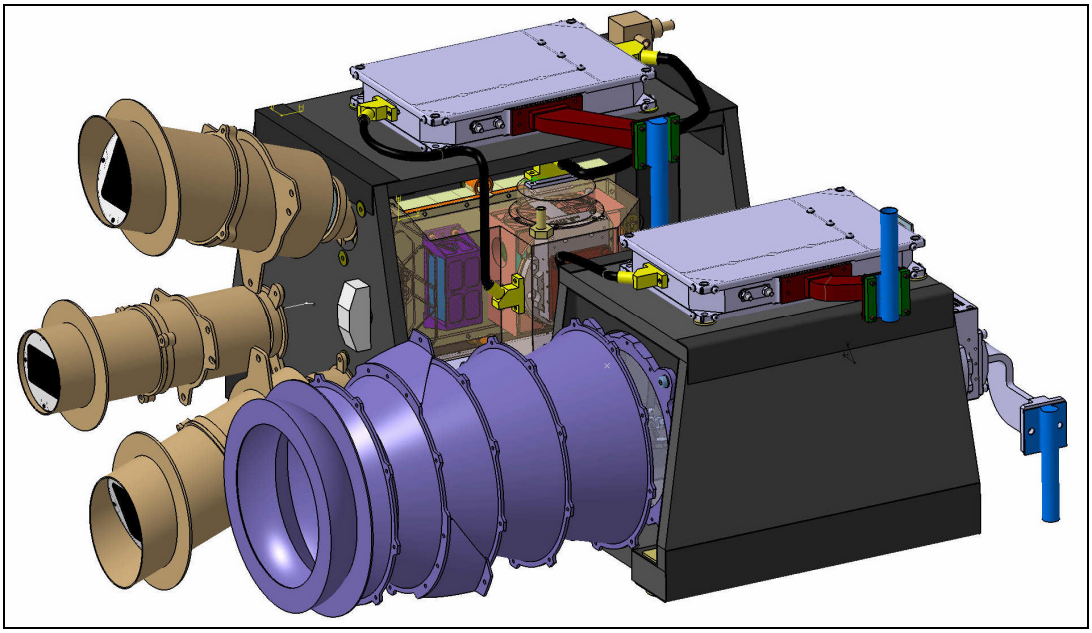

Figure 8: SIMBIO-SYS layout (courtesy of Selex Galileo).

In addition, SIMBIO-SYS includes a digital electronics unit for telecommand / telemetry link, and the converters of the spacecraft power. Main Electronics (ME) and power supply are common at IFE level. Each channel is characterised by optics, detector, thermal hardware (if needed), Proximity Electronics (PE) and electrical interface to the ME.

The PEs are controlled by a Field Programmable Gate Array (FPGA) which handles commands from the ME. When an acquisition is requested, the FPGA implements the required detector configuration, then triggers the acquisition and sends the digitized data set to the ME for further processing.

The ME manages all high level logical interfaces with the spacecraft:

- switch-on and switch-off of each channel;
- reception and interpretation of Telecommands (TC);
- formatting and transmission of Telemetry (TM) packets to the spacecraft.

The communications between the ME and the spacecraft, as well as between the ME and the three channels, use a space-wire link with a transmission clock of 100 MHz and an

actual bandwidth of ~ 80 Mbit/s independently for uplink (spacecraft to ME, ME to IFE) or downlink (IFE to ME, ME to spacecraft).

The ME is constituted of four major units: a Command and Control Processor Unit (CPCU) and three identical Compression Units (CU), each dedicated to a given IFE (HRIC, STC, VIHI).

The CPCU must implement the internal timeline of SIMBIO-SYS according to the received TC, with a "master-slave" relationship between the ME and each of the three IFE's. This timeline is based on an Instrument On-Board Time (IOBT) which is synchronized with the spacecraft On-Board Time (OBT) upon reception of first a time update TC then a time synch through the space-wire time-code.

Each IFE generates science data only upon reception of a parameterized data request from the ME. This data can be either housekeeping (HK) (following a HK request) or science (following a frame request).

Each frame transmitted by a channel is first binned (along columns and / or rows) if requested by the TC parameters, then stored by the FPGA of the corresponding CU (or added to the previous frame if frame binning is requested). Once data acquisition is complete (i.e. after the n-th frame is received if n frames are to be binned), the CU compresses and formats the data in series of data fields of telemetry (TM) packets.

The CPCU continuously polls the three IFE for available data fields. If a data field is ready and if the output buffer of the space-wire interface to the spacecraft is available, it generates a header which tags the packet with the appropriate Application Process ID (APID), the IOBT of the corresponding frame request, and the checksum. The now complete packet is then copied to the output buffer and transmission is initiated.

2.2 *The High spatial Resolution Imaging Channel (HRIC)*

2.2.1 Scientific objectives

HRIC scientific objectives are linked to the investigation of Mercury's surface features whose origin is still matter of wide debate. Some examples are:

- heavily cratered regions, maintaining records of the period of late heavy meteoroid bombardment;
- hilly and lineated terrains, possibly resulting from seismic waves generated by the Caloris impact;
- smooth plains, identified as putative deposits of volcanic eruptions late in planet's history;
- inter-crater plains, identified as impact basin ejecta or lava plains in origin.

The study of such features can be divided in seven scientific themes:

1. Find unambiguous evidence of past volcanic activity

   Measurement: *Obtain high resolution images of intercrater plains, volcanic domes, rills, landform, major basins (also in the unknown hemisphere), and georeferentiate them in the context of the global scale provided by STC and VIHI.*

   This measurement will contribute to solve some still open questions on Mercury's volcanic activity:

   a) did the effusive volcanic activity last much longer than on any other planet?
   b) is the Arecibo evidence of a giant volcanic dome on the unknown hemisphere confirmed?
   c) is the wide spreading of basin ejecta an efficient mechanism for resurfacing?

2. Characterisation of the surface units and their relative ages

   Measurement: *Obtain high resolution images of selected regions of different geologic units on the planet's surface such as heavily cratered regions, hilly terrains (antipodal to Caloris Basin), smooth plains, intercrater plains.*

This measurement will allow to improve our knowledge on the general characteristics of the planet's surface: the heavily cratered regions, which are considered as the record of the period of late heavy meteoroid bombardment; the hilly terrains, result of seismic waves generated by the Caloris impact; the smooth plains, which are possibly volcanic deposits erupted late in planet's history; the intercrater plains, and their still unclear nature of either impact basin ejecta or lava basin

3. Probe the past (recent) tectonic activity

   Measurement: *characterise at small spatial scale the network of lineaments (Global Grid Network) distributed on a global scale, in order to constrain the small-scale texture and the local tectonic events.*

   This measurement will contribute to solve some still open questions on the Mercury's tectonic activity:

   a) are the NW-SE and NE-SW lineaments a general feature confirming the braking of the planet rotation period?
   b) are the lobate scarps the results of the cooling of planets' mantle?

4. Investigation of the planet's exogenic processes of evolution

   Measurement: *map the fine-grained regolith in several flat-floored craters at different values of latitude and longitude, in order to study the effect of the continuous micro-bombardment (β-meteoroids), and the role of varying thermal and particle environment in modifying surface properties.*

   This measurement is aimed at studying the fine-grained regolith on the Mercury's surface, probably 5 to 10 meter thick on average, which is expected to be much more mature than the Moon's surface. The effects that will be explored are the large glassy component of the regolith, the release of free metallic iron due to micro-impacts, the radiation damage from the solar wind.

5. Geomorphological characterisation of impact craters

   Measurements: *obtain high resolution images of highly degraded rims of large and ancient craters in order to support the reconstruction of the degradation sequence, the aging processes and the rate of global resurfacing.*

   This measurement will allow us to explore in detail particular surface features, such as craters of different epochs and evolutions. The complex impact craters on Mercury are significantly shallower than those on the Moon and deeper than those on Mars, and this is probably due to differences in upper crust. The investigation of the erosional processes and the crater removal will be supported by the link between small crater morphology and the regolith thickness. Moreover, details on secondary craters and impact ejecta will be obtained, which will allow us to derive direct information on the nature of surface and sub-surface materials.

6. Understand the mineralogical composition of planet's surface

   Measurement: *obtain high-resolution (5 to 20 m pixel scale, down to about 1/20 of VIHI pixel scale) images of selected surface features in specific broad-band filters, in order to correlate surface features and surface composition to a scale comparable with the regolith mixing length.*

   The HRIC multicolour high resolution images will help in exploring the surface distribution of different materials at a small spatial scale (Figure 9). The analysis of the link between the different surface compositions and the observed morphology and/or individual landmarks will allow us to investigate the low abundance in ferrous iron (Fe^{2+}), the anorthositic composition with a FeO content of ≤ 6%, the distribution of surface and sub-surface materials (olivine, pyroxene, feldspars, glass materials) and the metal-to-silicate ratio on Mercury.

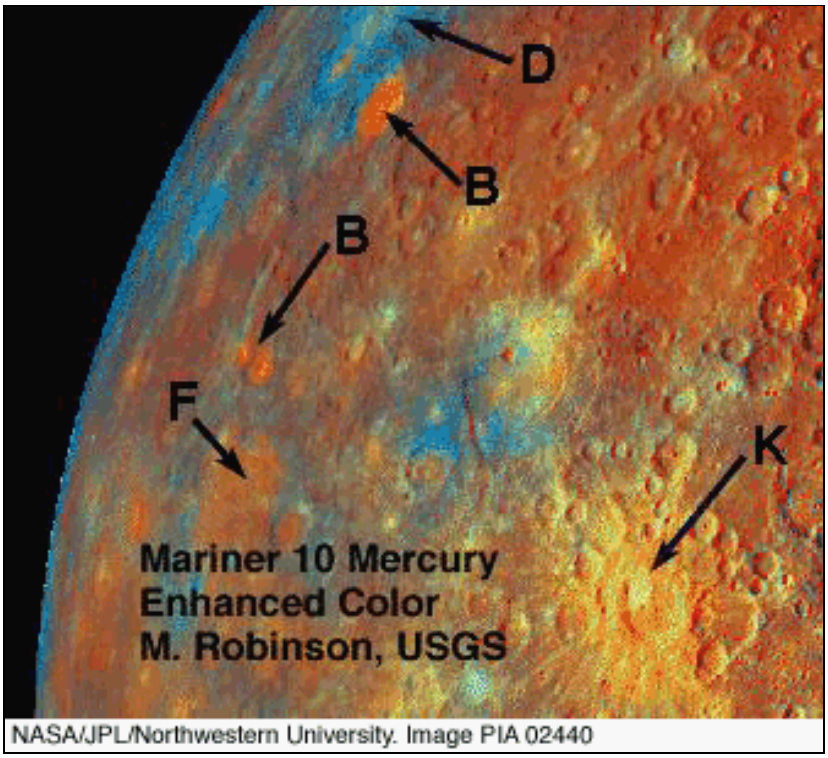

Figure 9: Enhanced colour image of Mercury's surface taken by Mariner 10 (available on http://photojournal.jpl.nasa.gov/catalog/PIA02440). B) bright units that may represent primitive crustal material; D) relative dark and blue unit with enhanced titanium content; F) colour unit that follows plains boundaries and is interpreted as lava flow; K) Kuiper crater with fresh material excavated from a subsurface unit that may have an unusual composition.

7. Determination of moment of inertia of the planet

Measurement: *Identification, accurate location and observation (at different phases of libration in longitude) of surface signatures on a small-scale, in order to support the libration experiment.*

The libration (or rotation) experiment to be performed by MORE ([29]) requires that the same spot on the surface ("landmark") is observed several times at different mean anomalies.

The measurement to fulfil this sub-theme will pose specific constraints on operations for "libration" observations: it will be necessary to choose "landmark" pairs of surface features that can be observed on the periside of the orbit [46]. Albedo spots are the best candidates for pattern matching. For recognising patterns of albedo spots, low phase angles ($\alpha < 10°$) are to be avoided for lack of contrast, and high phase angles ($\alpha > 60°$) are to be avoided as well because of long shadows.

To accomplish these scientific tasks, HRIC will have to:

- Acquire images of about 20% of the planet surface at high spatial resolution;
- Observe interesting surface targets (about 5% of the total amount of observations) at maximum spatial resolution (pixel scale = 5 m/pxl);
- Localise and analyse in detail key surface features for planet age estimation [44], [45].

Surface areas to be observed will derive from present knowledge and shall probably include additional new and appealing targets, poorly known so far, deriving from the MESSENGER mission results. HRIC will provide images with a detail level 4 times (linear) higher than the best achievable by the MESSENGER MDIS cameras [19]; this will represent a major improvement in Mercury surface characterisation.

2.2.2 Optical-mechanical design

The High Resolution Imaging Channel (Figure 10) has been designed in order to satisfy the primary scientific requirement of performing imaging of selected areas of the planet with ground pixel scale of 5 m/pxl at a distance of 400 km from the planet surface.

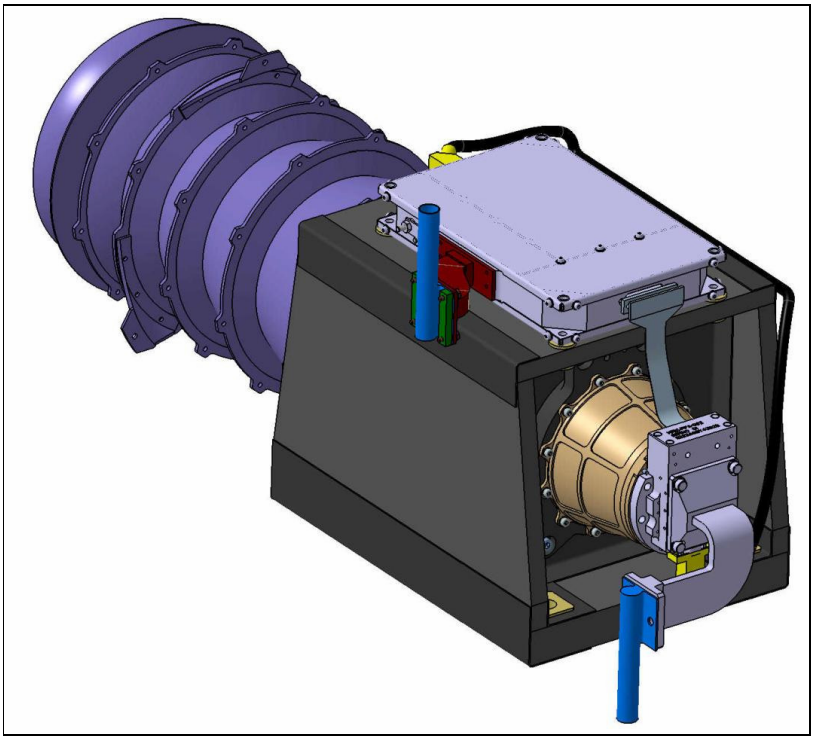

Figure 10: HRIC complete optical-mechanical design (courtesy of Selex Galileo).

In the overall optical-mechanical design (Figure 10) there are six major elements:

1. external baffle (in front of the optical aperture): this element protects the incoming optical bundle up to the camera optical entrance and, above all, thanks to its profile (Stavroudis configuration – see Section 3.3.2), it reduces the thermal load coming form the planet;
2. optics housing (dark grey box): it consists of a honeycomb sandwich that supplies support against vibrations and thermal distortions and protects HRIC optics from external straylight;
3. proximity electronics (PE - box on the top of the optics housing): it is responsible for HRIC data digitalisation and transmission to the spacecraft through the SIMBIO-SYS Main Electronics (housed in a separate box) and for setting sensor parameters;

4. conical support structure (light brown cone): this element contains the HRIC optics corrector (three lenses) that focalised the light on the detector through the filters;
5. detector package (light grey element at the end of the structure): it contains HRIC filters, detector and Read-Out Integrated Circuit (ROIC);
6. heat pipes (blue tubes): these elements connect HRIC detector and PE to radiators to control their temperature.

Inside the optics housing and the conical support structure (Figure 10 – dark green box and light brown cone) the HRIC telescope (Figure 11 – black structure plus the blue-mirror in the middle) is placed together with:

- the Heat Rejection Filter (violet disk);
- the optics corrector (transparent azure lenses);
- the detector (green & brown box).

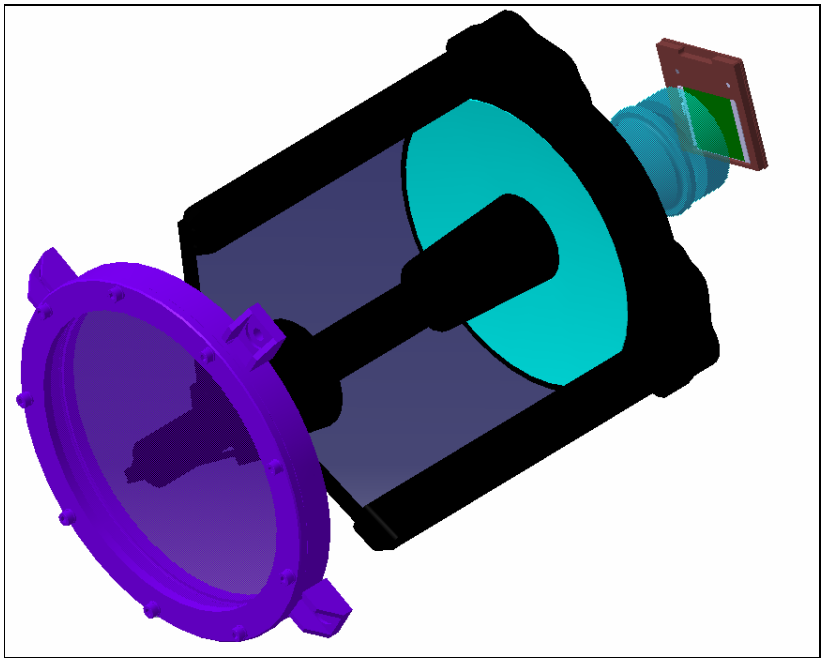

Figure 11: HRIC telescope, detector and Heat Rejection Filter (courtesy of Selex Galileo).

The HRIC optical design is based on a catadioptric Ritchey- Chretien concept with a focal length of 800 mm, modified with a dedicated refractive camera, in order to correct the field of view (Figure 12). The adopted configuration gives a pixel resolution of 2.5″ for a pixel size of 10 μm. The focal ratio of the instrument is F/8.9, in order to be diffraction limited at

400 nm that, together with the adopted 2048x2048 detector, guarantees a squared Field Of View (FOV) of 1.47°.

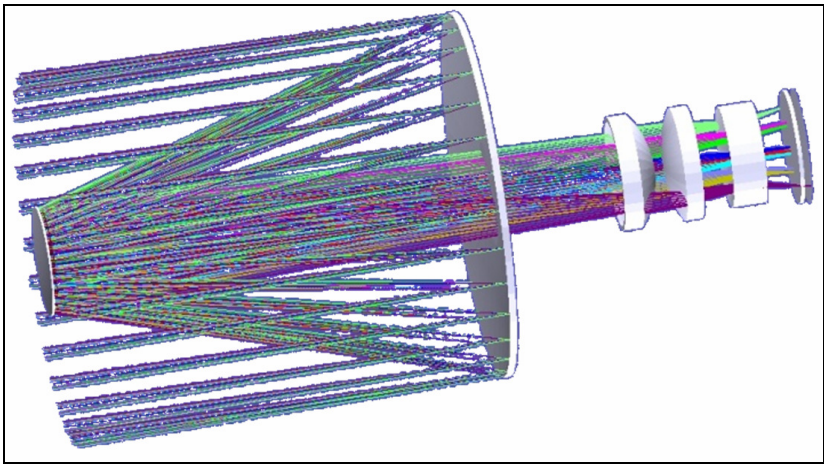

Figure 12: HRIC optical layout (courtesy of Selex Galileo).

The combined (reflective and refractive) solution guarantees a good balance of achieved optical performances and optimisation of resources (mainly volume and mass), as it results more convenient than a pure dioptric solution (in terms of number of optical elements and total length) [47].

Since the system is diffraction limited, the fraction of diffraction Encircled Energy (EE) enclosed in one pixel is considered in order to optimise the image quality. The fraction of EE over the whole field of view is > 67%. The diffraction Modulation Transfer Function (MTF) is > 50% at the Nyquist frequency over the whole field of view. The root mean square (RMS) spot diameter is < 2 μm over the full field, so it is well enclosed in the Airy disk. The field curvature is < 38 μm and the maximum distortion is about 0.2%.

The adopted optical solution achieves a relative obscuration ratio of 40% (in diameter) including internal baffles in order to reduce straylight and to provide a good energy transfer to the telescope exit pupil.

The main tasks of the HRIC are to provide high resolution images with a pan-chromatic filter (centred at 650 nm and with 400 nm of bandwidth) and to help in geo-mineralogical characterisation of local surface features by band-pass filters. Filters centred at 550, 750 and 880 nm (bandwidth 40 nm) are foreseen (Figure 13).

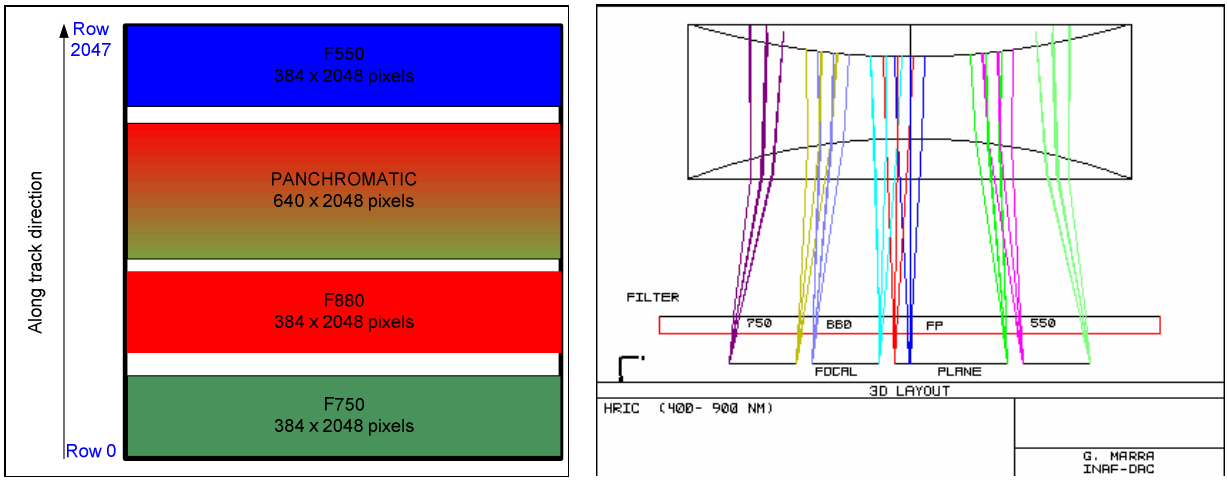

Figure 13: HRIC filter positioning and dimensions with respect to the focal plane (left – top view; right – lateral view).

A hybrid 2k x 2k Si-PIN CMOS array has been chosen as detector, due to its characteristics and capabilities which ensure required performances to the system. It allows low power consumption and shall benefit from the huge on-going research and development in CMOS technology. In addition, CMOS technology has a better tolerance to radiation: existing sensors have a radiation tolerance better than 230 krad (Co^{60}). The array solution is preferred to linear detectors to allow snapshot image acquisition, which appears less critical with respect to requirements on pointing and stability from spacecraft in an extreme thermal environment as that expected at Mercury orbit. HRIC sensor (Figure 14) is characterised by a squared pixel of 10 µm in size, a Fullwell charge greater than 120 ke^-, a very low readout noise (about 60 e^-) and a readout circuit at 5 Mpix/s that transfers to the PE the acquired signal of every pixel every 0.2 µs.

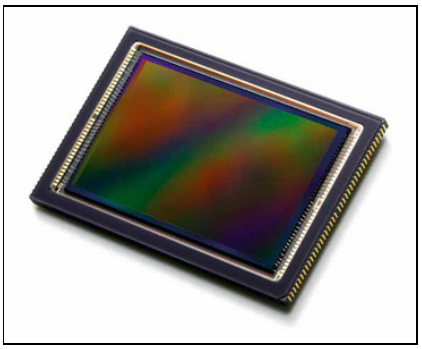

Figure 14: HRIC hybrid Si-PIN CMOS sensor.

Readout circuit is also able to read different areas of the sensor in parallel (windowing); as a result it is possible to transfer data acquired in different spectral ranges (see HRIC filter positioning Figure 13) simultaneously.

2.2.3 Images acquisition and transmission

Data acquired by HRIC sensor are digitalised in the PE (Figure 15): the analogue signal of each pixel is transferred to the Analogue-to-Digital-Converter (ADC) which produces 14 bits for each sample (or pixel). Bits are than transferred to the internal FPGA where:

- they can be directly transmitted to the ME through the space wire at 80 Mbit/s;
- they can be temporary transferred to a local buffer (especially in the case where the incoming amount of data exceed the space wire transfer capability);
- for some particular HRIC science operative modes (see Section 4.2), they can be manipulated to reduce data rate or increase signal strength (i.e., binning).

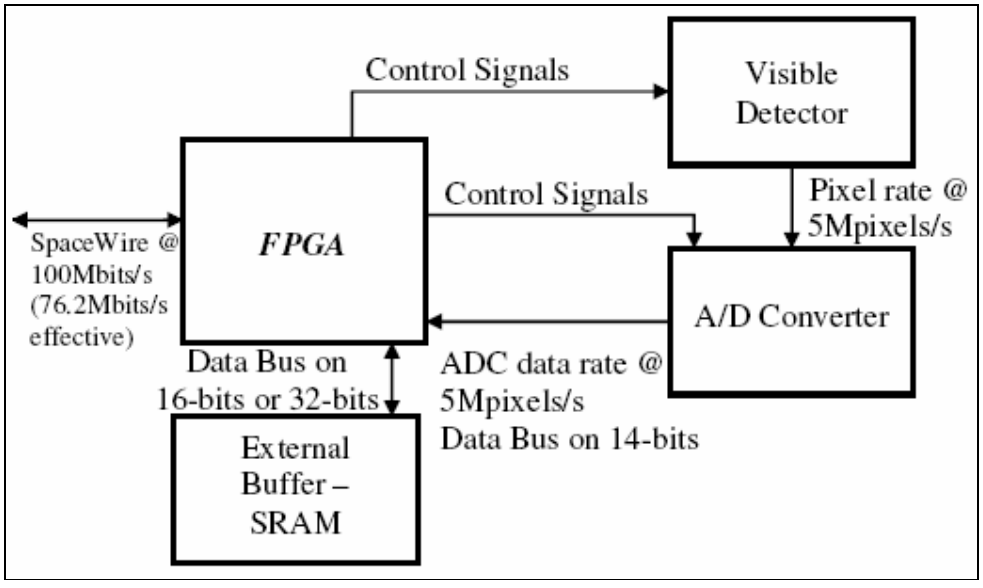

Figure 15: HRIC PE scheme (courtesy of Selex Galileo).

PE also commands the HRIC sensor through control signals that generally derive from ME Telecommands.

Once transferred to the SIMBIO-SYS ME (Figure 16), HRIC data are compressed and packed before being sent to the spacecraft. To ensure data transfer but also the correct

functioning of all the SIMBIO-SYS suite (especially in case of circuital damage) a redundant DPU is foreseen.

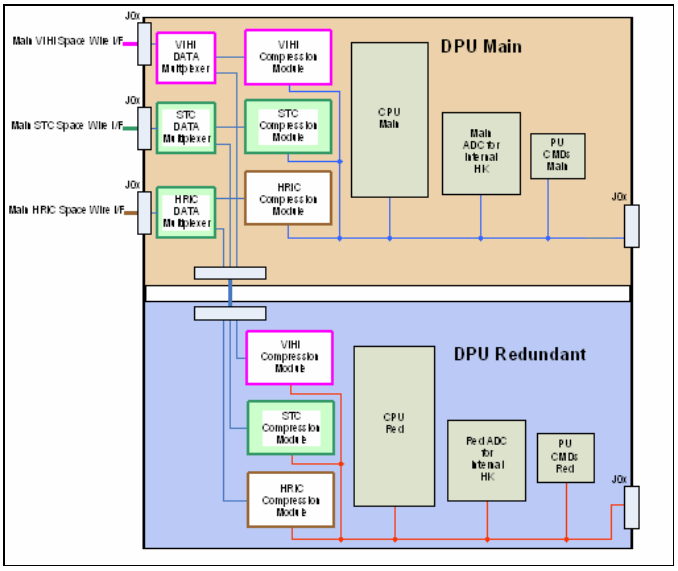

Figure 16: SIMBIO-SYS ME scheme (courtesy of Selex Galileo).

CHAPTER 3

HRIC imaging performances

The analysis on the imaging performances of the high resolution camera of SIMBIO-SYS is a key part of the instrument development. In this chapter we report the details of investigations on some key aspects: radiometric and imaging performances, filters optical characteristics and baffle rejection properties. The HRIC Radiometric Model (HRIC-RM) consists of a mathematical description of the radiance-to-signal (image) conversion process performed by the camera through the optical path and the detector specifications. The "visual" extension of the HRIC-RM is the HRIC Simulator (HRIC-SIM), which allows to apply the HRIC-RM equations, combined with a mathematical description of the HRIC optical layout, in order to extract from an input scenario (synthetic or realistic) a preview of the output image produced by the camera.

In addition, key optical elements such as the HRIC filters, with respect to in-band vs. out-of-band transmission and ghosts production are analysed.

Finally, a comparative analysis of the HRIC external baffle optical rejection properties has been performed, considering two possible layouts: conical (baseline solution) and cylindrical configurations.

3.1 *The Radiometric Model of the HRIC*

The High Resolution Imaging Channel – Radiometric Model (HRIC-RM) consists on a mathematical description of the entire process by which the high spatial resolution channel of SIMBIO-SYS suite transforms into an image the solar spectral Irradiance back-reflected from the Mercury surface. HRIC-RM uses observational geometric parameters and computes the statistical distribution of the output signal and the noise in order to simulate the performances of the camera in any operative condition by estimating the Signal-to-Noise-Ratio (SNR) image quality parameter.

3.1.1 Basic theory

HRIC-RM derives from the modelling of two features: the Mercury surface radiance acquired by the HRIC and the radiance-to-signal conversion process. In the next two paragraphs both themes are analysed.

3.1.1.1 Mercury Radiance

The thermal spectral Radiance of a Black Body is described by the Planck's law ([48] – Chapter 2):

$$L_{bb}(\lambda) = \frac{2hc^2}{\lambda^5\left[e^{\frac{hc}{\lambda kT}} - 1\right]} \left[\frac{W}{m^2 \cdot nm \cdot sr}\right] \quad \begin{cases} h & \text{Plank's constant} & 6.63 \cdot 10^{-34} & [J \cdot s] \\ c & \text{Light speed} & 3 \cdot 10^{8} & \left[m/s\right] \\ T & \text{Solar temperature} & 5776 & [\text{K}] \\ k & \text{Boltzmann's constant} & 1.38 \cdot 10^{-23} & \left[J/K\right] \end{cases}$$

Equation 1: Black Body Spectral Radiance (Planck's law).

which defines the power emitted by a unit surface in a unit solid angle for each wavelength (λ) (see Figure 17 – red arrows; considering the Sun as black body).

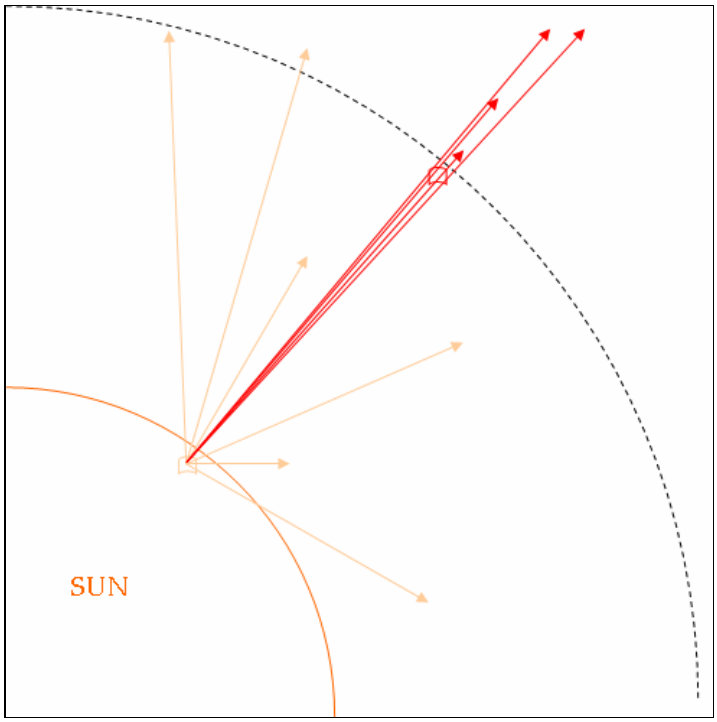

Figure 17: Solar Spectral Radiance.

Figure 18 shows the radiance profile emitted by a unit surface of a black body at 5776 K for each wavelength in a unit solid angle (derived from Equation 1).

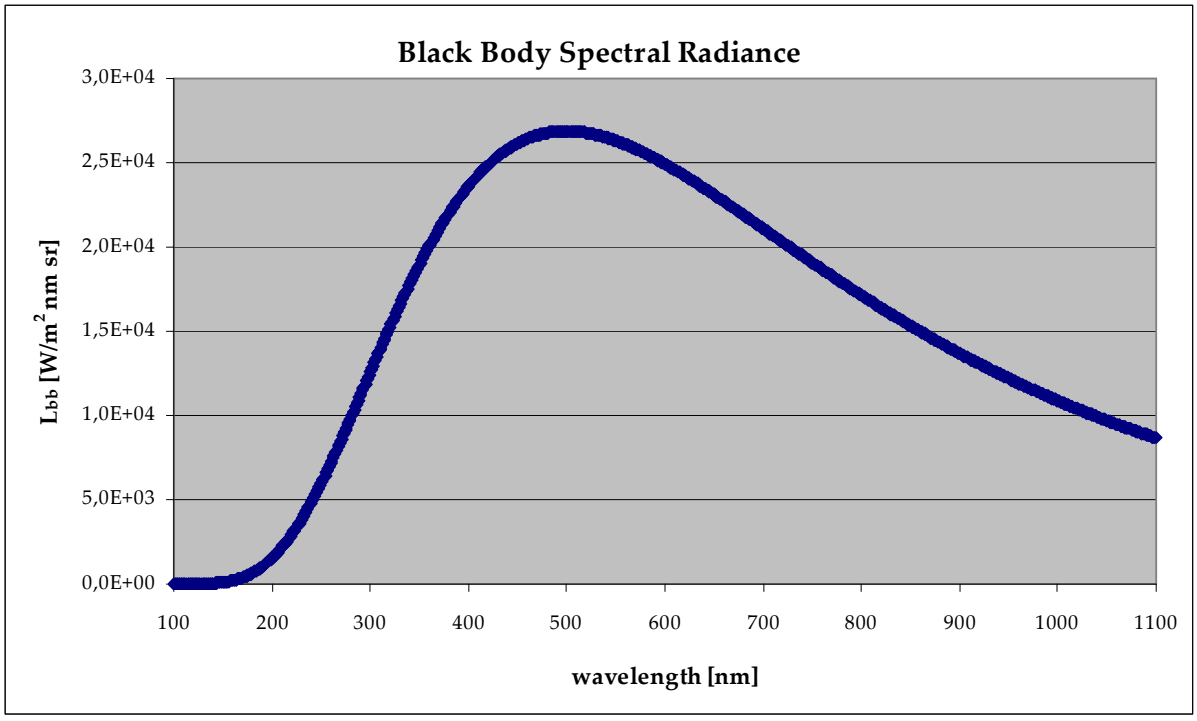

Figure 18: Sun Spectral Radiance profile (Sun as Black Body at 5800 K).

In order to estimate the total power for each wavelength, emitted by each Sun unit surface and impinging on Mercury, the solid angle corresponding to the Mercury surface has to be considered (Figure 19 – left and Equation 2).

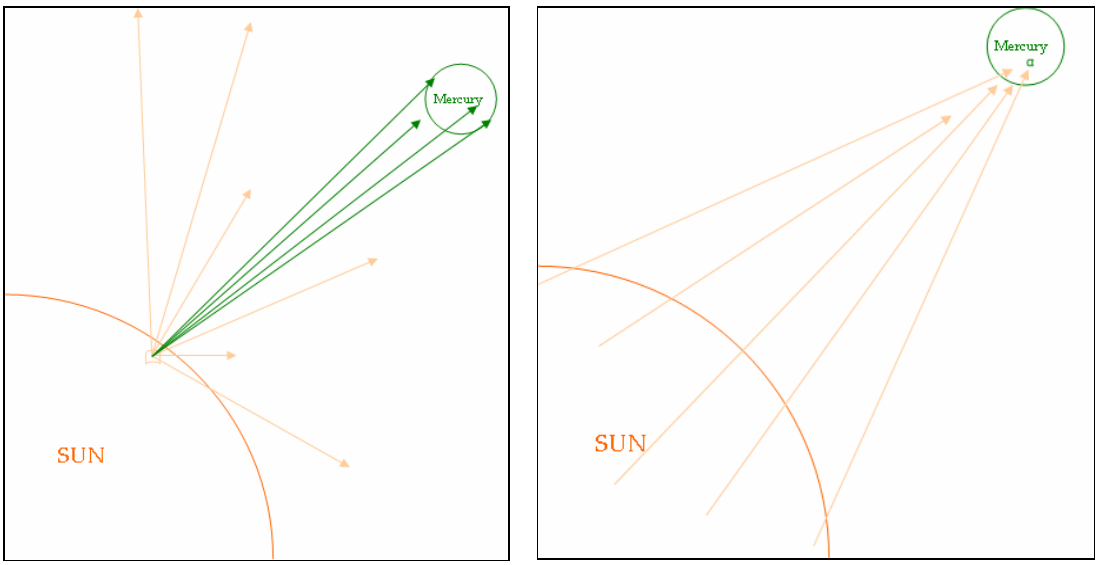

Figure 19: Solar Spectral Radiance at Mercury (left) and Solar Spectral Irradiance (right).

$$\Omega_{S-M} = \frac{\pi R_M^2}{d_{S-M}^2} \quad [sr]$$

Equation 2: Sun-Mercury solid angle.

where R_M is the Mercury mean radius and d_{S-M} is the Sun-Mercury distance.

To derive the spectral radiance acquired by HRIC it is necessary to determine the radiance back-reflected from each Mercury surface element (at each wavelength); as consequence, the Figure 19 – right solid angle cone must be considered.

The resulting "Mercury-Sun" solid angle is:

$$\Omega_{M-S} = \frac{\pi R_S^2}{d_{S-M}^2} \quad [sr]$$

Equation 3: Mercury-Sun solid angle.

where R_S is the Sun mean radius.

The Mercury-Sun solid angle depends on d_{S-M}; considering it constant could determine significant errors in impinging spectral power estimation, taking into account the high value of eccentricity (e = 0.2) of Mercury orbital trajectory (Figure 20).

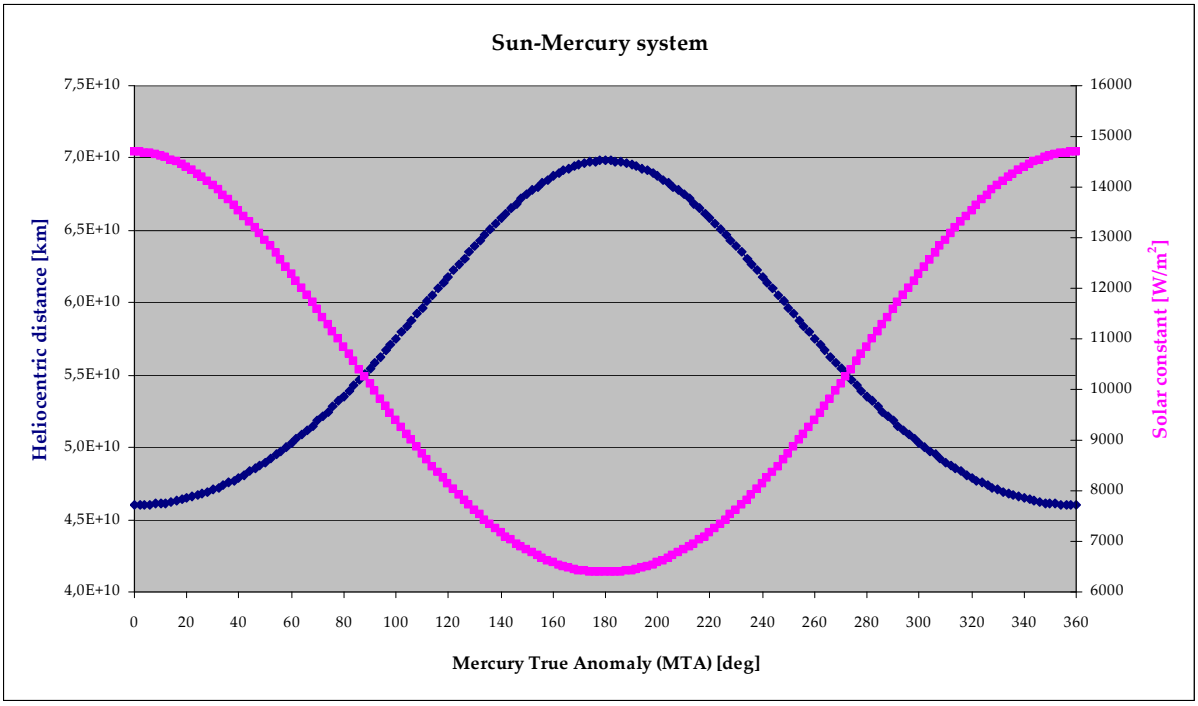

Figure 20: Mercury heliocentric distance and Solar constant at Mercury with respect to Mercury True Anomaly (MTA).

As consequence, it is necessary to modify the solid angle expression by substituting d_{S-M} with the expression of the orbital position of a target in an elliptical trajectory (first Kepler's law – Equation 4):

$$d_{S-M} = \frac{a_M\left(1-e_M^2\right)}{1+e_M\cos\left(\psi_M\right)} \quad [m]$$

Equation 4: Orbit equation.

where a_M is the Mercury orbital semi-major axis, e_M is the Mercury orbital eccentricity and ψ_M is the Mercury True Anomaly (MTA).

The total power impinging on each Mercury surface element and for each wavelength (Figure 19 – right) is:

$$E_{Mercury}(\lambda) = L_{Sun}(\lambda) \cdot \Omega_{M-S} = \frac{2hc^2}{\lambda^5 \left[e^{\frac{hc}{\lambda kT}} - 1 \right]} \cdot \pi R_{Sun}^2 \cdot \left[\frac{1 + e_M \cos(\psi_M)}{a_M (1 - e_M^2)} \right]^2 \left[\frac{W}{m^2 \cdot nm} \right]$$

Equation 5: Sun Spectral Irradiance at Mercury.

The Sun-induced spectral Radiance (Figure 21 – green arrows) can be derived by considering the Mercury albedo profile ($A_M(\lambda)$) and assuming a Lambertian distribution of planetary surface roughness:

$$L_{Mercury}(\lambda) = E_{Mercury}(\lambda) \cdot A_M(\lambda) \cdot \frac{1}{\pi} =$$

$$= \frac{1}{\pi} \cdot \frac{2hc^2}{\lambda^5 \left[e^{\frac{hc}{\lambda kT}} - 1 \right]} \cdot \pi R_{Sun}^2 \cdot \left[\frac{1 + e_M \cos(\psi_M)}{a_M (1 - e_M^2)} \right] \cdot A_M(\lambda) \left[\frac{W}{m^2 \cdot nm \cdot sr} \right]$$

Equation 6: Sun-induced Mercury spectral Radiance.

Finally, the Sun-induced Mercury Radiance entering into the HRIC telescope can be derived considering the appropriate solid angle (Figure 21 – black arrows and Equation 7):

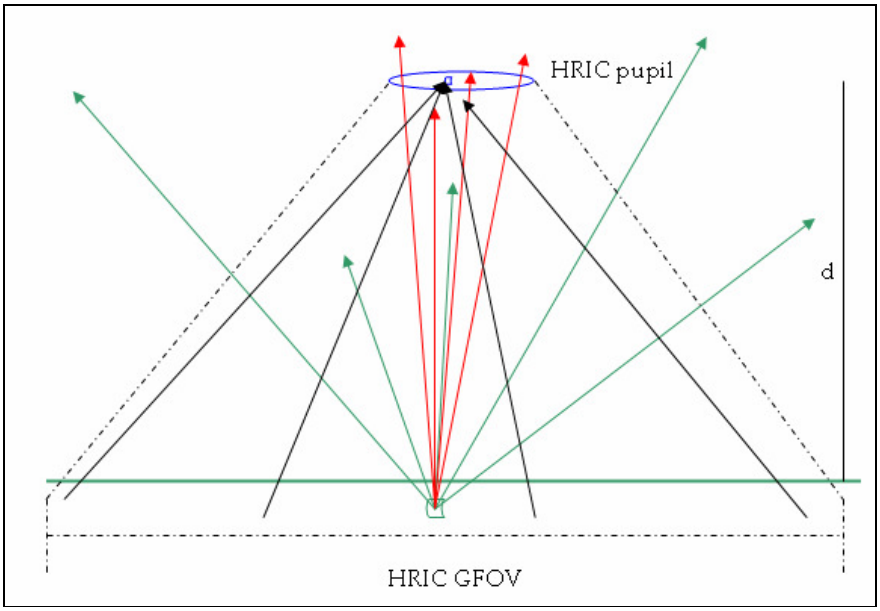

Figure 21: Acquisition geometry. Ground Field Of View (GFOV) represents the on-ground projection of the Field Of View (FOV) of the camera.

$$\Omega_{HRIC-M} = \frac{GFOV^2}{d_{M-HRIC}^2} = \frac{\left[2d_{M-HRIC}\tan\left(FOV/2\right)\right]^2}{d_{M-HRIC}^2} = 4\tan^2\left(\frac{FOV}{2}\right) \ [sr]$$

Equation 7: HRIC-Mercury solid angle.

where d_{M-HRIC} is the Mercury-HRIC distance.

The Mercury-HRIC distance variability due to spacecraft motion along its elliptical trajectory does not influence the HRIC-Mercury solid angle value: the input spectral power loss due to distance variability is recovered by on-ground integration area widening (and vice versa).

The HRIC-entering Mercury radiant spectral flux is, then, computed by considering operative latitude (*lat*), phase angle (correspondent to MTA), telescope aperture and entrance pupil (EP) and is given by:

$$\Phi_{Mercury}(\lambda) = L_{Mercury}(\lambda)\cdot\Omega_{HRIC-M}\cdot\left|\cos(lat)\right|\cdot\left|\cos(MTA)\right|\cdot EP =$$

$$= \frac{4}{\pi}\cdot\pi R_{Sun}^2\cdot\left[\frac{1+e_M\cos(\psi_M)}{a_M\left(1-e_M^2\right)}\right]^2\cdot\tan^2\left(\frac{FOV}{2}\right)\frac{2hc^2}{\lambda^5\left[e^{\frac{hc}{\lambda kT}}-1\right]}\cdot A_M(\lambda)\cdot\left|\cos(lat)\right|\cdot\left|\cos(MTA)\right|\cdot EP \ \left[\frac{W}{nm}\right]$$

Equation 8: HRIC input Mercury radiant spectral flux.

To complete the Mercury radiance estimation an additional element should be considered: Mercury can be considered as a black body at 700 K (dayside temperature of the planet). Applying the Plank's law (Equation 1) the Mercury thermal radiance can be calculated and added to the solar flux. Figure 22 reports a comparison of the two spectral irradiance contributes.

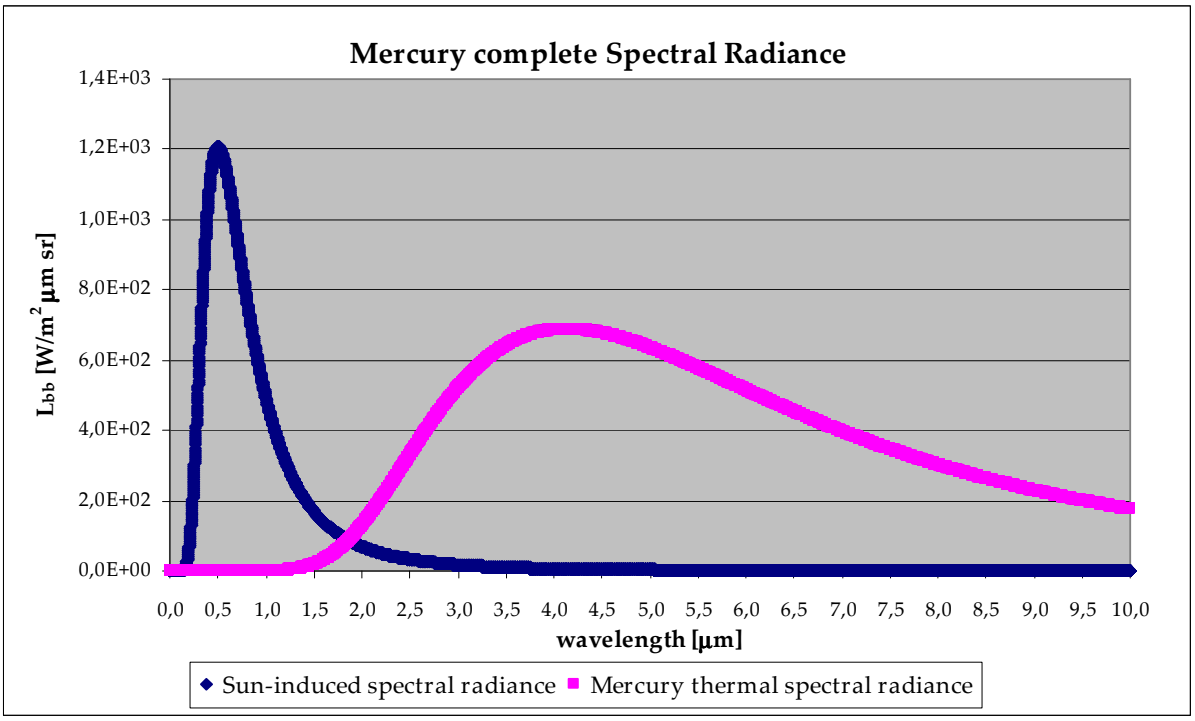

Figure 22: Complete Mercury spectral radiance.

However, being HRIC an imaging channel operating in the visible range of the spectrum (between 400 and 900 nm) the Mercury thermal radiance contribution can be considered negligible in HRIC input radiance estimation.

In the following only Sun-induces radiance is considered as Mercury radiance that contributes in image signal definition.

3.1.1.2 Image signal

Before being focused onto the HRIC hybrid Si-PIN CMOS detector, the Mercury spectral radiance entering in the HRIC pupil (EP) is "filtered" through (see Section 2.2.2) a panchromatic (FPAN – centred at 650 nm with 500 nm of bandwidth) and three broad-band filters (F550, F750 and F880 – centred at 550, 750 and 880 nm respectively all with 40 nm of bandwidth). Figure 23 shows the portions of Sun spectral irradiance filtered by each filter.

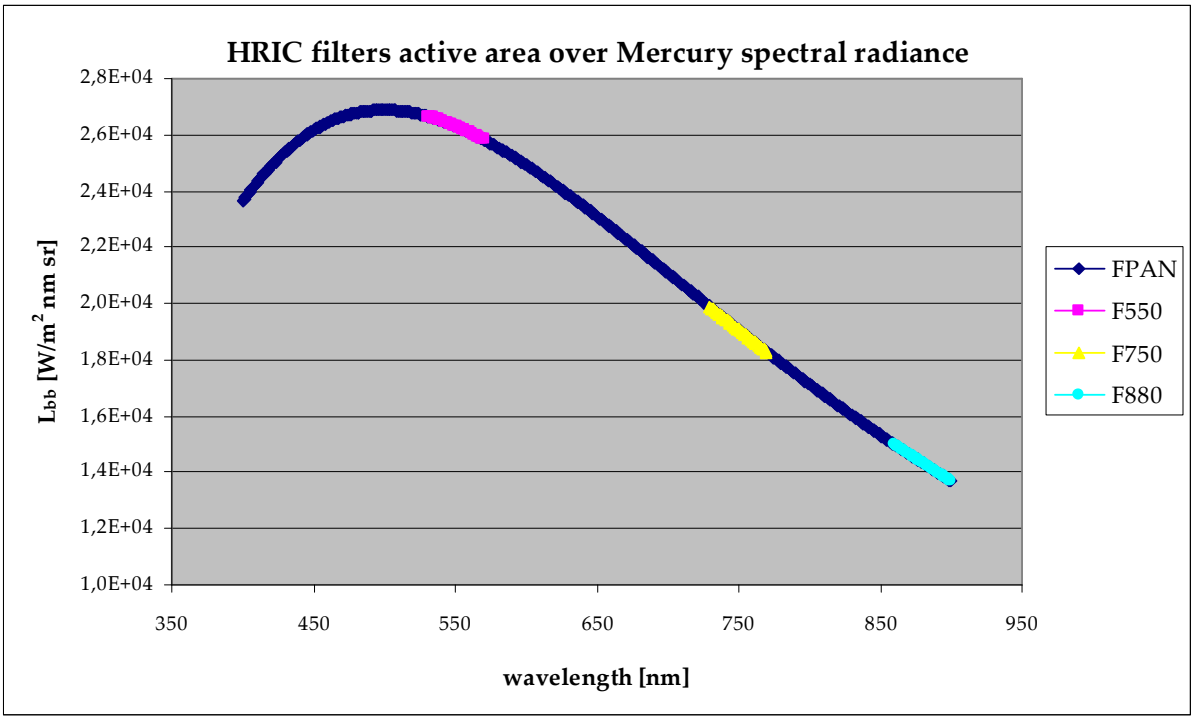

Figure 23: Operating spectral intervals of HRIC filters on black body emission.

Equation 9 reports the mathematical expression of this spectral power selection:

$$G = \frac{4}{\pi} \cdot \pi R_{Sun}^2 \cdot \left[\frac{1 + e_M \cos(\psi_M)}{a_M (1 - e_M^2)} \right]^2 \cdot \tan^2 \left[\frac{FOV}{2} \right] \cdot EP \cdot |\cos(lat)| \cdot |\cos(MTA)| \quad [m^2 sr]$$

$$signal = \begin{cases} G \int_{530}^{570} \frac{2hc^2}{\lambda^5 \left[e^{\frac{h \cdot c}{\lambda \cdot k \cdot T}} - 1 \right]} \cdot A_M(\lambda) \cdot d\lambda & (F550) \quad \left[\frac{\mathrm{W}}{\mathrm{m}^2 sr} \right] \\ G \int_{730}^{770} \frac{2hc^2}{\lambda^5 \left[e^{\frac{hc}{\lambda kT}} - 1 \right]} \cdot A_M(\lambda) \cdot d\lambda & (F750) \quad \left[\frac{\mathrm{W}}{\mathrm{m}^2 sr} \right] \\ G \int_{860}^{900} \frac{2hc^2}{\lambda^5 \left[e^{\frac{h \cdot c}{\lambda kT}} - 1 \right]} \cdot A_M(\lambda) \cdot d\lambda & (F880) \quad \left[\frac{\mathrm{W}}{\mathrm{m}^2 sr} \right] \\ G \int_{400}^{900} \frac{2hc^2}{\lambda^5 \left[e^{\frac{hc}{\lambda kT}} - 1 \right]} \cdot A_M(\lambda) \cdot d\lambda & (FPAN) \quad \left[\frac{\mathrm{W}}{\mathrm{m}^2 sr} \right] \end{cases}$$

Equation 9: Filter outgoing radiance.

The above equations, however, do not consider the spectral properties of the following HRIC optical components (see Section 2.2.2):

- heat rejection filter transmittance profile: $E_{hrf}(\lambda)$;
- lens/mirror optical efficiency: $E_{opt}(\lambda)$;
- filter transmittance spectral profile: $E_{filt}(\lambda)$.

With all these necessary corrections, Equation 9 can be written as follows:

$$G = \frac{4}{\pi} \cdot \pi R_{Sun}^2 \cdot \left[\frac{1 + e_M \cos(\psi_M)}{a_M (1 - e_M^2)} \right]^2 \cdot \tan^2 \left[\frac{FOV}{2} \right] \cdot EP \cdot |\cos(lat)| \cdot |\cos(MTA)| \quad \left[m^2 sr \right]$$

$$signal = \begin{cases} G \cdot \int_{530}^{570} \frac{2hc^2}{\lambda^5 \left[e^{\frac{hc}{\lambda kT}} - 1 \right]} \cdot A_M(\lambda) \cdot E_{opt}(\lambda) \cdot E_{filt}(\lambda) \cdot E_{hrf}(\lambda) \cdot d\lambda & (F550) \quad \left[\frac{W}{m^2} \right] \\ G \cdot \int_{730}^{770} \frac{2hc^2}{\lambda^5 \left[e^{\frac{hc}{\lambda kT}} - 1 \right]} \cdot A_M(\lambda) \cdot E_{opt}(\lambda) \cdot E_{filt}(\lambda) \cdot E_{hrf}(\lambda) \cdot d\lambda & (F750) \quad \left[\frac{W}{m^2} \right] \\ G \cdot \int_{860}^{900} \frac{2hc^2}{\lambda^5 \left[e^{\frac{hc}{\lambda kT}} - 1 \right]} \cdot A_M(\lambda) \cdot E_{opt}(\lambda) \cdot E_{filt}(\lambda) \cdot E_{hrf}(\lambda) \cdot d\lambda & (F880) \quad \left[\frac{W}{m^2} \right] \\ G \cdot \int_{400}^{900} \frac{2hc^2}{\lambda^5 \left[e^{\frac{hc}{\lambda kT}} - 1 \right]} \cdot A_M(\lambda) \cdot E_{opt}(\lambda) \cdot E_{filt}(\lambda) \cdot E_{hrf}(\lambda) \cdot d\lambda & (FPAN) \quad \left[\frac{W}{m^2} \right] \end{cases}$$

Equation 10: Real filter outgoing radiance.

The final step to obtain the acquired signal in photo-electrons (N_s) is to introduce all the hybrid Si-PIN CMOS detector characteristics and operative parameters:

- pixel Fill Factor (FF) that represents the pixel sensitive area percentage;
- detector Quantum Efficiency ($QE(\lambda)$) that represents the photon-electron conversion capability of the detector;
- number of detector pixels (N_{pix});
- detector exposure time (t_{exp}).

Equation 10 becomes:

$$\tilde{G} = G \cdot FF \cdot \frac{1}{N_{pix}} \cdot t_{\exp} =$$

$$= \frac{4}{\pi} \cdot \pi R_{Sun}^2 \cdot \left[\frac{1 + e_M \cos(\psi_M)}{a_M (1 - e_M^2)} \right]^2 \cdot \tan^2\left(\frac{FOV}{2} \right) \cdot EP \cdot |\cos(lat)| \cdot |\cos(MTA)| \cdot FF \cdot \frac{1}{N_{pix}} \cdot t_{\exp} \quad \left[\mathrm{m}^2 s \right]$$

$$N_S = \begin{cases} \tilde{G} \cdot \int_{530}^{570} \frac{\lambda}{hc} \cdot \frac{2hc^2}{\lambda^5 \left[e^{\frac{hc}{\lambda kT}} - 1 \right]} \cdot QE(\lambda) \cdot A_M(\lambda) \cdot E_{opt}(\lambda) \cdot E_{filt}(\lambda) \cdot E_{hrf}(\lambda) \cdot d\lambda & (F550) \quad \left[\frac{e^-}{m^2 s} \right] \\ \tilde{G} \cdot \int_{730}^{770} \frac{\lambda}{hc} \cdot \frac{2hc^2}{\lambda^5 \left[e^{\frac{hc}{\lambda kT}} - 1 \right]} \cdot QE(\lambda) \cdot A_M(\lambda) \cdot E_{opt}(\lambda) \cdot E_{filt}(\lambda) \cdot E_{hrf}(\lambda) \cdot d\lambda & (F750) \quad \left[\frac{e^-}{m^2 s} \right] \\ \tilde{G} \cdot \int_{860}^{900} \frac{\lambda}{hc} \cdot \frac{2hc^2}{\lambda^5 \left[e^{\frac{hc}{\lambda kT}} - 1 \right]} \cdot QE(\lambda) \cdot A_M(\lambda) \cdot E_{opt}(\lambda) \cdot E_{filt}(\lambda) \cdot E_{hrf}(\lambda) \cdot d\lambda & (F880) \quad \left[\frac{e^-}{m^2 s} \right] \\ \tilde{G} \cdot \int_{400}^{900} \frac{\lambda}{hc} \cdot \frac{2hc^2}{\lambda^5 \left[e^{\frac{hc}{\lambda kT}} - 1 \right]} \cdot QE(\lambda) \cdot A_M(\lambda) \cdot E_{opt}(\lambda) \cdot E_{filt}(\lambda) \cdot E_{hrf}(\lambda) \cdot d\lambda & (FPAN) \quad \left[\frac{e^-}{m^2 s} \right] \end{cases}$$

Equation 11: Image signal for each filter.

A critical aspect to underline regards the integration time (t_{exp}) value. Obviously, the longer is the exposure time the higher is the signal intensity. However, it shall be compatible with the conditions to avoid smearing due to the spacecraft motion during acquisition, according to the following constraint (Equation 12):

$$t_{sme} \leq \frac{1}{4} \cdot \frac{\text{pixel spatial dimension}}{\text{spacecraft on} - \text{ground velocity}} \quad [\mathrm{s}]$$

Equation 12: Integration time condition to avoid smearing.

which guarantees a good illumination for the detector and avoids significant blur of adjacent pixels signal.

Although the basic strategy is to use the maximum possible exposure time, under high back-reflected radiance intensity conditions and/or used filter (e.g.: FPAN instead of a broad-band filter), the pixel integration time can be lower than the one given by Equation 12 in order to avoid detector saturation (the accumulated charges exceed detector full-well capacitance).

Equation 13 reports the condition to avoid detector saturation:

$$N_S + offset : \begin{cases} > Fullwell \Rightarrow saturation \Rightarrow error \\ < Fullwell \Rightarrow correct \end{cases}$$

Equation 13: Detector saturation condition.

that can be used to determine the maximum exposure time to avoid detector saturation (Equation 14):

$$\begin{cases} \tilde{N}_S = \dfrac{N_S}{t_{\exp}} & \left[\dfrac{\mathrm{e}^-}{s}\right] \\ N_{off} = \dfrac{offset}{t_{\exp}} & \left[\dfrac{\mathrm{e}^-}{s}\right] \text{ (i.e. dark current)} \end{cases} \quad \Rightarrow \quad t_{sat} < \frac{Fullwell}{\tilde{N}_S + N_{off}} \ [\mathrm{s}]$$

Equation 14: Integration time condition to avoid saturation.

Another limitation in exposure time choice is the ROIC time resolution (t_{th}), which consists of the readout circuit cycle, the minimum time interval for a close/open cycle of the sensor CMOS matrix.

In conclusion, the selection of detector exposure time must respect three constraints: smearing, saturation and circuital threshold (Equation 15).

$$t_{\exp} = \max\{t_{th}; \min\{t_{sme}; t_{sat}\}\} = \max\left\{t_{th}; \min\left\{\frac{1}{4} \cdot \frac{\text{pixel spatial dimension}}{\text{spacecraft on} - \text{ground velocity}}; \frac{Fullwell}{\tilde{N}_S + N_{off}}\right\}\right\} \ [\mathrm{s}]$$

Equation 15: Detector exposure time definition rule.

Figure 24 and Figure 25 show the exposure time profile in two typical operative conditions and considering different albedo coefficients.

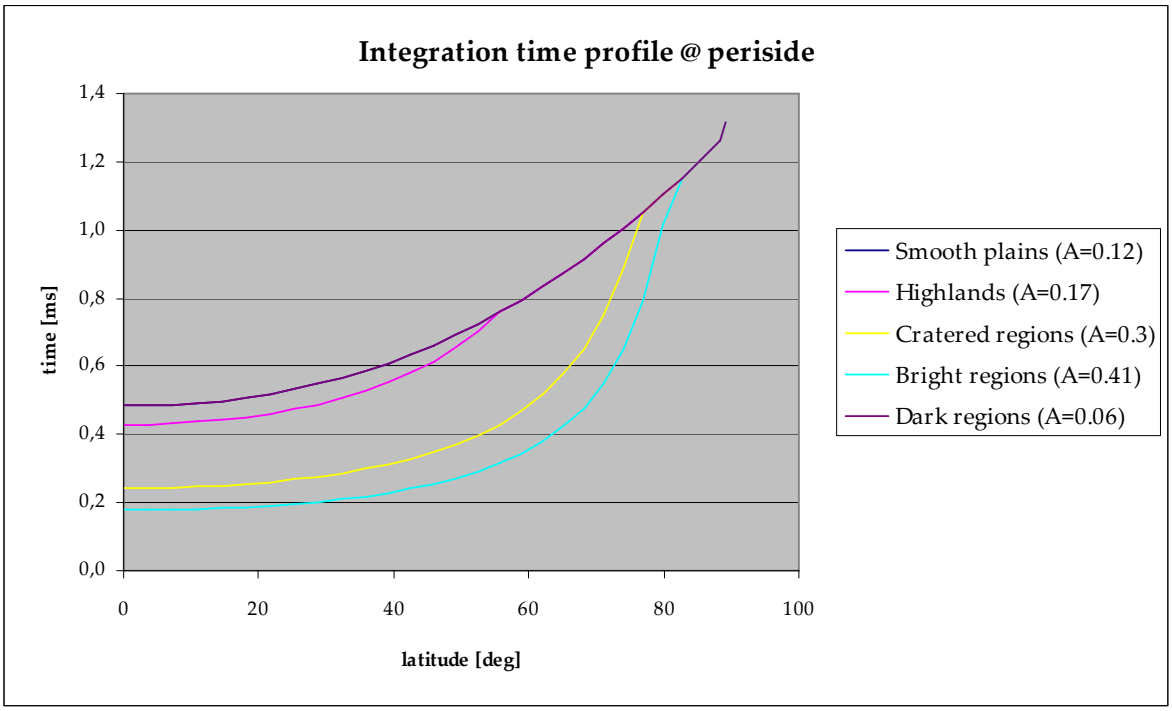

Figure 24: Integration time profile for different albedo coefficients for spacecraft at 400 km of altitude.

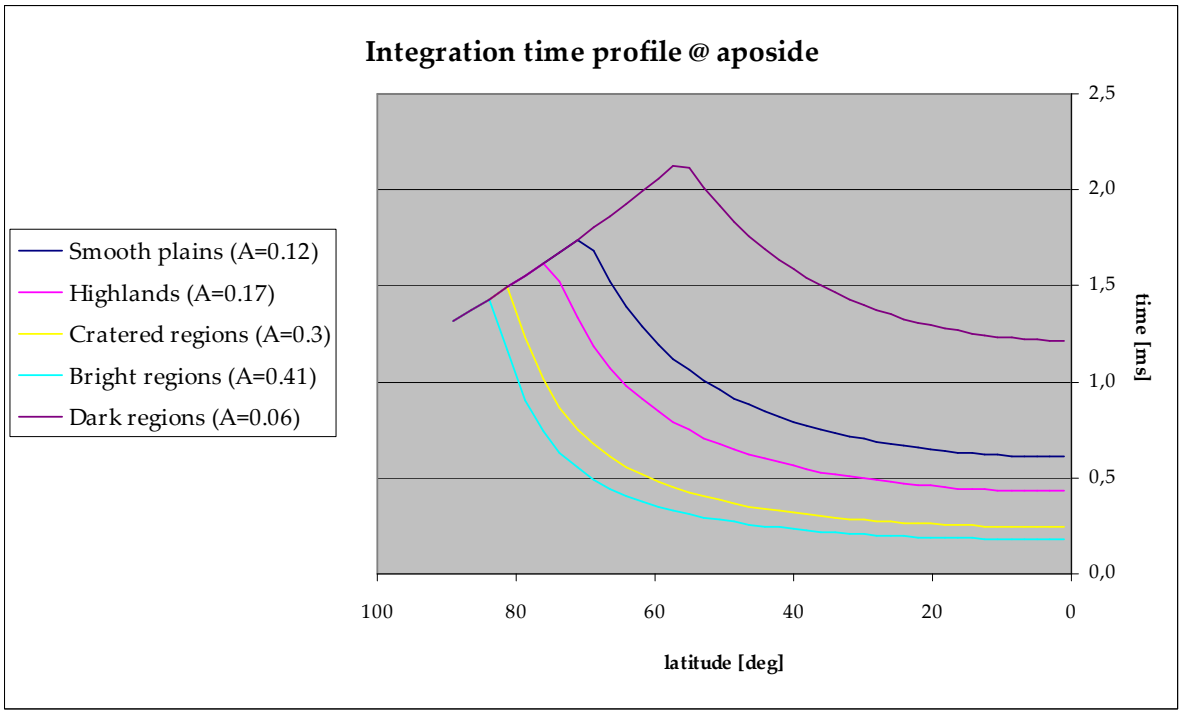

Figure 25: Integration time profile for different albedo coefficients for spacecraft at 1500 km of altitude.

Finally Figure 26, Figure 27 and Figure 28 report the detector Quantum Efficiency ($QE(\lambda)$), the Heat Rejection Filter ($E_{hrf}(\lambda)$) and the Optics ($E_{opt}(\lambda)$) efficiency profiles, respectively.

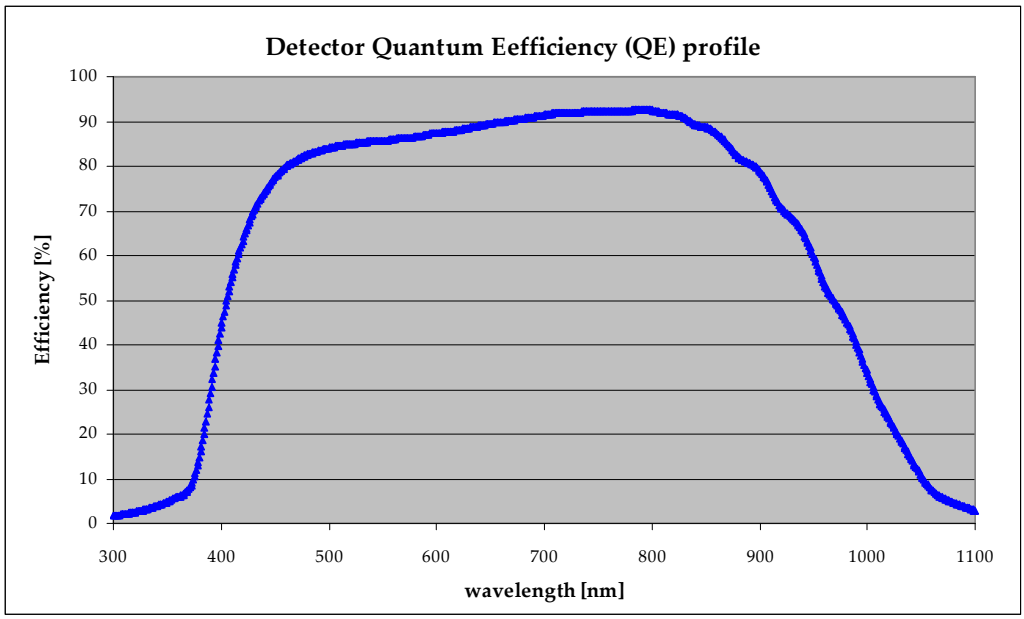

Figure 26: Detector Quantum Efficiency (QE) spectral efficiency profile.

Detector QE is well above 80% in the relevant spectral range (400 ÷ 900 nm); this guarantees very good performances in photon-electron conversion process. In addition, the detector QE profile increases towards longer wavelengths, compensating to some extent the Mercury low emittance in the F880 filter.

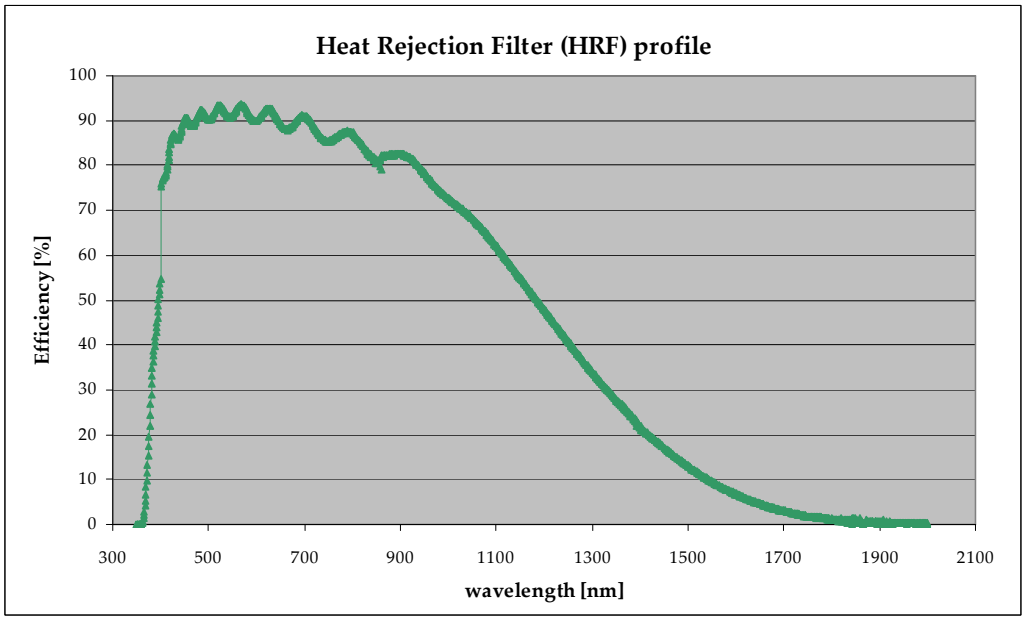

Figure 27: Heat Rejection Filter (HRF) spectral efficiency profile.

Heat Rejection Filter reflects more than 90% above 1500 nm to limit the thermal contribution to image formation.

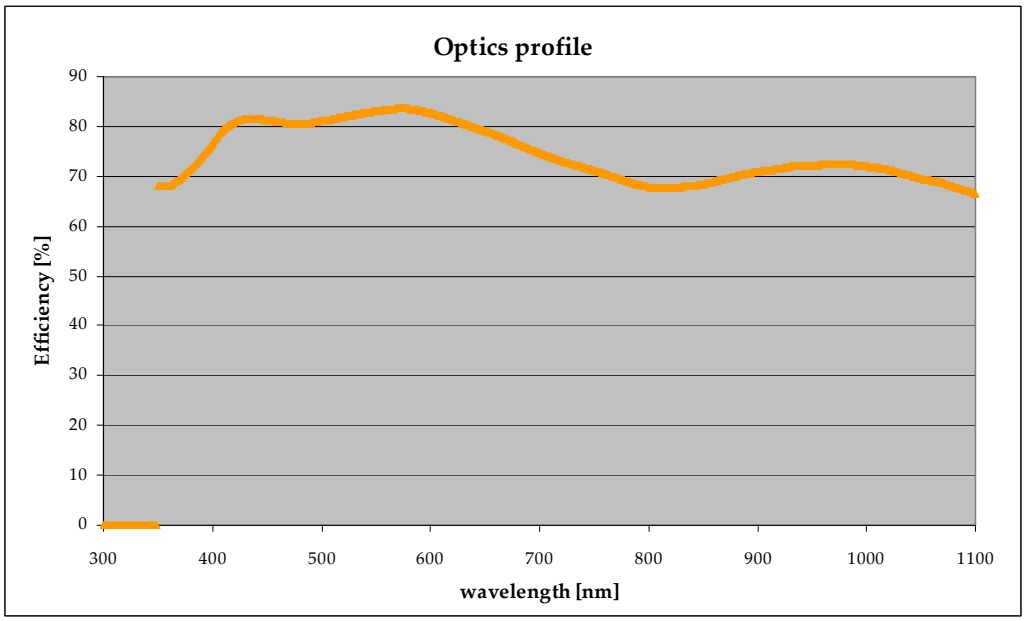

Figure 28: Optics spectral efficiency profile.

Optics efficiency (> 68% in the relevant spectra range) guarantees a good light transmittance towards the FPA.

3.1.1.3 Noise

Equation 11 is used to determine the image signal intensity (in electrons) for each filter and in each pixel of the HRIC Si-PIN CMOS detector. Of course, many degradation effects (noises) concur to modify the ideal behaviour of this photo-electronic element, affecting the recovered signal. In addition, ROIC and the Proximity Electronics (PE) electronic components (e.g.: amplifiers, …) introduce spurious signals that are present in the acquired data. These additional inputs can be divided in two families depending on their local/global effects:

1. On pixel:

   This noise category consists of:

   - Photon noise (σ_S): it consists of photons fluctuation in the radiant flux of every light source (photon shot noise – [48] Chapter 4.2.1). Its magnitude directly depends on the intensity of the light and/or on the exposure time. From a statistical point of view, photon noise is modelled with Poisson distribution:

$$P(x) = \frac{e^{-\lambda}\lambda^{x}}{x!}$$

$\lambda(>0)$ expected number of events (photons) in the considered time interval
$x(\geq 0)$ number of events (photons)

Equation 16: Poisson distribution.

For large numbers of events (as it is when considering a photons flux) the Poisson distribution approaches a normal distribution, in which the standard deviation is equal to the square root of the average number of photons.

$$\sigma_S = \sqrt{N_S} \quad [e^-]$$

Equation 17: Photon shot noise standard deviation.

   - Dark Current (σ_{DC}): it consists of a spontaneous and continuous release of charges (N_{dark}) due to the molecular thermal agitation in the HRIC detector (thermal noise – [48] Chapter 3.6).

$$N_{dark} = \frac{J_D \cdot A_D \cdot t_{\exp}}{q} \quad [e^-]$$

$$\begin{cases} J_D & \text{dark current density} \propto T & \left[\frac{nA}{cm^2}\right] \\ A_D & \text{pixel area} & [cm^2] \\ q & \text{electron charge} & [Coulomb] \end{cases}$$

Equation 18: Dark current expression.

Its magnitude depends directly on the exposure time and on the detector temperature. Generally, its contribution can be easily reduced (by subtraction) during data calibration; unfortunately, as for the photon shot noise, the dark current is characterised by a fluctuation of the electrons flux following a Poisson distribution (dark current shot noise – [48] Chapter 4.2.1), which becomes a null-mean normal one (very large number of events) where the standard deviation is:

$$\sigma_{DC} = \sqrt{N_{dark}} \quad [\mathrm{e}^-]$$

Equation 19: Dark current shot noise standard deviation.

Dark current effects can be reduced only by cooling the detector considering that, in general, the dark current density is halved every 8-9 °C.

- Readout noise (σ_{ro}): this is an electronic noise associated to the detector readout process. Its principal component consists of a spurious signal (kTC noise – [48] Chapter 4.2.2) induced by the reset circuit during sensor charge transfer (circuital leakage). From a statistical point of view, the reset noise is modelled with a normal distribution with null mean and standard deviation equal to:

$$\sigma_{reset} = \frac{\sqrt{kTC}}{q} \quad [e^-]$$

Equation 20: Reset noise standard deviation.

where k is the Boltzmann constant, T is the absolute temperature of the circuit and C is the parasitic capacitance responsible for the leakage.

Reducing capacitance size is the best way to limit the reset noise effects; such a solution helps also in increasing the device output gain conversion. In addition, detector cooling is a possible alternative solution.

- Off-chip amplifier noise ($\sigma_{off-chip}$): this degradation term derives from the combination of 1/f noise (or pink noise) and white noise. It can be described by three elements: the noise spectral density (ν_n) at f_{knee} frequency (where the two noise components are equal), the noise equivalent bandwidth (B_n) and the detector sensitivity (k_n).

$$\sigma_{off-chip} = \nu_n \cdot \frac{\sqrt{B_n}}{k_n} \quad [e^-]$$

$$B_n \propto \text{readout rate} \quad \left[\frac{pxl}{s}\right]$$

Equation 21: Off-chip noise standard deviation.

- Quantization noise (σ_{ADC}): this noise term is associated to the analogue to digital conversion process (Figure 29).

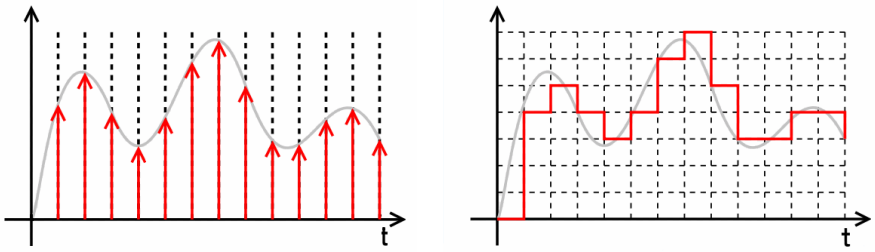

Figure 29: Sampling (left) and quantization (right) processes of an ADC.

After the time sampling of the input analogue signal, the Analogue-to-Digital-Converter (ADC) assigns the closest codified level to the sample amplitude introducing an error which is uniformly distributed between $\pm \Delta/2$ (half quantization step). The equivalent expression in electrons of the quantization noise standard deviation is:

$$\sigma_{ADC} = \frac{\Delta}{\sqrt{12}} \quad [e^-]$$

$$\Delta = \text{quantization level amplitude} = \frac{\text{detector Fullwell}}{2^{2\#\_bit}}$$

Equation 22: Quantization noise standard deviation.

Increasing the number of ADC conversion bits helps in reducing quantization noise magnitude, but increases the system sensitivity to noise.

2. On frame:

   This noise category consists of:

   - Photo Response Non Uniformity (σ_{PRNU}): this term accounts for the variation of photo-response across the different pixels of the HRIC detector. It is a signal-dependent noise and is a multiplicative factor of the photoelectrons number. In the linear responsivity region, it is expressed as a fraction of the total number of charge carriers ([48] Chapter 4.2.6). In case of normal distribution modelling, the standard deviation of the photo-response non uniformity noise component is expressed by:

$$\sigma_{PRNU} = PRNU \cdot N_s \quad [e^-]$$

Equation 23: Photo Response Non Uniformity noise component standard deviation.

In normal operative conditions, PRNU is the frame dominant noise component for most arrays.

   - Dark Current Non Uniformity (σ_{DCNU}): similarly to PRNU, this noise component accounts for the variation in dark current production between detector pixels. It is usually expressed as an RMS fraction of the nominal dark current. Standard deviation of the associated noise term is:

$$\sigma_{DCNU} = DCNU \cdot N_{dark} \quad [e^-]$$

Equation 24: Dark Current Non Uniformity noise component standard deviation.

Being related to pixel dark current, detector cooling is indicated to reduce DCNU magnitude.

- Fixed Pattern Noise (σ_{FPN}): this term is related to offset variations between different pixels across the sensitive array after repeating several times reset operation. The standard deviation of such an offset is:

$$\sigma_{FPN} = \frac{FPN_{volt}}{k_n} \quad [e^-]$$

Equation 25: Fixed Patter Noise component standard deviation.

3.1.1.4 Spurious charge

Spurious charge is a degradation component that affects the detector output signal. It consists in parasitic charge storage in the ROIC and/or detector Si-PIN cells which determines an increment of the output signal level.

The real effect of spurious charge depends on two factors:

1. temperature: the rate of free charges depends linearly on the operative temperature of the detector and the ROIC;
2. read-out time: free charges accumulate in time so that the amount of spurious charge in each pixel depends on the time lag between image acquisition and reading.

As a result, at frame level, spurious charge affects output image with a spatial variant offset that increases with respect to the detector readout sequence. This offset can be easily reduced by means of a proper instrument calibration; the spurious charge shot noise (as for the photon noise and the dark current) could be a new noise component in the SNR formulation that requires to be modelled.

In addition, as for the PRNU and DCNU, a sort of non-homogeneity in spurious charge accumulation between the detector pixels is expected. This effect, named as Spurious Charge Non Uniformity (SPNU) implies an effect on the overall image, whose reduction must be carefully defined and planned in order to not introduce a larger correction noise.

3.1.2 The Radiometric Model as HRIC performance analysis tool

HRIC-RM parameters are reported in Table 5.

Par name	Value	Par name	Value	Par name	Value
EP [cm^2]	52.9	PRNU [%]	2	k_n [μV/e$^-$]	14
FOV [mrad]	25.6	DCNU [%]	10	B_n [MHz]	20
Fullwell [ke$^-$]	120	N_{dark} [e$^-$/s]	10000	FPN_{volt} [V]	15
t_{th} [ms]	0.1	σ_{ro} [e$^-$]	60	T [K]	273-293
ADC_{bit}	14	ν_n [V/Hz^{½}]	$2 \cdot 10^{-8}$	C [fF]	16

Table 5: HRIC Radiometric Model input parameters.

Without loss of generality, HRIC-RM is organised in two sections related to the two extreme operative conditions:

- periside arc: in this case the spacecraft is close to the planet surface so that the HRIC can observe specific superficial targets at the maximum spatial resolution (5 m/pxl). Due to thermal constraints, this operative condition is realised when Mercury is at its aphelion, where (Figure 20) the Solar constant is lower (6272 W/m^2).
- aposide arc: when Mercury is at its perihelion the spacecraft shall be as far as possible from the planet surface to avoid thermal (Solar constant is at 14448 W/m^2) and radiation problems (Figure 20). In this case the spatial resolution is lower (15-19 m/pxl) and wide surface coverage is the principal operative goal of the camera.

For both the above operating conditions, HRIC-RM allows us to estimate the quality of observations through the pixel and frame SNR parameters:

$$SNR = \frac{s(e^-)}{n(e^-)} = \begin{cases} pixel & \Rightarrow \dfrac{s(e^-)}{\sqrt{\sigma_S^2 + \sigma_{DC}^2 + \sigma_{ro}^2 + \sigma_{off-chip}^2 + \sigma_{ADC}^2}} \\ frame & \Rightarrow \dfrac{s(e^-)}{\sqrt{\sigma_S^2 + \sigma_{DC}^2 + \sigma_{ro}^2 + \sigma_{off-chip}^2 + \sigma_{ADC}^2 + \sigma_{PRNU}^2 + \sigma_{DCNU}^2 + \sigma_{FPN}^2}} \end{cases}$$

Equation 26: Signal to Noise Ratio (pixel and frame) formulation.

Figure 30 and Figure 31 report the SNR-pixel and SNR-frame profiles, respectively, for the periside operative arc and the panchromatic filter.

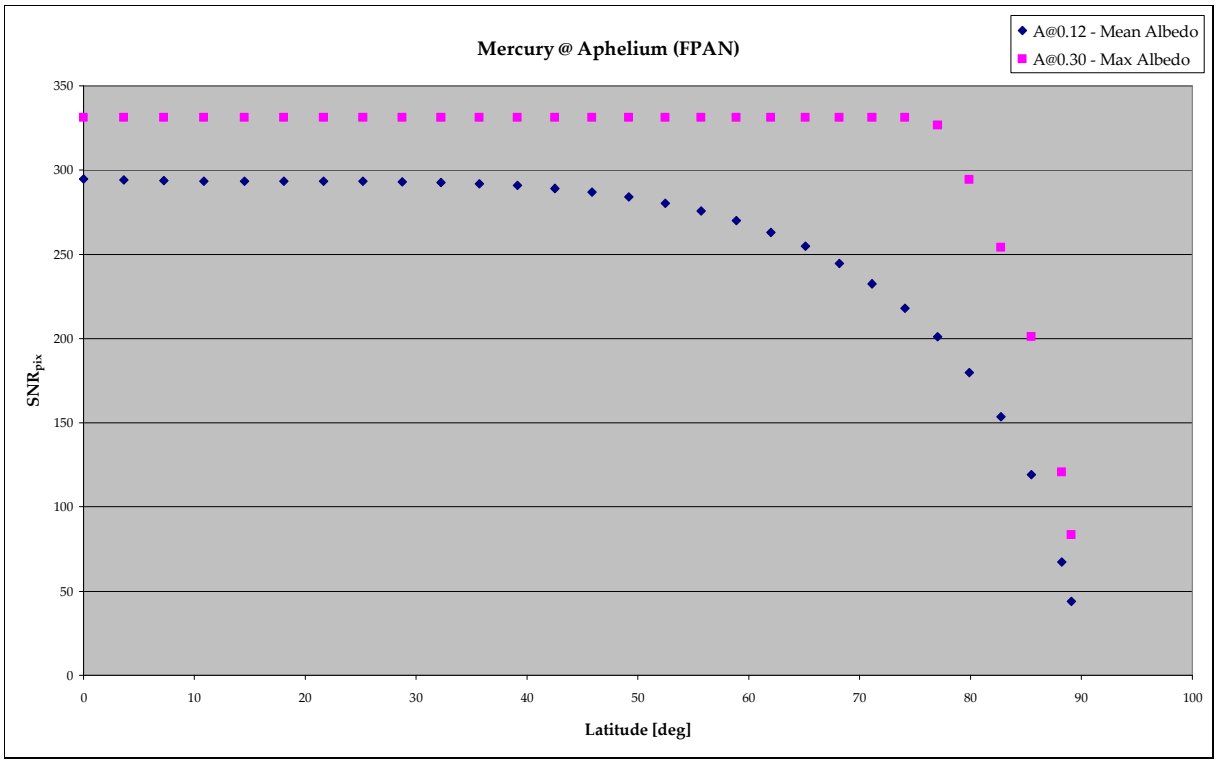

Figure 30: Expected on-pixel panchromatic SNR profile along the periside arc.

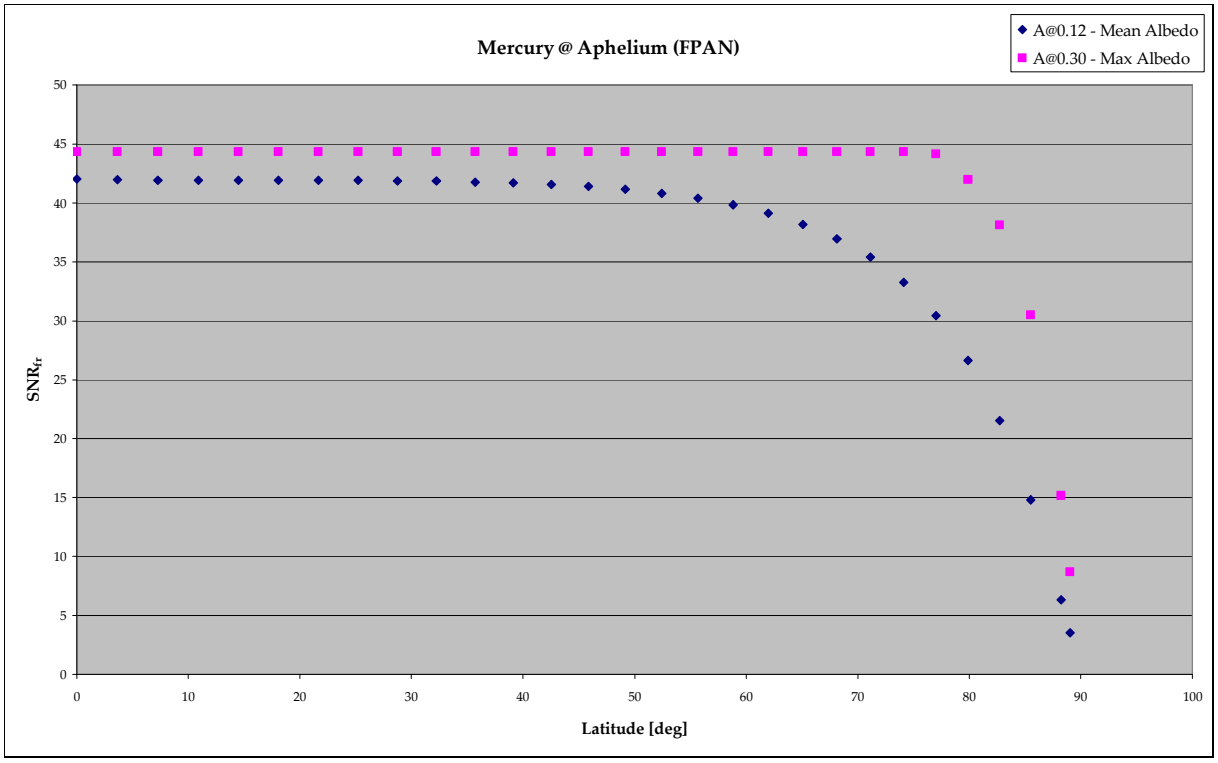

Figure 31: Expected on-frame panchromatic SNR profile along the periside arc.

The two above profiles indicate that the expected signal quality is very high, close to the possible maximum (i.e., ideal detector, only photon noise or photon noise non uniformity contribution). In fact, considering a saturated input signal, SNR-pixel can be equal to the square root of the Fullwell at maximum (~346) while SNR-frame is upper limited by the PRNU (SNR at 50).

Figure 32 and Figure 33 report the SNR-pixel and SNR-frame profiles, respectively, for the aposide operative arc and the F880 filter.

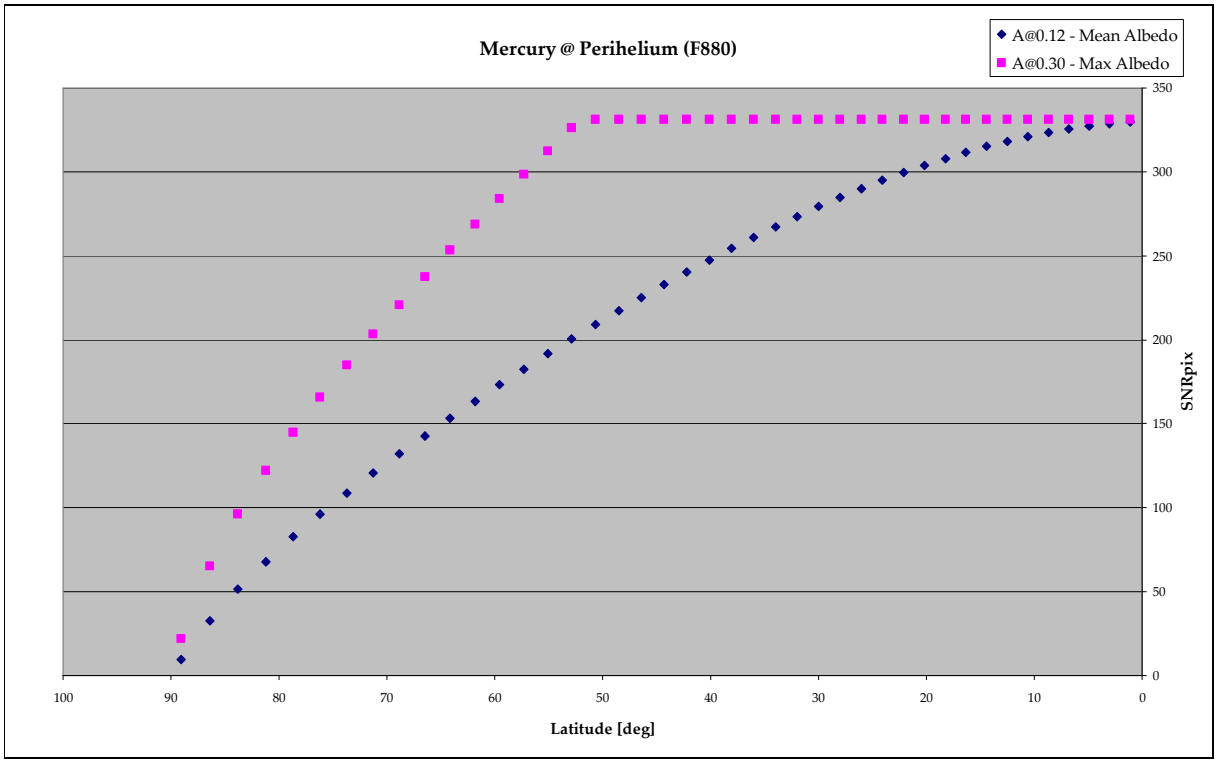

Figure 32: Expected on-pixel F880 SNR profile along the aposide arc.

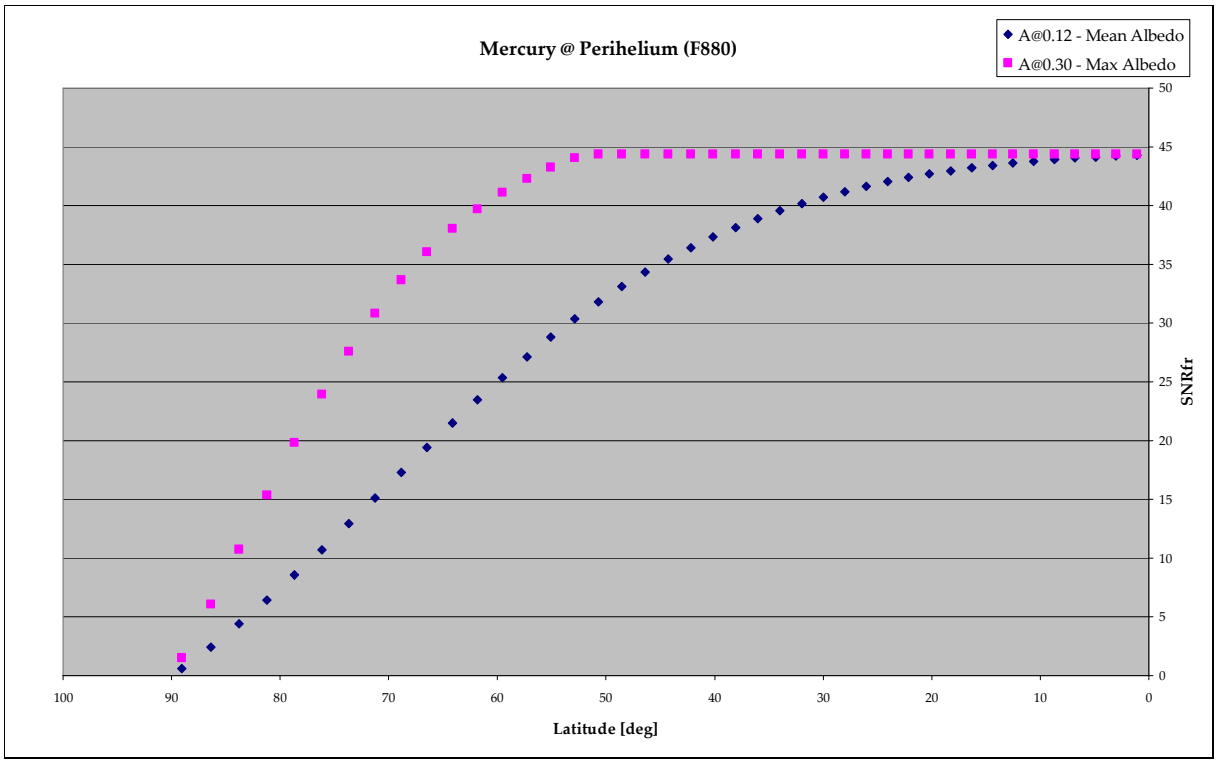

Figure 33: Expected on-frame F880 SNR profile along the aposide arc.

The two above profiles indicate that HRIC will operate very well (high SNR values) even on the aposide arc.

Finally, the above graphs report only two examples of HRIC-RM SNR outputs: setting input parameters to the desired configuration, HRIC-RM can estimates the SNR profile on pixel and on frame in every operative condition.

3.2 *HRIC Simulator*

The High Resolution Imaging Channel – SIMulator (HRIC-SIM) is an interactive extension of the HRIC-RM that directly operates on images. HRIC-SIM is built to give a visual estimation of the quality of the HRIC system. Starting from an analytical description of the instrument optical layout and HRIC-RM equations, HRIC-SIM applies on a possible input scene (synthetic or realistic image) all the image quality degradation processes (system MTF, filters response and noise contribution).

In the following a brief introduction on the Modulation Transfer Function (MTF) and some considerations about spatial frequency domain are presented; subsequently, the HRIC-SIM tool is presented with particular attention on how the HRIC-RM equations are introduced into the simulation tool. Finally, some results are reported.

3.2.1 HRIC optical PSF, MTF and image quality

The Point Spread Function (PSF) is the response to the impulse of an optical system ([48] Chapter 9.1.2); it indicates how the optical design of an imaging system spreads light on a detector (Figure 34). In a diffraction-limited configuration with circular aperture, PSF consists into a bi-dimensional Sinc-like function (Equation 27).

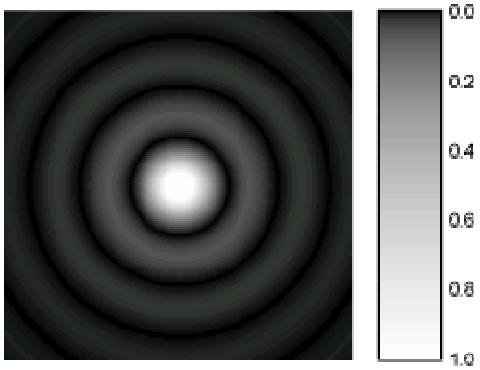

Figure 34: Diffraction limited Point Spread Function (PSF).

$$PSF(r) = \left[\frac{2J_1\left(\pi Dr / \lambda f \right)}{\pi Dr / \lambda f} \right]^2 = \left[\frac{2J_1\left(\pi r / \lambda F_{\#} \right)}{\pi r / \lambda F_{\#}} \right]^2$$

$$\begin{cases} D & = \text{optical aperture} \\ f & = \text{focal length} \\ F_{\#} & = \text{focal ratio} \\ J_1(\cdot) & = \text{first order Bessel function} \end{cases}$$

Equation 27: Diffraction limited Point Spread Function (PSF) for a circular aperture.

PSF is characterised by two fundamental parameters which define the performances of an optical system in terms of resolution and sharpness:

1. Airy disk: it consists of the central PSF bright disk whose radius r_0 (Equation 28) defines the angular resolution of a diffraction limited optical design: two adjacent light point sources are resolvable (detectable signal fluctuation) if the Airy disk centre of the first one occurs in the first minimum of the Airy disk of the second (Figure 35 – Rayleigh criteria);

$$sen(\theta) = 1.22\left(\frac{\lambda}{D}\right)$$

$$r_0 = tg(\theta)\cdot f \cong \theta \cdot f = 1.22(\lambda \cdot F_{\#})$$

$$\begin{cases} \theta & = \text{optical angular resolution} \\ \lambda & = \text{wavelength} \\ f & = \text{focal length} \\ D & = \text{Pupil aperture (diameter)} \\ F_{\#} & = \text{focal ratio} \end{cases}$$

Equation 28: Airy disk radius.

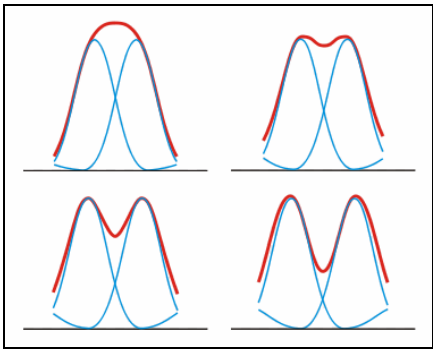

Figure 35: Un-resolved (top) and resolved (bottom) light spots.

2. Encircled Energy (EE) disk: it consists of a circle concentric to the Airy disk that contains 80-84% of signal energy. In optical system design, it is considered as a measure of image sharpness: as it widens, adjacent point sources PSF's blur.

In general these two parameters are in contrast to each other due to the PSF formulation: as the Airy disk shrinks, PSF secondary lobes become more intense and the encircled energy disk widens.

The Airy and the EE disks are not the only quality parameters involved in an imaging system development. Another key factor is the detector sampling step (pixel) which defines the minimum detectable period for a feature (i.e., spatial resolution).

As a result, finding the best performance of an optics-detector configuration is a task that, in general, requires to proceed along a critic trade-off process between optical detection capabilities, image sharpness and detector resolution requirements.

Such a process is usually performed in the Fourier domain where it is easier to evaluate the optics-detector design performances. The comparison is performed by considering:

1. optical Modulation Transfer Function (MTF): it consists of the magnitude of the PSF Fourier's transform and it represents the spatial frequency response of an optical design. The MFT profile shows how each spatial frequency component of an image spatial spectrum is modulated. Its Gaussian-like shape indicates that higher spatial frequency components experiment higher attenuation factors (Figure 36) determining a loose of feature sharpness and a general image contrast reduction.

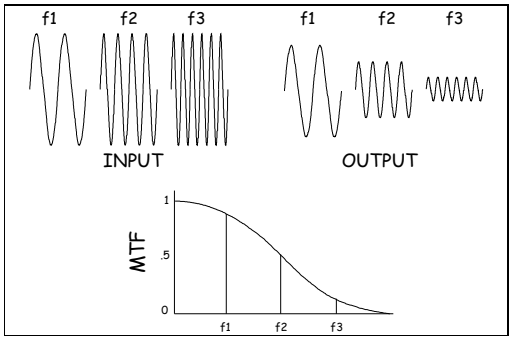

Figure 36: Modulation Transfer Function (MTF) profile.

Last "accepted" spatial frequency component is the cut-off frequency (Equation 29):

$$\nu_C = \frac{1}{\lambda \cdot F_{\#}}$$

Equation 29: MTF cut-off frequency expression.

In an obscured Ritchey-Chrétien configuration (HRIC design), the optical MTF can be derived as follows:

$$MTF_{optic}(\nu) = \frac{A(\nu) + B(\nu) + C(\nu)}{1 - \varepsilon^2}$$

$$A(\nu) = \begin{cases} \frac{2}{\pi} \cdot \left[\cos^{-1}\left(\frac{\nu}{\nu_C}\right) - \frac{\nu}{\nu_C} \cdot \sqrt{1 - \left(\frac{\nu}{\nu_C}\right)^2} \right] & 0 \le \frac{\nu}{\nu_C} \le 1.0 \\ 0 & \frac{\nu}{\nu_C} > 1.0 \end{cases}$$

$$B(\nu) = \begin{cases} \frac{2\varepsilon^2}{\pi} \cdot \left[\cos^{-1}\left(\frac{\nu}{\nu_C \cdot \varepsilon}\right) - \frac{\nu}{\nu_C \cdot \varepsilon} \cdot \sqrt{1 - \left(\frac{\nu}{\nu_C \cdot \varepsilon}\right)^2} \right] & 0 \le \frac{\nu}{\nu_C \cdot \varepsilon} \le 1 \\ 0 & \frac{\nu}{\nu_C \cdot \varepsilon} > 1.0 \end{cases}$$

$$C(\nu) = \begin{cases} -2\varepsilon^2 & 0 \le \frac{\nu}{\nu_C} \le \frac{(1-\varepsilon)}{2} \\ \frac{2}{\pi} \cdot \left[\varepsilon \cdot \sin(\phi) + \left(\frac{\phi}{2}\right) \cdot (1+\varepsilon^2) - (1-\varepsilon^2) \cdot \tan^{-1}\left(\frac{1+\varepsilon}{1-\varepsilon} \cdot \tan\left(\frac{\phi}{2}\right)\right) \right] - 2\varepsilon^2 & \frac{(1-\varepsilon)}{2} \le \frac{\nu}{\nu_C} \le \frac{(1+\varepsilon)}{2} \\ 0 & \frac{\nu}{\nu_C} \ge \frac{(1+\varepsilon)}{2} \end{cases}$$

$$\phi = \cos^{-1}\left(\frac{(1+\varepsilon^2) - 4 \cdot \left(\frac{\nu}{\nu_C}\right)^2}{2\varepsilon} \right) \qquad \varepsilon = \frac{D_{obscuration}}{D_{optic}}$$

Equations 30: Optical MTF calculation in an obscured optical configuration.

2. Nyquist frequency (ν_N): it is the highest spatial frequency component the detector is able to reproduce (Equation 31).

$$\nu_N = \frac{1}{2 \cdot p}$$

Equation 31: Detector Nyquist frequency.

where p is the detector pixel pitch (10 µm).

In sampling theory, ν_N represents the spatial frequency threshold to avoid spatial frequency recombination (i.e. aliasing).

3. image spatial spectrum: it is the Fourier transform of the input image and represents the distribution of the spatial frequency components that governs size, shape, orientation etc. of features and/or patterns in the image.

In practice, the trade-off process is performed comparing only optical MTF and Nyquist frequency, assuming that the image spatial spectrum is MTF-like, especially for what concerns the spatial frequency band. This limiting assumption (input image cannot contain features whose relative spatial frequency components are higher than the optical cut-off frequency) derives from the necessity to define the best detector sampling rate solution.

In ideal conditions, sampling detector performances must respect the Nyquist law [49]:

$$\frac{\text{sensor sampling frequency}}{\text{input image spatial bandpass}} = \frac{1/p}{1/(\lambda \cdot F_{\#})} = \frac{\lambda \cdot F_{\#}}{p} = 2$$

Equation 32: Ideal ratio between detector sampling capabilities and input image band-pass.

This condition is mandatory to avoid aliasing because it assures a good separation between different image spatial spectrum replicas generated during sampling process.

Unfortunately, given the MTF-like distribution of image spatial spectrum, respecting Nyquist condition means that the magnitude of Nyquist frequency component is null: in fact, as the sensor sampling frequency is two times the input image spatial band-pass ($\lambda \cdot F_{\#} / p = 2$) the MTF profile goes to zero at detector Nyquist frequency (Figure 37). As a result, even if the detector sampling rate is compatible with the image spatial spectrum bandwidth, it cannot reveal image features at the Nyquist frequency.

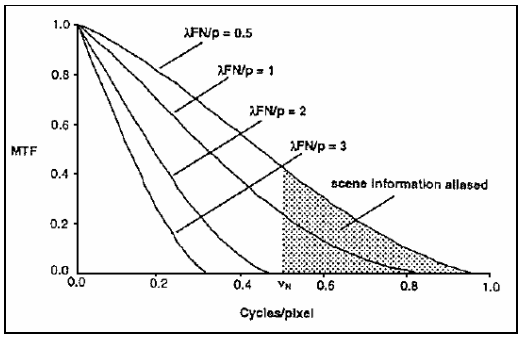

Figure 37: Comparison between detector sampling rate and MTF bandwidth.

We recall that HRIC scientific objectives are to:

1. detect features whose dimensions are comparable with pixel size on-ground projection;
2. follow signal fluctuations whose period is equal to the dimension of two pixels.

Such stringent requirements imply to reduce the Equation 32 ratio in order to increase the magnitude of the Nyquist frequency component, even if a certain degree of aliasing can occur.

In HRIC imaging system the high spatial resolution requirement of 5 m/pxl combined with the narrow FOV of 1.47 degree and the on-axis optical layout imposes to significantly reduce the $\lambda \cdot F_{\#} / p$ ratio; in particular, the ratio between detector sampling rate and input image spatial bandwidth is four times lower on average (Equation 33).

$$\frac{\lambda \cdot F_{\#}}{p}(HRIC) \in \left[\underbrace{0.3}_{\lambda=400nm} \; ; \; \underbrace{0.8}_{\lambda=900nm} \right] < 2$$

Equation 33: HRIC detector sampling capabilities.

Such a stringent result implies that HRIC imaging system could experience some critical aliasing effect (the mean sampling rate is 4 times lower than the Nyquist condition).

Actually, when studying aliasing effects there are two aspects to take into account:

1. original image spatial spectrum: aliasing effects are present only if the original image is characterised by spatial frequency components greater than the detector sampling one. This means that the magnitude of aliasing effects depends on the

image spatial frequency content (e.g.: smooth plain → negligible aliasing effects; heavily cratered regions with rays → critical aliasing effects).

2. real visual effects: Figure 37 shows that MTF modulation of spatial frequencies just below the Nyquist component increases as the $\lambda \cdot F_{\#} / p$ parameter reduces. This means that although more aliasing occurs as $\lambda \cdot F_{\#} / p$ decreases, the higher optical MTF profile below the Nyquist frequency causes that image edges appear sharper [49];

In addition, an imaging system configuration characterised by a ratio lower than in Equation 32 benefits of an improved SNR (Equation 34): for a given spectral interval $[\lambda_{\min}; \lambda_{\max}]$ halving the $\lambda \cdot F_{\#} / p$ coefficient implies that the signal strength quadruples:

$$S = \frac{\pi \cdot p^2 \cdot t_{\exp}}{4 \cdot F_{\#}^2} \cdot \int_{\lambda_{\min}}^{\lambda_{\max}} QE(\lambda) \cdot E_{opt}(\lambda) \cdot L_M(\lambda) d\lambda$$

Equation 34: MTF and SNR relation.

Equation 34 indicates that for a given spectral band-pass $[\lambda_{\min}; \lambda_{\max}]$ the image signal is inversely proportional to $[\lambda \cdot F_{\#} / p]^2$. As consequence, if the $\lambda \cdot F_{\#} / p$ is halved the signal power increase of a factor of 4 determining, in the case of constant noise contribution, a significant improvement in SNR [49].

Figure 38 reports the optical MTF profile for all the filters (panchromatic and three broad band) of the HRIC design.

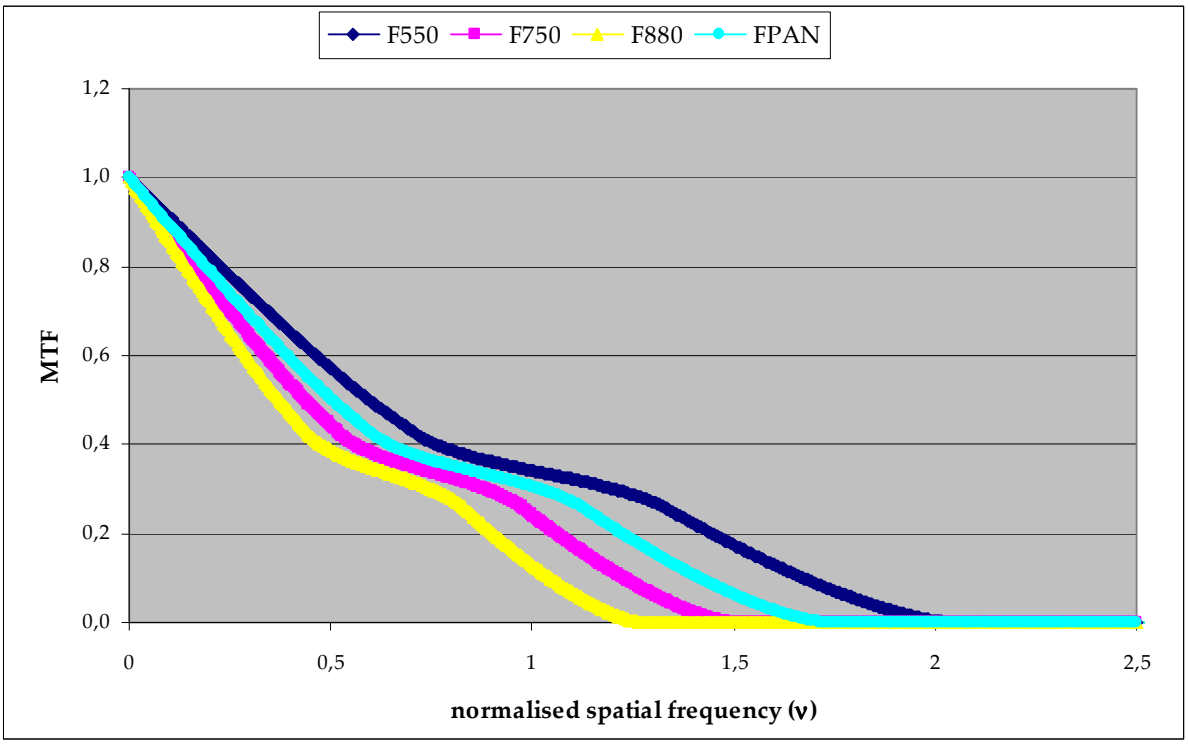

Figure 38: Optical MTF profiles for the HRIC panchromatic and broad-band filters at their central spectral frequency. Spatial frequencies are normalised with respect to detector sampling frequency (1/p = 1 lines/pxl).

As a final consideration, it is important to analyse what Equation 32 implies on the PSF dimensioning with respect to the detector pixel size. Nyquist condition implies that the optical angular resolution (Equation 28) subtends at least 2 pixels, in nominal operative conditions on the periside arc; this corresponds to an on-ground fluctuation period of about 10 metres (HRIC resolution requirement).

Unfortunately, as shown in Figure 37 satisfying the Nyquist condition means that the signal magnitude at the Nyquist frequency is null and so the relative feature is not detectable by the detector. Again, the only solution is to reduce the detector sampling rate which implies that, for a given optical design (fixed MTF), the Airy disk shrinks with respect to the detector pixel size. As a result, in HRIC imaging system design, the Airy disk diameter is comparable with the detector pixel size.

3.2.2 System MTF

The MTF described in the previous section represents the optical component of a system MTF (MTF-SYS). Actually, there are other additional terms which are related to detector sampling capabilities (finite pixel size), optical and detector aberrations and pointing variations ([48] Chapter 10). Equation 35 reports the complete MTF-SYS formulation:

$$\mathrm{MTF}_{\mathrm{sys}} = \mathrm{MTF}_{\mathrm{optic}} \cdot \mathrm{MTF}_{\mathrm{detector}} \cdot \mathrm{MTF}_{\mathrm{motion}} \cdot \mathrm{MTF}_{\mathrm{optical\_aberr}} \cdot \mathrm{MTF}_{\mathrm{detector\_aberr}} \cdot \mathrm{MTF}_{\mathrm{jitter}}$$

Equation 35: System MTF terms and calculation.

In the following all the MTF-SYS components are described:

1. $\mathrm{MTF}_{\mathrm{detector}}$: in the previous paragraph (3.2.1) sampling rate requirement has been discussed considering a infinitesimal (in size) pixel. In the Fourier domain, finite linear integration is modelled as follows ([48] Chapter 10.3):

$$MTF_{\mathrm{detector}}(\nu) = \left|\mathrm{sinc}(p \cdot \nu)\right|$$

Equation 36: Detector MTF component.

2. $\mathrm{MTF}_{\mathrm{motion}}$: during HRIC acquisition (t_{exp}) a relative displacement between optical system and observed scene occurs (spacecraft motion along its orbit) determining a blurring effect oriented along-track, that is modelled as follows ([48] Chapter 10.5):

$$MTF_{\mathrm{motion}}(\nu) = \left|\mathrm{sinc}(\Delta p \cdot \nu)\right| \quad \Delta p = \frac{\mathrm{dwell\_time}}{t_{\mathrm{exp}}}$$

Equation 37: Motion MTF component.

3. $\mathrm{MTF}_{\mathrm{optical\text{-}aberr}}$: optics misalignment and/or manufacturing limitations may reduce the optical performance of the system. A linear attenuation of spatial frequency components is expected:

$$MTF_{\mathrm{optical\_aberr}}(\nu) = 1 - k_{\mathrm{optic\_aberr}} \cdot \nu$$

Equation 38: Optical aberration MTF component.

where $k_{optical\_aberr}$ is the optical aberration coefficient.

4. $MTF_{detector\text{-}aberr}$: type and relevant technology of detector affect detector responsivity. A linear attenuation of spatial frequency components is expected:

$$MTF_{detector\_aberr}(\nu) = 1 - k_{detector\_aberr} \cdot \nu$$

Equation 39: Detector aberration MTF component.

where $k_{detector\_aberr}$ is the detector aberration coefficient.

5. MTF_{Jitter}: jitter can be figured out starting from the camera pointing stability. A high frequency random motion affects the image quality in both the along and across track directions. Assuming a Gaussian distribution for the random movements, MTF_{Jitter} can be modelled as follows ([48] Chapter 10.5.2):

$$MTF_{Jitter}(\nu) = e^{-2\cdot(\pi\cdot\sigma_{jitter}\cdot\nu)^2}$$

Equation 40: Random motion (Jitter) MTF component.

where σ_{Jitter} is the random displacement.

Figure 39 shows all the MTF-SYS components and the resulting profile (thin line).

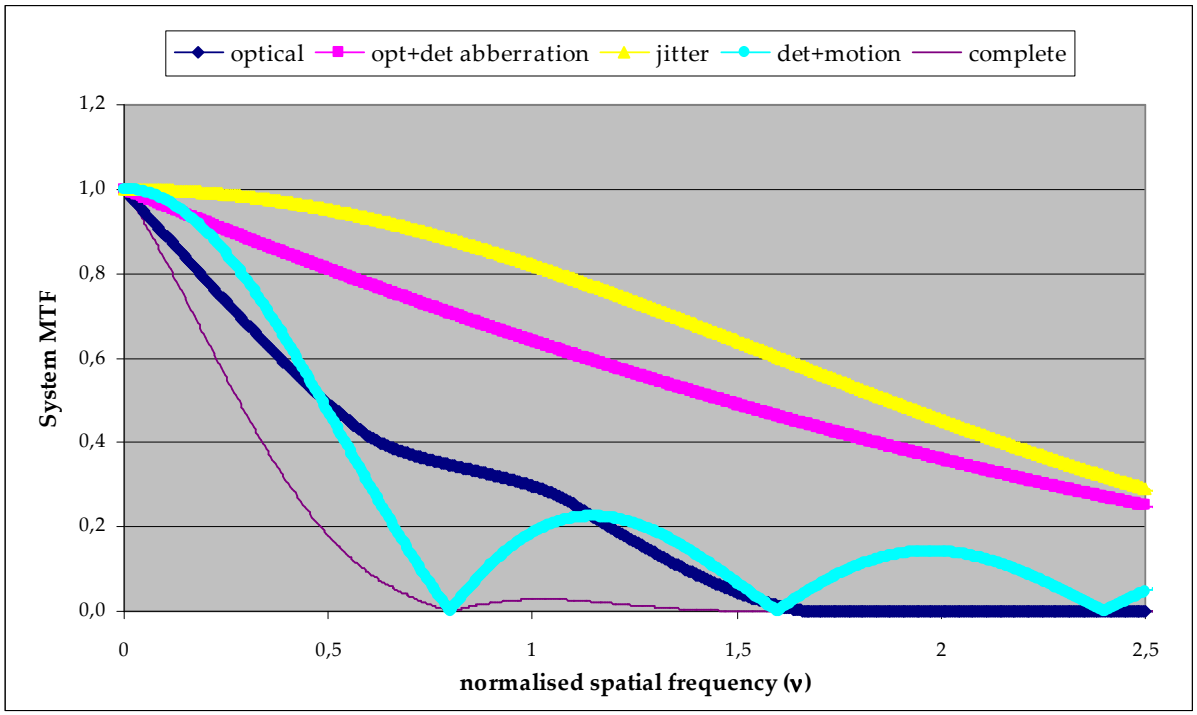

Figure 39: MTF-SYS components.

The most critical degradation components are the $MTF_{detector}$ and MTF_{motion} which reduce significantly the magnitude of MTF, especially at high spatial frequency. This effect has two opposite consequences:

1. negative effect: the reduction of MTF magnitude at high spatial frequencies determines that image short scale features suffer an higher degradation effect with a significant loss of contrast;
2. positive effect: MTF magnitude reduction could help in limiting aliasing effects, thanks to a greater attenuation factor over the image spatial frequency components that are greater than the detector Nyquist frequency.

3.2.3 The simulator

HRIC-SIM is developed in Interactive Data Language (IDL), which is a software development environment suitable to manipulate images. In addition, it offers the possibility to build a simple and efficient Graphics User Interface (GUI) that helps users inserting parameters and performing simulations in short time.

Figure 40 shows the HRIC-SIM flowchart.

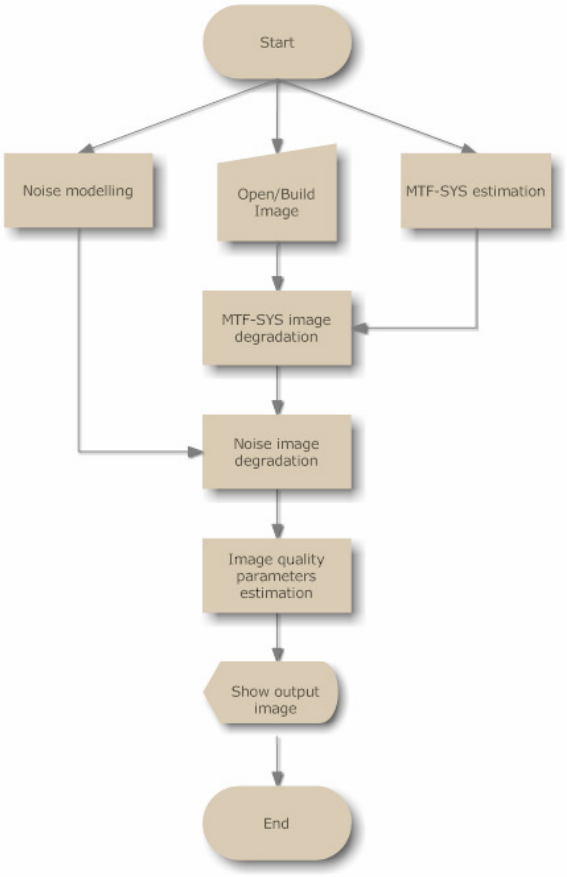

Figure 40: Simulation tool scheme.

In the following paragraphs all HRIC-SIM stages are described.

3.2.3.1 Input image

HRIC-SIM uses a GUI to input an already existing image or to build a synthetic scenario (e.g.: bars, edge, impulse, etc.). Such an image represents the observed scene in real operative conditions and so, from the spatial frequency content point of view, it is characterised by an arbitrary wide spatial spectrum which, in principle, could be incompatible with imaging system detection capabilities.

To guarantee this degree of freedom it is necessary to break the 1:1 correlation between the image and detector pixel size that occurs when opening or building an image and that upper limits its spatial spectrum to the detector Nyquist frequency. To this aim, a scaling factor is used, which "explodes" the input image spectrum shifting its components to higher spatial frequencies. As a result, each detector pixel "sees" a more detailed (a "super" resolved) image with shorter scale features (Figure 41) whose spatial frequency components are greater than the detector Nyquist frequency.

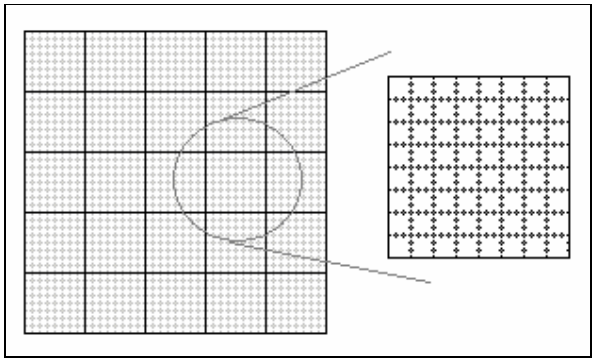

Figure 41: Comparison between detector pixel size (left) and input image pixel size (right).

3.2.3.2 System MTF estimation

The calculation of MTF-SYS (Equation 35) is a complicated task due to the "sinc" formulation of the $MTF_{detector}$ and MTF_{motion} components, which is a non-causal infinite function. As a result, MTF-SYS calculation is performed in two steps:

1. a partial MTF-SYS profile is calculated considering only MTF_{optic}, $MTF_{optical\_aberr}$, $MTF_{detector\_aberr}$ and MTF_{Jitter}:

$$MTF'_{system} = MTF_{optic} \cdot MTF_{optical\_aberr} \cdot MTF_{detector\_aberr} \cdot MTF_{jitter}$$

Equation 41: HRIC simulator partial system MTF profile.

   and applying a radial symmetry to derive the 2-D extension.

2. $MTF_{detector}$ and MTF_{motion} components are introduced by exploiting the convolution theorem:

$$f(x,y) * g(x,y) \leftrightarrow F(u,v) \cdot G(u,v)$$

Equation 42: Convolution Theorem.

   As a result, instead of reproducing the sinc function, its simple Fourier anti-transform (rectangle) is used by means of convolution with the partial MTF-SYS anti-transform.

   At this stage it is important to underline what is the dimension of the convolution box with respect to input image pixel size. Being $MTF_{detector}$ and MTF_{motion} components related to the detector, and considering the scaling factor introduced in the previous paragraph (Figure 41), their anti-transform dimensions are:

   - $MTF_{detector}$: square box with the scaling factor value as side;
   - MTF_{motion}: rectangular box with the scaling factor value as across-track side and Δp (Equation 37) as along-track side.

Once completed the MTS-SYS estimation, it is applied over the "super" resolved input image in order to simulate the optics-detector degradation. The resulting image is characterised by two principal effects:

1. blur: this effect is particularly evident when considering the shortest scale image features and it is due to the optical cut-off and Nyquist frequency limitations;
2. oversampling: thanks to the $MTF_{detector}$ component, the "super" resolved input image is mediate (box convolution) with the scaling factor as step.

As a final step, before introducing noise modelling, the degraded image is undersampled with the scaling factor as step in order to reduce image dimensions to the detector ones (Figure 41).

3.2.3.3 Noise

Next HRIC-SIM step consists into noise modelling and application. Such process recalls all the Radiometric Model equations (Section 3.1.1) and simulates the image degradation by substituting each pixel value with a random value extracted from a Gaussian distribution where:

- Mean value: pixel original value;
- Standard deviation: frame noise expression (Equation 26).

3.2.3.4 Degradation evaluation: Relative Edge Response (RER)

HRIC is an imaging system devoted to reveal image short scale features with high level of sharpness and global contrast. To guarantee such objectives the estimation of the Relative-Edge-Response (RER) parameter is of paramount importance.

RER ([49], [50], [51], [52]) is one of the engineering parameters of General Image Quality Equation (GIQE) which is used to provide predictions of imaging system performance with respect to the National Imagery Interpretability Rating Scale (NIIRS). It is directly related to the contrast response of an imaging system and represents its reactivity degree with respect to rapid signal fluctuations in the observed scene (Figure 42).

Figure 42: RER estimation test scenario. airborne (left) and on-ground (right) view of a typical pattern used to simulate edges for RER estimation.

RER analytical expression is:

$$RER = \sqrt{\left[ER_X(0.5) - ER_X(-0.5)\right] \cdot \left[ER_Y(0.5) - ER_Y(-0.5)\right]}$$

Equation 43: Relative Edge Response (RER) equation.

where ER is the Edge Response of the system. The RER parameter is derived considering the ER at an half of Ground Sample Distance (GSD – the distance between two adjacent pixel centres) from the real edge position in the image (Figure 43).

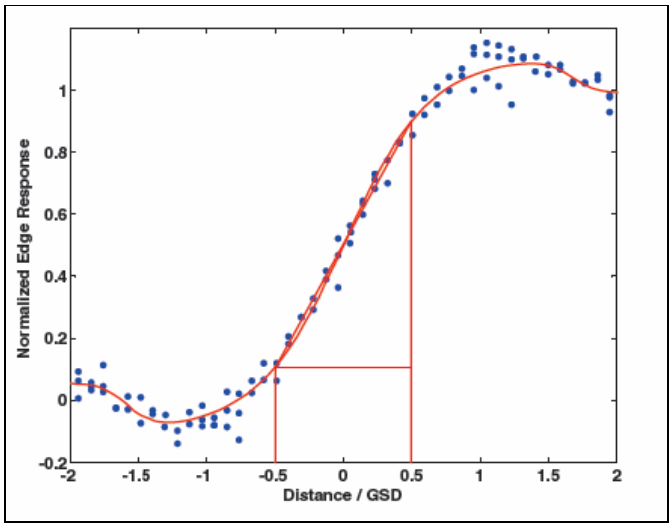

Figure 43: Normalised Edge Response profile at different edge-GSD distance.

Figure 43 shows that the ER profile (red line) is derived from the interpolation of several samples at different sub-pixel distances obtained as illustrated in (Figure 44).

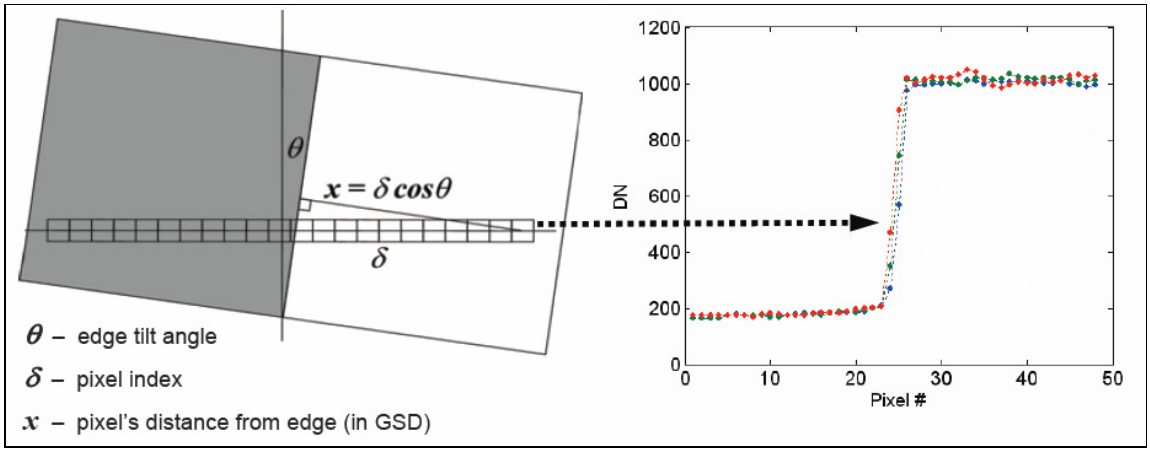

Figure 44: Edge Response measurement technique.

3.2.4 HRIC imaging performance analysis

HRIC-SIM has been used to test the HRIC imaging system performances on different input scenarios (Table 6) and considering the optical design parameters reported in Table 7.

Type	Sub-type	Remarks
Real	-	Mars surface acquisition
Synthetic	Impulse	Image signal intensity derives from Black Body irradiance estimation at central panchromatic filter wavelength (i.e. 650 nm) for different surface types (Dark, Smooth Plains, Highlands or Cratered Regions – 6%, 12%, 17% and 30% of reflectance, respectively).
	Across-track edge	
	Across-track multi-frequency bars	

Table 6: HRIC-SIM simulation images.

Parameter	Value	Remarks
Scaling factor	8	It represents the ratio between the image and the detector pixel size
Pupil diameter [mm]	90	-
Focal length [mm]	800	-
$k_{optical\text{-}aberr}$	10 [%]	-
$k_{detector\text{-}aberr}$	10 [%]	-
σ_{Jitter}	10^{-6}	-

Table 7: HRIC simulation tool input parameters.

Noise modelling parameters are reported in Table 5.

Finally, RSI-ENVI[2] (Research System Inc. – ENvironment for Visualizing Images) tool has been used to show, analyse and extract data and profiles from input and output images in order to evaluate and to report the HRIC imaging system design performances.

[2] Software solution for processing and analysing geospatial imagery with also GIS capabilities.

3.2.4.1 Real Image

Real image simulation has been done considering a Mars surface observation (Figure 45) performed by the High Resolution Imaging Science Experiment (HiRISE) instrument aboard the American mission Mars Reconnaissance Orbiter (MRO). In particular, the radiance data of the image in Figure 45 have been extracted from the public repository (available on http://hirise.lpl.arizona.edu) and, then, they have been adapted to the Mercury conditions in order to have a continuous signal distribution between albedo coefficients (6% ÷ 30% of reflectance) of Mercury dark and cratered regions.

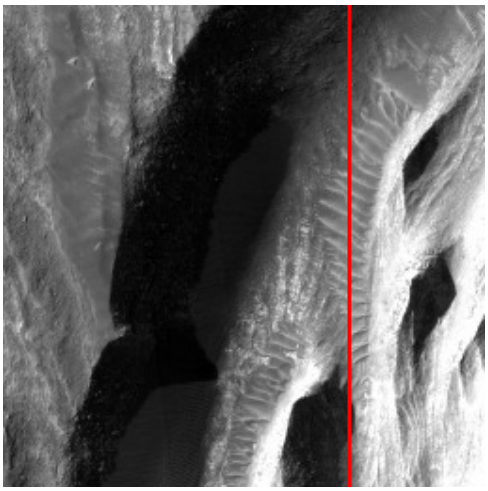

Figure 45: Juventae Chasma Landform (-3.6° N, 298.2° E) ENVI plot.

Such a scenario has been considered as a suitable testing sample for two reasons:

1. high contrast level;
2. presence of short scale structures similar to across-track bars (Figure 45 – red line).

Figure 46 reports the input, output and the difference images obtained with HRIC-SIM tool.

By analysing the difference image in Figure 46 it is possible to notice that edges appear particularly evident; such result derives mainly from the blurring effects produced during the detector exposure time (MTF_{motion} component of MTF-SYS). Another relevant degradation element is the noise component which seems uniformly distributed.

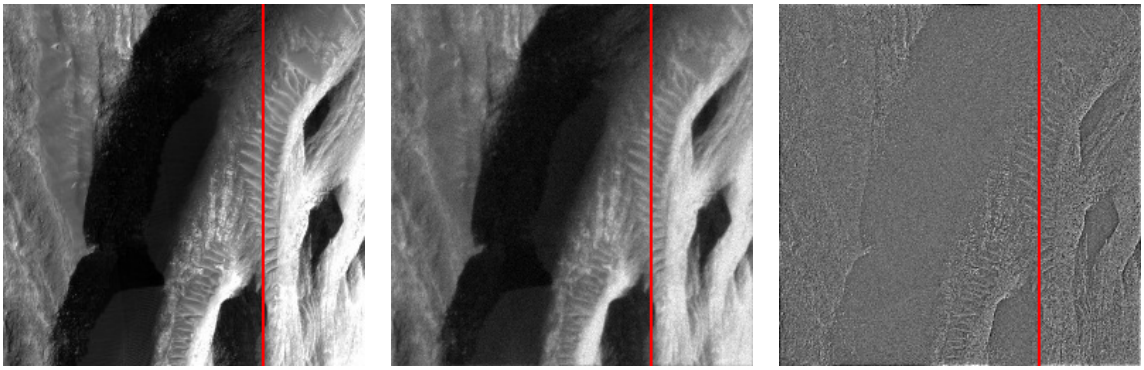

Figure 46: ENVI plot of input (left), output (middle) and difference (right) images.

Accordingly to MTF-SYS definition (see Section 3.2.2) the expected effects are:

1. modulation of output image signal fluctuations (i.e., attenuation);
2. spatial frequency components cut-off (MTF_{optic}) and aliasing ($MTF_{detector}$) effect which produce the loose of the shortest size superficial features;
3. along-track blurring during detector exposure (MTF_{motion}).

Figure 47 reports a vertical profile comparison between HRIC-SIM input and output images (red line in Figure 45) in which all the above expected effects can be identified.

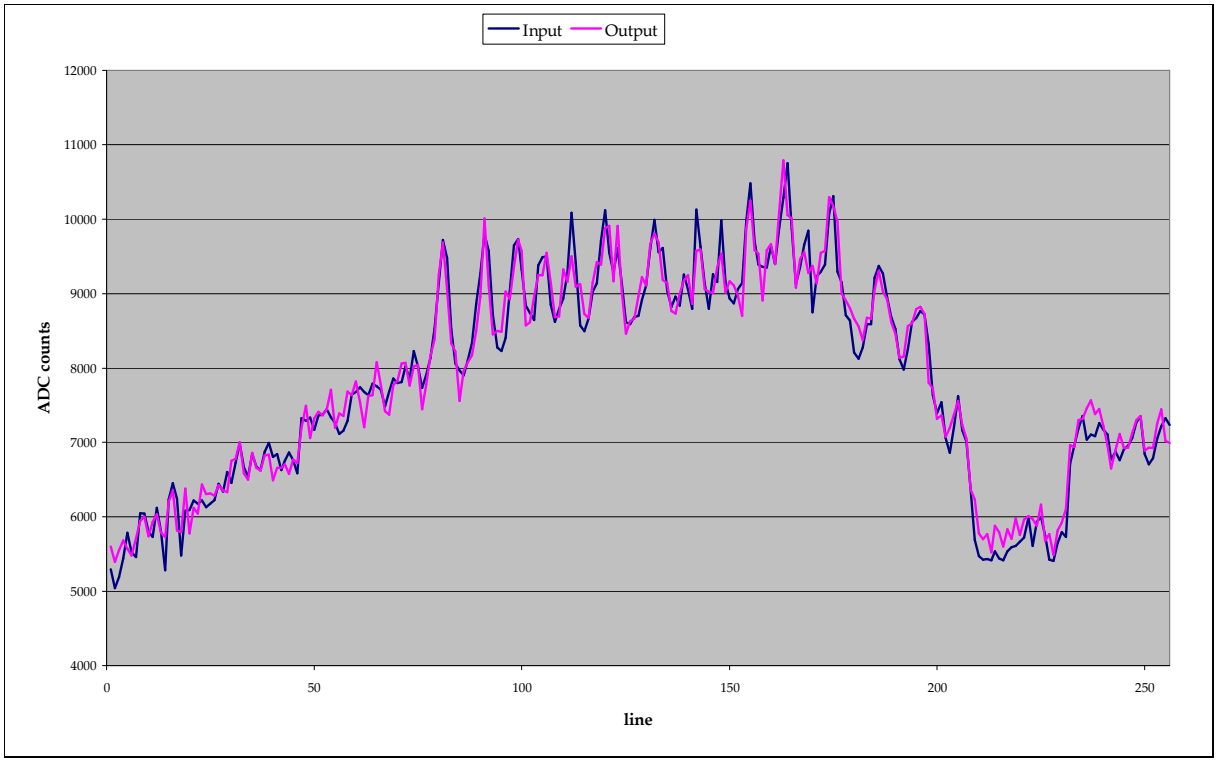

Figure 47: Vertical profile comparison.

3.2.4.2 Synthetic scenarios

3.2.4.2.1 Impulse

Figure 48 reports the HRIC-SIM simulation results when considering a point source. Such synthetic scenario provides the PSF calculation of the HRIC imaging system.

Considering Table 6 specifications, point source synthetic scenario has been derived considering:

- smooth plains radiance as background intensity;
- twice of smooth plains radiance as point source intensity.

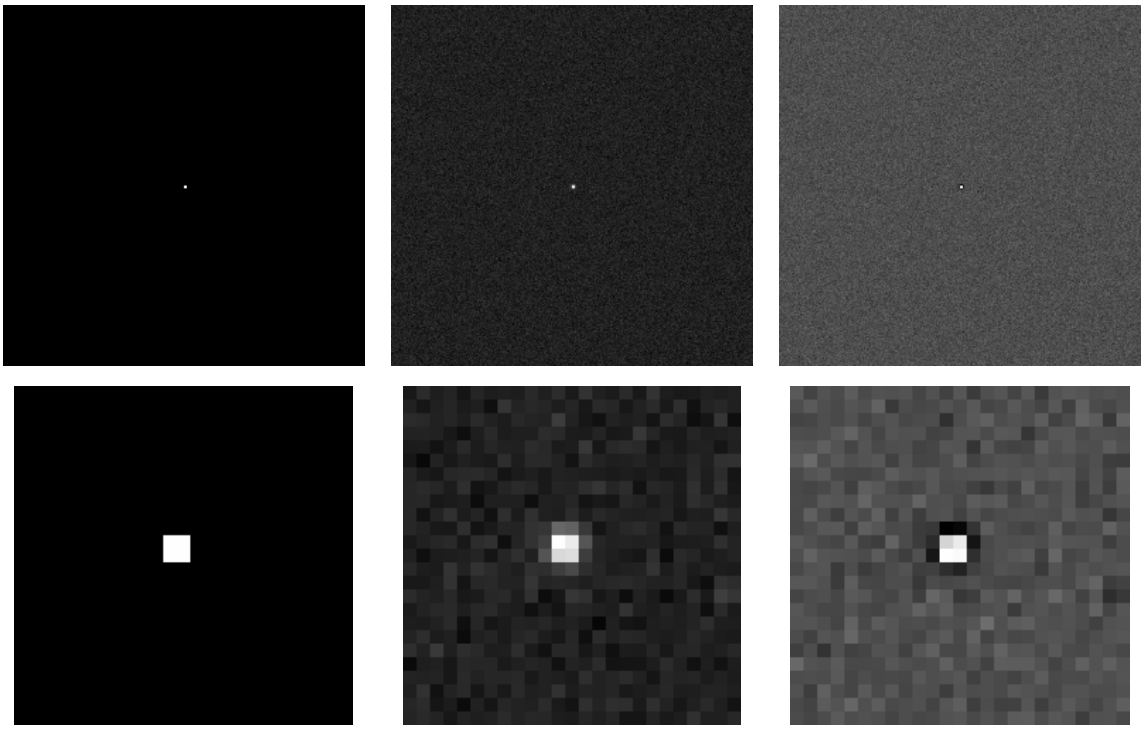

Image statistics					
Minimum:	6553	Minimum:	5913	Minimum:	-1348
Maximum:	13106	Maximum:	10809	Maximum:	3037
Mean:	6553.4	Mean:	6554.4	Mean:	-1.03
Standard deviation:	51.2	Standard deviation:	169.9	Standard deviation:	168.6

Figure 48: ENVI plots of input impulse (left), output PSF (middle) and difference image (right). Top: complete image; Middle: zoom; Bottom: statistics table.

Even though the input synthetic scenario considers a little difference in radiance level (12% vs. 24% of planetary surface albedo), thanks to HRIC detector performances and

exposure time maximisation (Figure 24 and Figure 25), the point source and PSF images appear sharp with a significant difference in signal level (Figure 48 – min - max statistics). From a quick look of the difference image (Figure 48 – right), two elements are evident:

1. noise contribution seems to be uniformly distributed;
2. residual point source derives from the difference in shape and intensity between input source and HRIC PSF.

The above elements become more relevant when considering the *Standard deviation* parameter in images statistics (Table in Figure 48): the output image presents a high intensity level variability (standard deviation), indicating that noise fluctuations and HRIC PSF enlargement are more relevant that what they visually appear.
In any case, the sharpness of the output image indicates that the impulse is well identified.
Figure 49 reports a vertical profile comparison between HRIC-SIM input and output images over the point source. Besides the noise contribution, the following major elements are evidenced on the output image:

1. lower PSF intensity: peak value attenuation is due to MTF-SYS modulation effect (Section 3.2.1);
2. larger PSF profile: shape enlargement is another typical MTF-SYS effect due to the cut-off frequency which eliminates higher spatial frequency components;
3. PSF rising side anticipates the input source one (lower line value) due to the along-track smear during exposure (MTF_{motion}).

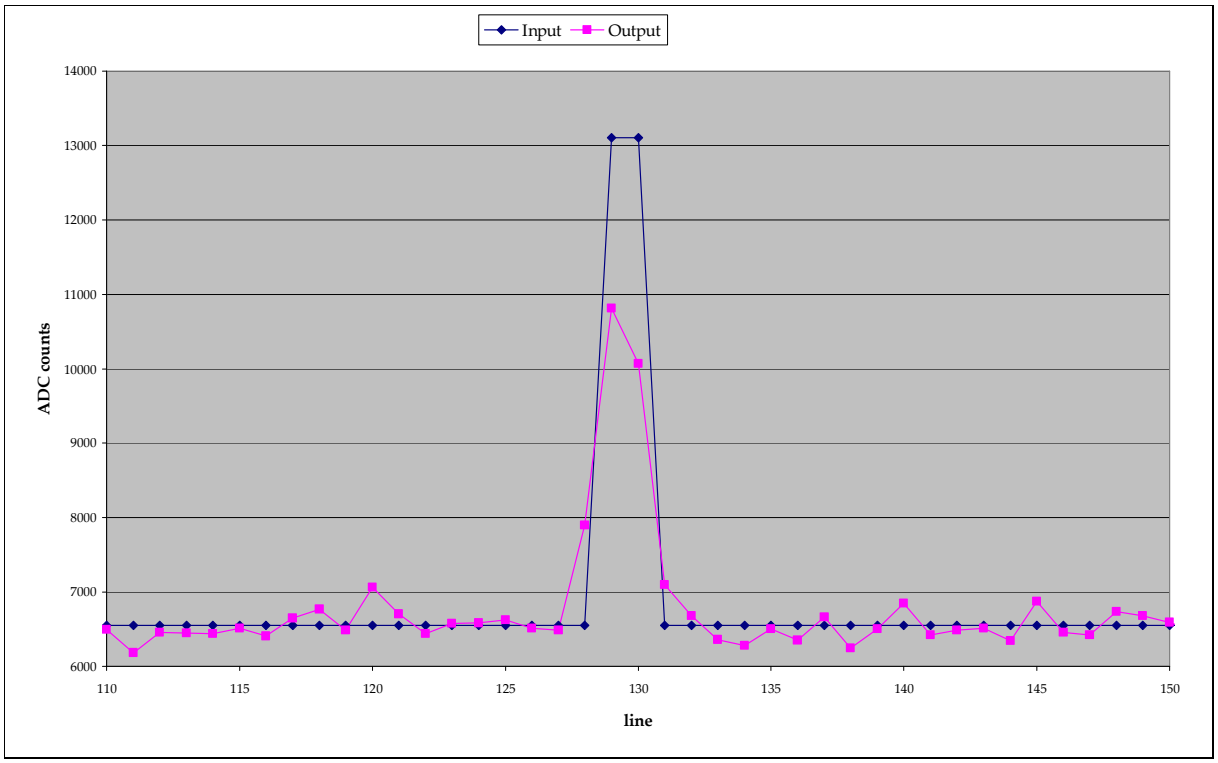

Figure 49: Impulse vertical profile comparison.

3.2.4.2.2 Edge

Figure 50 reports the HRIC-SIM simulation results when considering an along-track amplitude variable edge. Such synthetic data are useful in evaluating the impact of MTF_{motion} component in blurring edges.

From Table 6 specifications, edge has been derived considering:

- dark regions as background intensity;
- 0.5% across-track step intensity increase.

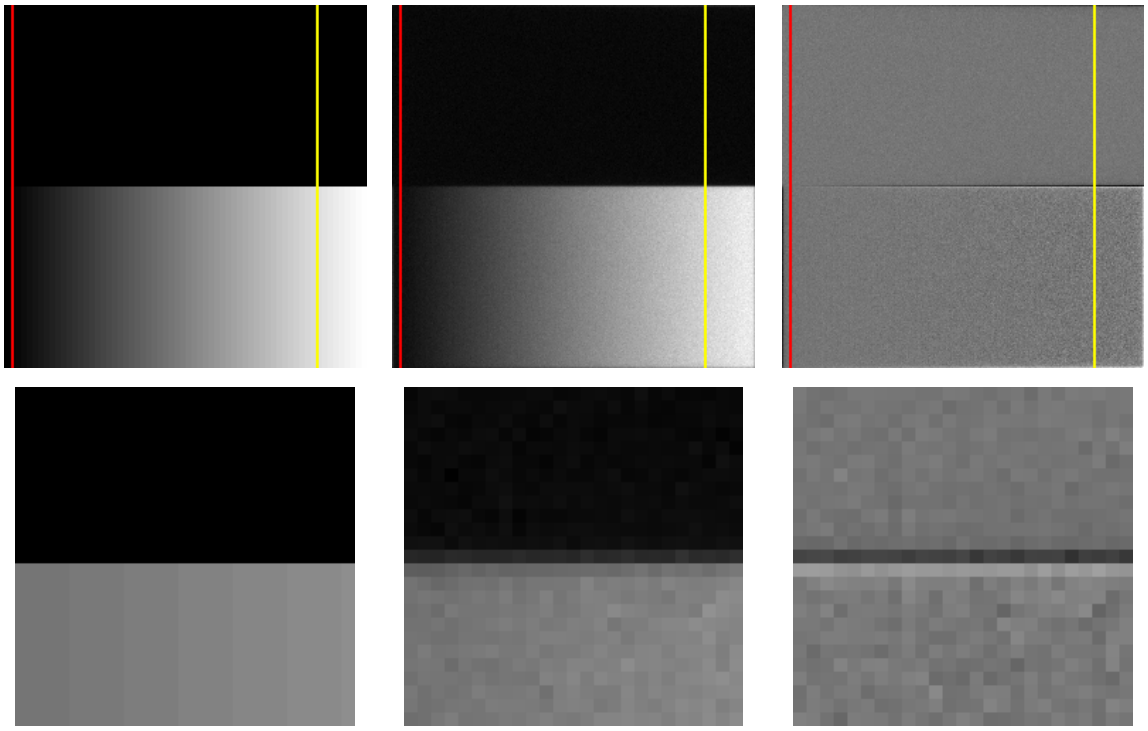

Image statistics					
Minimum:	2097	Minimum:	1653	Minimum:	-3359
Maximum:	13106	Maximum:	13773	Maximum:	3887
Mean:	4849.4	Mean:	4851.9	Mean:	-2.5
Standard deviation:	3575.8	Standard deviation:	3520.8	Standard deviation:	280.6

Figure 50: ENVI plots of input (left), output (middle) and difference image (right). Top: complete image; Middle: zoom; Bottom: statistics table.

By observing the difference image (Figure 50 – right) and considering image statistics, input and output images seem to be very similar. The only evident feature is the black horizontal line in the middle, which is related to the HRIC imaging system response to the

edge (see zooms). Such feature derives from the signal smearing during exposure: edge intensity signal is blurred in the along-track direction determining, in the worst case, a lose in feature localization. Figure 51 shows a comparison between input and output images for a quite critical vertical profile (Figure 50 – red line): noise fluctuations and signal along-track mixing mask the edge signal transition which becomes difficult to correctly localise.

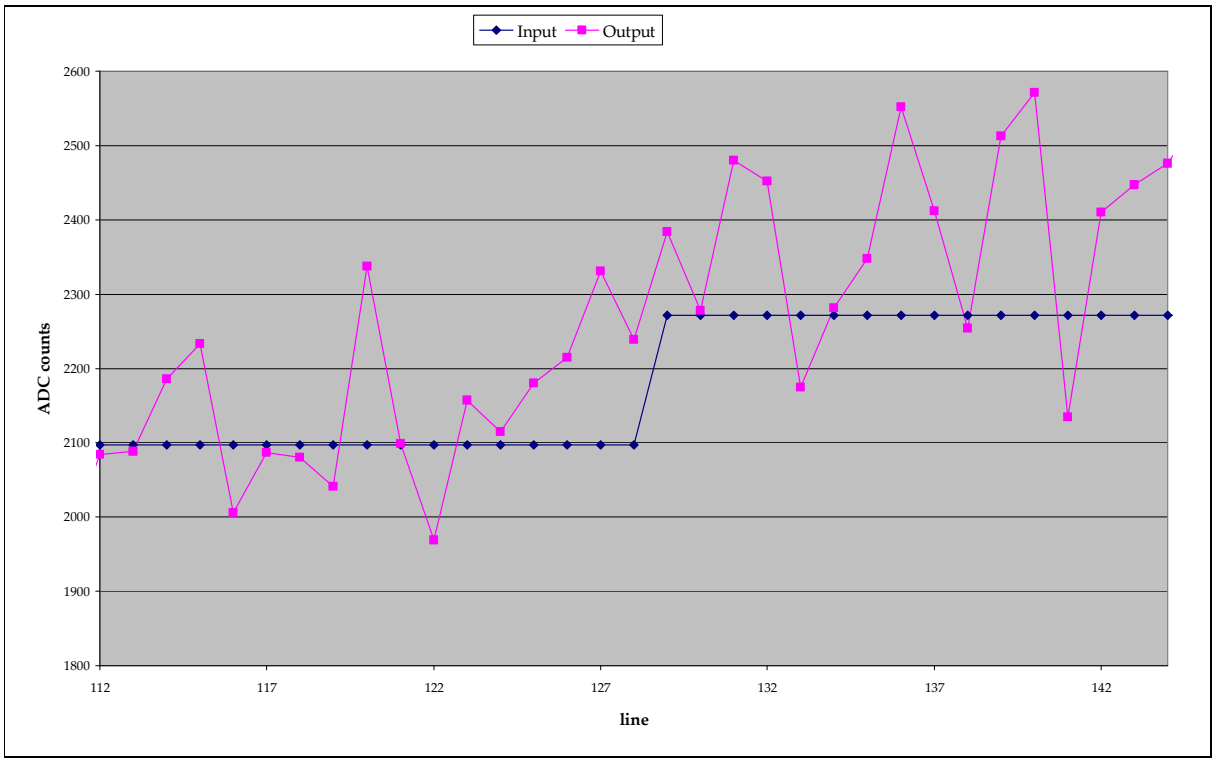

Figure 51: Critical edge vertical profile comparison.

Figure 52 shows the edge response comparison in a more favourable condition (Figure 50 – yellow line) in which the signal intensity transition is more evident.

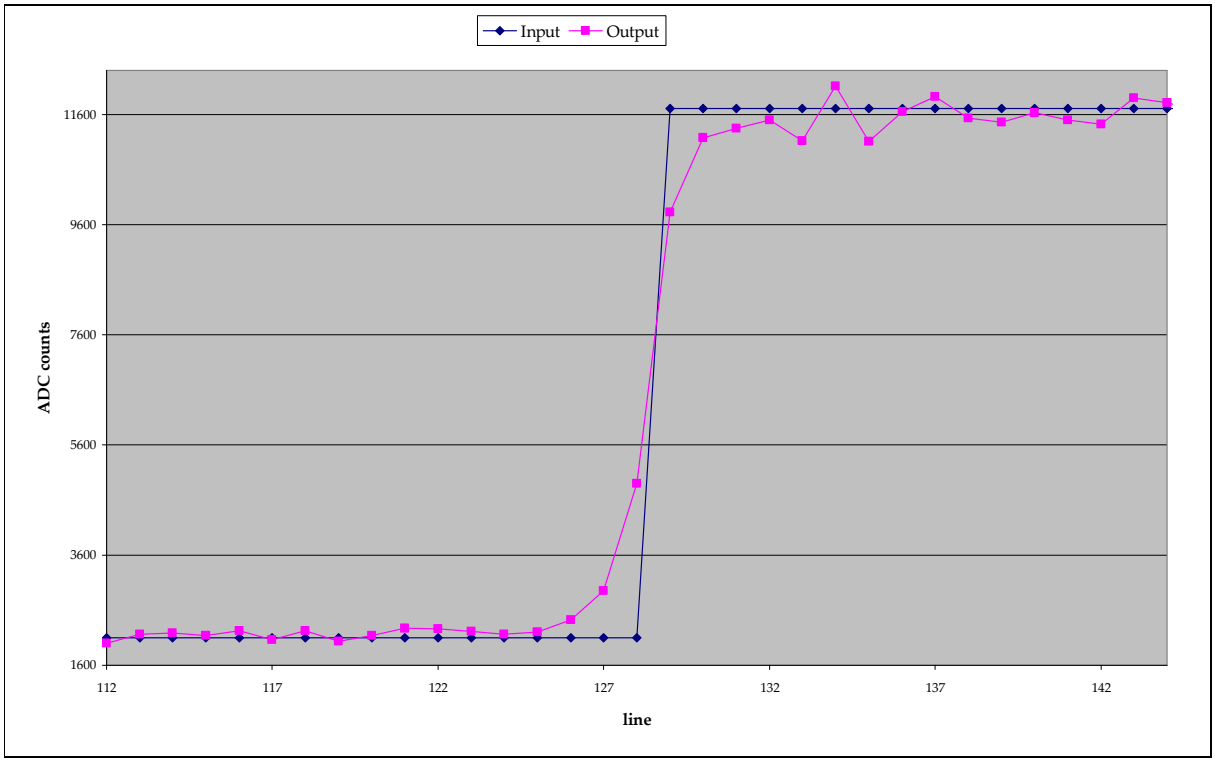

Figure 52: Favourable edge profile comparison.

3.2.4.2.3 Bars

The most interesting synthetic scenario used to evaluate HRIC system design performances is the multi-frequency and multi-shade horizontal bars image, because it allows to evaluate optical cut-off frequency, detector aliasing and edge blurring effects at the same time.

HRIC-SIM simulations have been done considering two possible scenarios:

- across-track shades;

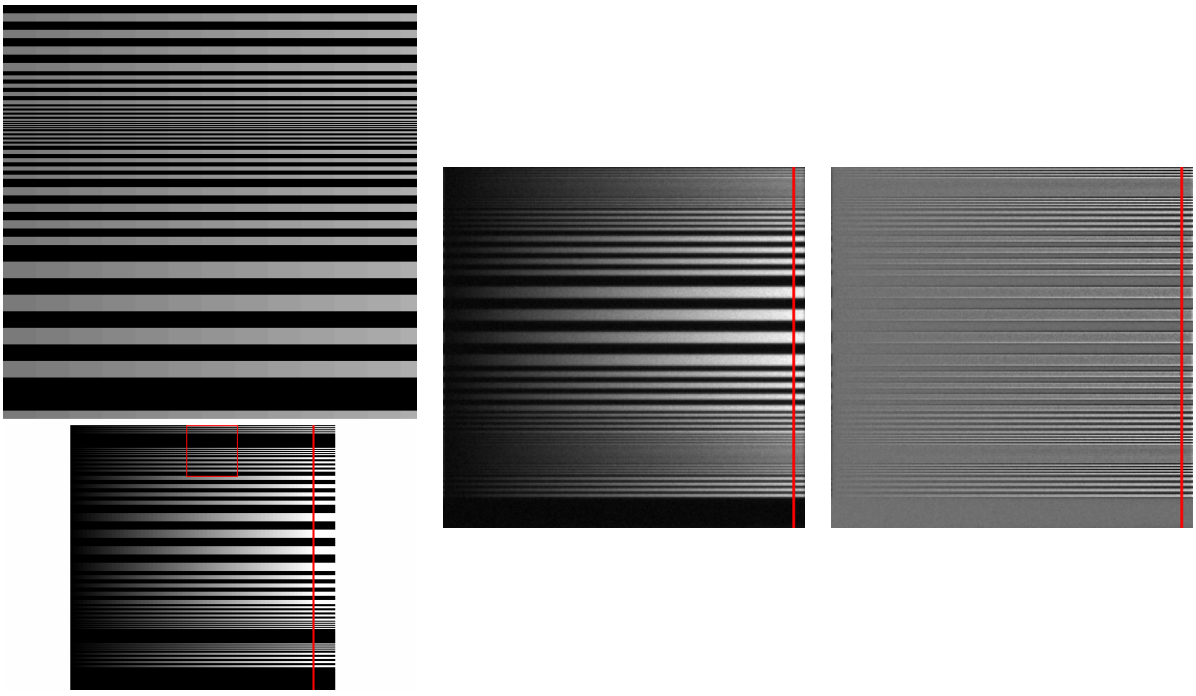

Image statistics					
Minimum:	2069	Minimum:	1681	Minimum:	-4654
Maximum:	13106	Maximum:	13274	Maximum:	5867
Mean:	4630.7	Mean:	4626.7	Mean:	4
Standard deviation:	3373.4	Standard deviation:	2571.5	Standard deviation:	1340.5

Figure 53: ENVI plots of input (left), output (middle) and difference image (right). A zoom (left-top) of the red box in the input image (left-bottom) is also reported. Bottom: statistics table.

From Table 6 specifications, multi-frequency across-track shade bars have been built considering:

- dark regions as background intensity;
- 0.5% across-track step intensity increase.

Figure 53 – left shows the input image in a complete (bottom) and a zoomed (top) version. This allows us to identify the thinnest horizontal bars, whose dimensions are incompatible with the detector sampling capabilities. In fact, the thinnest bars on the top are not resolved in the output image (Figure 53 – middle) due to:

- optical cut-off frequency;
- detector aliasing, which mixes signal fluctuations of larger bars.

Additional degradation effects are:

1. noise contribution, uniformly distributed over the image;
2. bar edges evidence (Figure 53 – right) which derives from image smearing during exposure.

Figure 54 shows a vertical profile comparison between the original and the output image (Figure 53 – red line); the loss of the thinnest bars (around samples 70-150) is clear, with dominance of noise and signal fluctuations mixing (aliasing) effects. Another evident effect is the anticipation of signal fluctuation rising side which is due to the edge blurring effect during exposure.

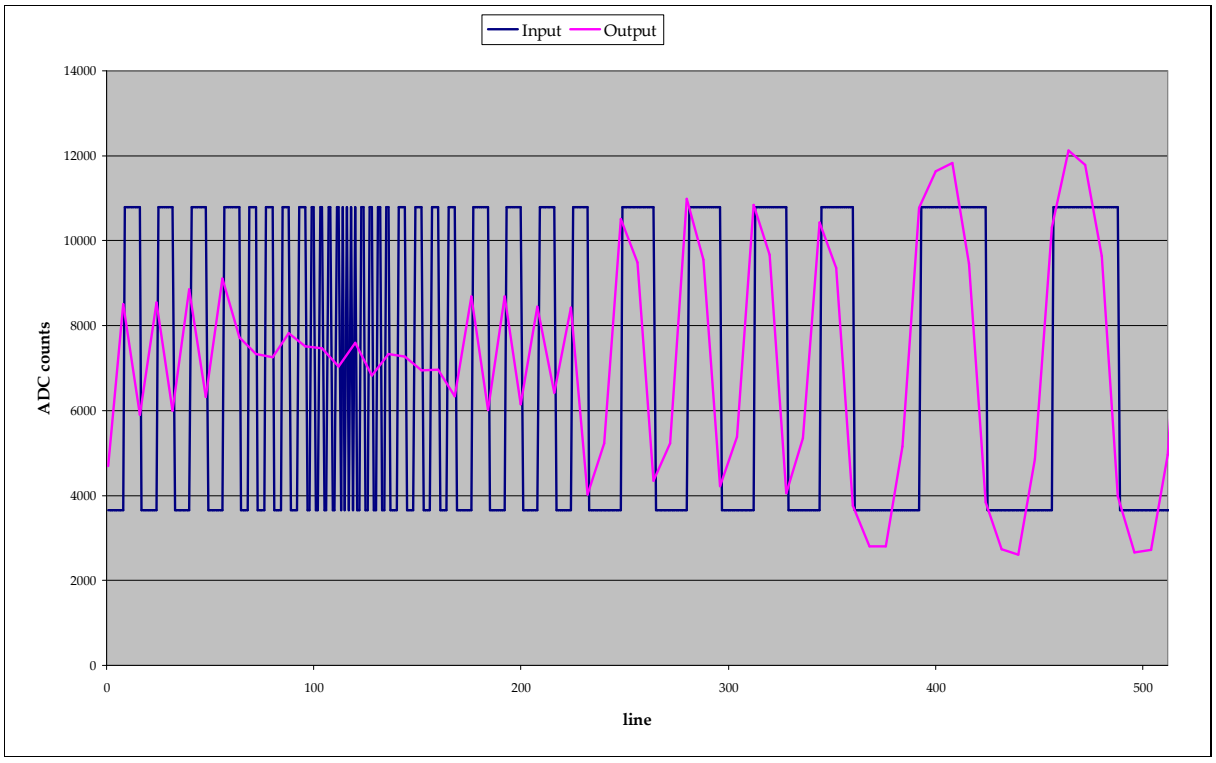

Figure 54: Horizontal multi-frequency bars with across-track shading vertical profile comparison.

- along-track shades;

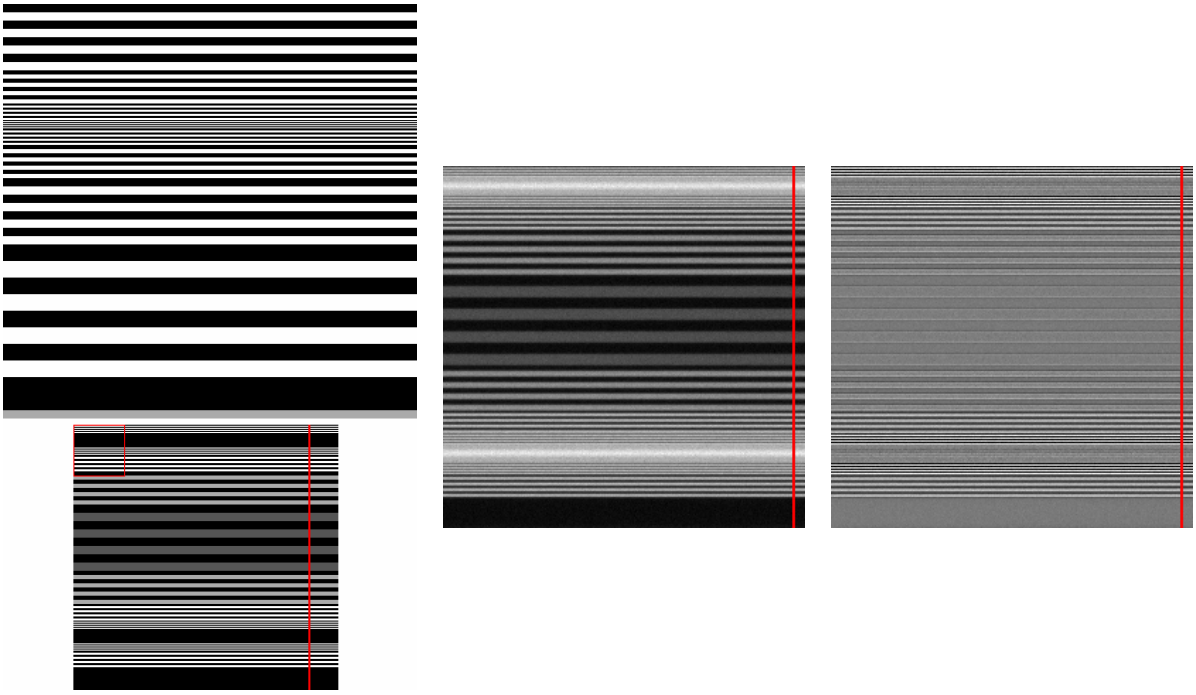

Image statistics					
Minimum:	2621	Minimum:	2203	Minimum:	-4687
Maximum:	13106	Maximum:	11989	Maximum:	4988
Mean:	5723.7	Mean:	5713	Mean:	10.6
Standard deviation:	3551.3	Standard deviation:	2451.7	Standard deviation:	1756.5

Figure 55: ENVI plot of input (left), output (middle) and difference image (right). A zoom (left-top) of the red box in the input image (left-bottom) is also reported. Bottom: statistics table.

In this case, multi-frequency across-track shade bars have been derived considering:

- dark regions as background intensity;
- as the horizontal bars reduce in dimension the related signal intensity doubles (equivalent albedo coefficients: [6%; 50%]).

As in Figure 53, also Figure 55 – left shows the complete (bottom) and zoomed (top) input image. In the output image (Figure 55 – middle) the thinnest bars on the top are no more resolvable due to:

- optical cut-off frequency;
- detector aliasing, which mixes signal fluctuations of larger bars.

Additional degradation effects are:

1. noise contribution, uniformly distributed over the image;
2. bar edges evidence (Figure 55 – right) which derives from image smearing during exposure.

Figure 56 reports a vertical profile comparison between input and output images; the most critical area is around the thinnest bars where optical cut-off and/or noise effects limit their resolvability. Another interesting feature regards the output signal fluctuations whose rising side always anticipates the input ones: it is a clear example of the smearing effect.

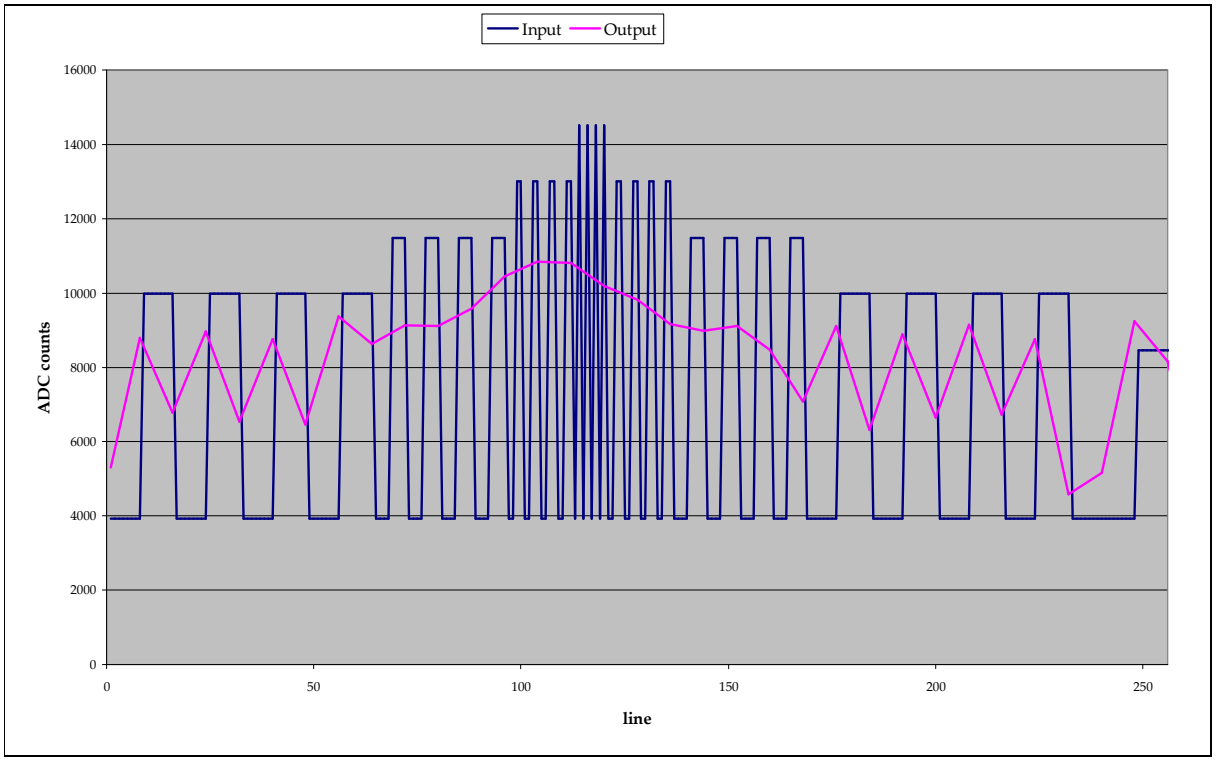

Figure 56: Multi-frequency bars with along-track shading vertical profile comparison.

3.2.4.3 Relative Edge Response (RER) simulation

To build a representative normalised Edge Response (ER) profile as shown in Figure 43 a large number of sub-pixel sampling has been used. Such process is sketched in Figure 57 where:

- the red box on the top-left represents one HRIC detector pixel. It is divided into 8x8 sub-pixel elements to evaluate ⅛ edge shift;
- the 12 rectangular grids represent a subset of the shifting edge images with (pink line) reference start position;
- the green and orange squares in each of the 12 rectangular grids represent the HRIC pixel detector;
- the red cross in the middle of green and orange squares in each of the 12 rectangular grids represents the reference position from which the edge distance is calculated;
- the grids at the two side serve as reference for edge shifting.

Figure 57: Sub-pixel edge shifting technique.

Using the shifting approach sketched in Figure 57, a set of 40 test images with horizontal multi-shade edge vertically shifted in the range [-2.5 ÷ 2.375] of a pixel size has been considered (Figure 58).

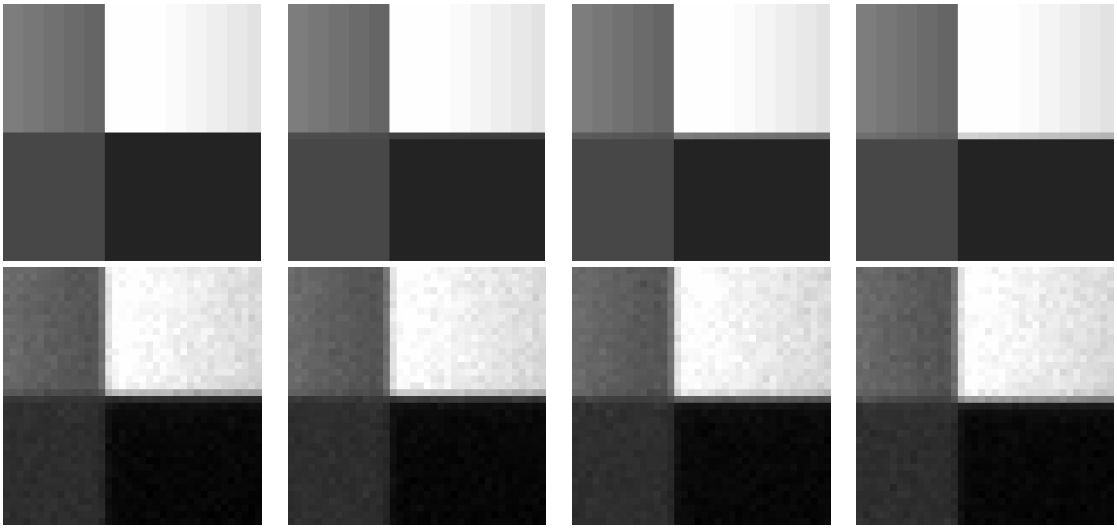

Figure 58: Subset of test input (top) and output (bottom) images.

Each image is divided in several areas with different step amplitudes in order to perform a statistical evaluation of along-track edge response in a single image. Finally, each signal level is repeated N=3 times in column in order to extract a statistics (i.e. mean value) of the system response with respect to the noise component fluctuation.

Starting from the output images, it is possible to build the normalised ER profile by extracting for a given pixel its signal level for the images sequence. Figure 59 show three normalised ER profiles.

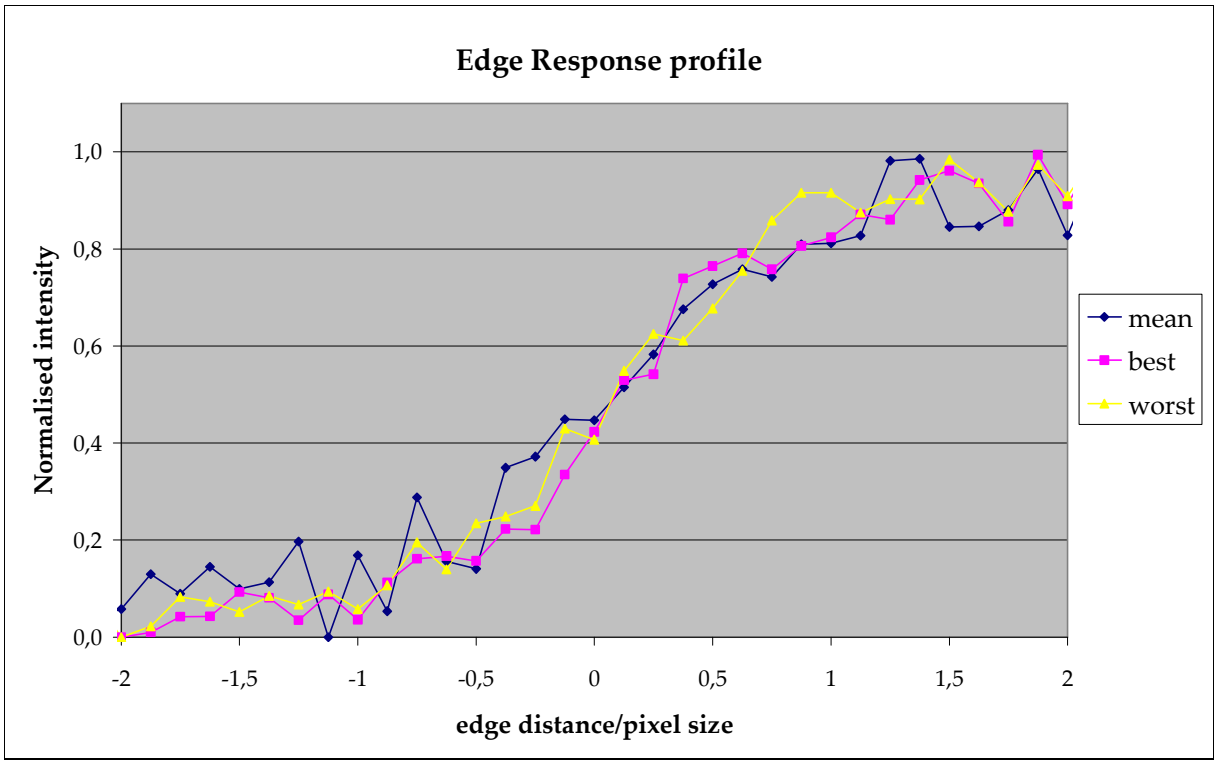

Figure 59: Normalised Edge Response profiles.

Table 8 reports a numerical comparison of these three cases.

Profile	Norm. ER @-0.5 / Norm ER @+0.5	RER
1 (Figure 59 – blue)	0.14 / 0.727	0.587
2 (Figure 59 – pink)	0.157 / 0.765	0.608
3 (Figure 59 – yellow)	0.235 / 0.677	0.443

Table 8: Comparison of three representative cases of Normalised Edge Response profile.

Figure 60 reports the complete RER profile calculated on all the tested edges: the blue line reports the RER values with respect to the edge of each column while the pink line represents a mean value calculated considering the N=3 repetitions of each signal level.

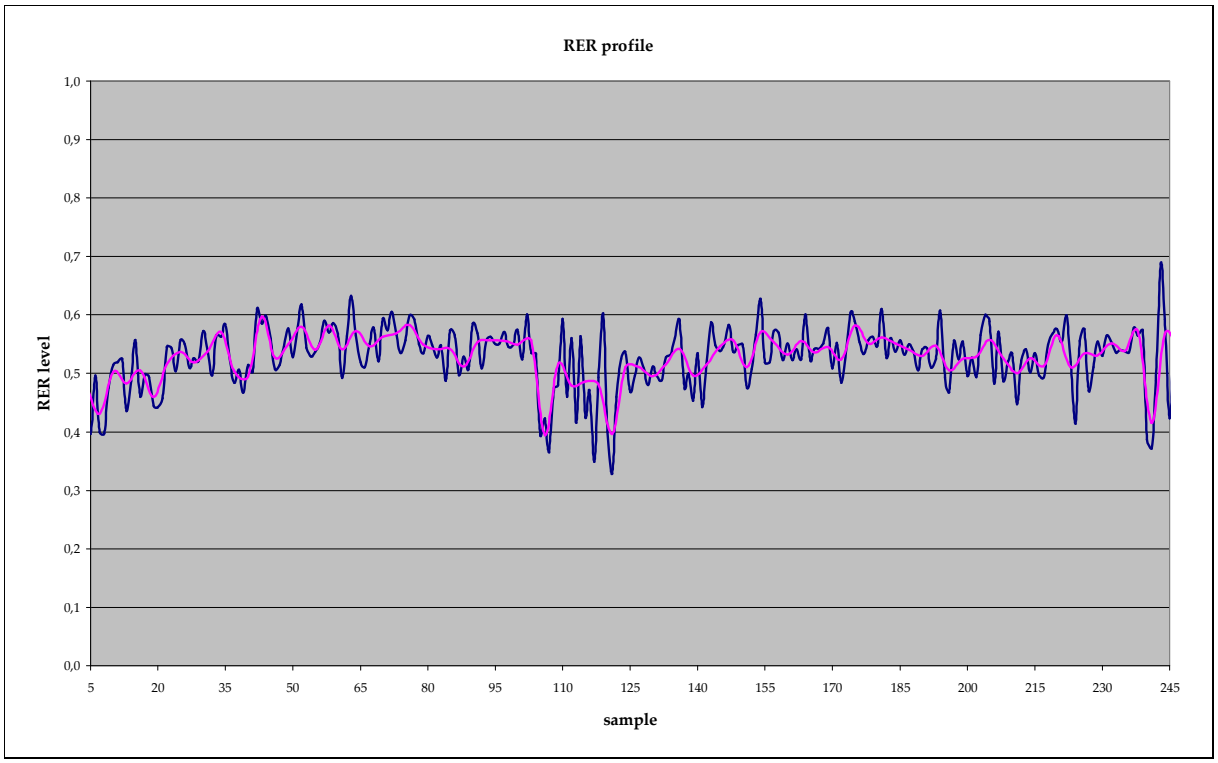

Figure 60: Relative Edge Response profile with respect to different edge intensity levels.

Figure 60 result indicates that HRIC imaging system design is characterised by a RER performance that is generally larger than 50%. Table 9 reports the RER performances of two of the most known high spatial resolution imaging systems operating around the Earth.

Sensor	Spatial resolution [m/pxl]	Altitude [km]	RER [%]
Quickbird	0.61 (Panchromatic)	450	75 [52]
IKONOS	0.82 (Panchromatic)	681	79 [51] [53]

Table 9: RER performances of the major high resolution imaging systems.

Instruments listed in Table 9 are imaging systems optimised for the Earth surface observation and are characterised by very high imaging performances. Anyway, the comparison between measured performances and the simulated values reported in Figure 60 indicates that the HRIC imaging system has quite good behaviour, also considering the hostile operative environment and the very strict mass and power budget limitations.

3.3 *Analyses of HRIC key optical elements*

The HRIC optical design is discussed in Section 2.2.2. In this section, the trade-off analysis performed on the mechanical/optical characteristics of some key optical elements, potentially affecting the image quality is reported. In particular:

- Filters: HRIC is equipped with a panchromatic and three broad-band filters (see Section 2.2.2). Their optical performances are extremely important to determine the amount of input radiance integrated on the associated detector area and, above all, the ratio between in-band and out-of-band components. Filters optical performance are in general estimated by means of ghost analysis and out-of-band vs. in-band total integrated radiance measurement;
- External baffle: it is the first element of HRIC optical-mechanical design (see Section 2.2.2). HRIC external baffle design is based on the Stavroudis concept, which is optimised for thermal rejection properties. External baffle optical performances are estimated by means of ray-tracing analysis, which can reveal undesirable in-filed light reflections.

3.3.1 **HRIC filters**

The optical properties (e.g., transmission, reflection and absorption) of the filters determine how light reaching the HRIC detector is spectrally selected in the different bands. Filters in the HRIC design are integrated in the detector package (see Section 2.2.2). Dimensioning specifications and requirements on sensor packaging determine their structure and manufacturing process:

- each filter is obtained starting from a fused-silica wafer;
- coatings are deposited on both sides of the wafer, with spectrally different (blocking and narrowband) optical properties, whose combined spectral properties define the HRIC filter;
- HRIC filters are obtained slicing the coated wafer;
- wafer slices are glued to each other with a transparent non-diffusive glue;
- a metallic bar is placed between adjacent filter slices in the glue in order to avoid light cross-talk;
- a Dark Mirror Coating (DCM) mask is applied on both surfaces of the glued filters block in order to cover filters and metallic bar edges and avoiding light scattering.

3.3.1.1 Filters optical specifications and optical performance analysis

HRIC imaging system design is characterised by four filters whose spectral specifications are reported in Table 10.

Filter	λ-50$_{on}$ [nm]	λ_C [nm]	FWHM [nm]	λ-50$_{off}$ [nm]	T_{out} / T_{in} [%]	T_{peak} [%]	$T_{out\text{-}ave}$ [%]
FPAN	400	650 ± 8	500 ± 5	900	< 0.5	> 85	< 0.05
F550	530	550 ± 9	40 ± 2	570	< 1	> 80	< 0.05
F750	730	750 ± 11	40 ± 2	770	< 1	> 80	< 0.05
F880	860	880 ± 13	40 ± 2	900	< 1	> 80	< 0.05

Table 10: HRIC filters optical specifications.

Such specifications allow the implementation of the scientific requirements, taking into account HRIC optical design requirements and filter manufacturing constraints.

Filters optical performances analysis has been performed in two steps:

- comparative: a preliminary analysis has been done in order to evaluate the out-of-band versus in-band optical transmission properties;
- absolute: using the HRIC-RM (see Section 3.1) the input signal reduction and the SNR variation with respect to an ideal (100% transmission) filter optical behaviour has been evaluated. Table 11 summarises the obtained results considering a possible acquisition over the Mercury equator on the periside arc with 12% (Smooth Plains) of albedo coefficient.

Filter	Total input energy [e^-]	Total filtered energy [e^-]	E_{tot} reduction [%]	In-band signal [%]	Out-of-band signal [%]	Out-band / In-band
FPAN	$1.2 \cdot 10^{18}$	$1.17 \cdot 10^{18}$	1.8	99.99	0.01	0.006
F550	$9.9 \cdot 10^{16}$	$9.7 \cdot 10^{16}$	1.55	99.82	0.18	0.18
F750	$1.16 \cdot 10^{17}$	$1.12 \cdot 10^{17}$	2.9	99.87	0.13	0.13
F880	$8.7 \cdot 10^{16}$	$8.5 \cdot 10^{16}$	2.4	99.9	0.1	0.1

Table 11: Filters optical performances with respect to entering energy.

Both analyses indicate that HRIC filters are characterised by very high optical performances; in particular, Table 11 indicates that:

- out-of-band signal contributes with a very low percentage, so that each HRIC filter operates the desired spectral selection on the integrated radiance;
- in-band total energy is close to the maximum achievable (ideal filter with 100% in-band transmission) values implying a good SNR.

3.3.1.2 Filter ghosts: definition and analysis

Ghosts are a relevant degradation effect in an imaging system due to the optical properties and configuration of its components. They consist of spurious signals originated by filter-detector reflections that overlap real signal with different intensity, size, shape and direction.

The most common ghost types are:

1. Internal ghosts: they are produced by the internal reflections between top and bottom filter faces (Figure 61).

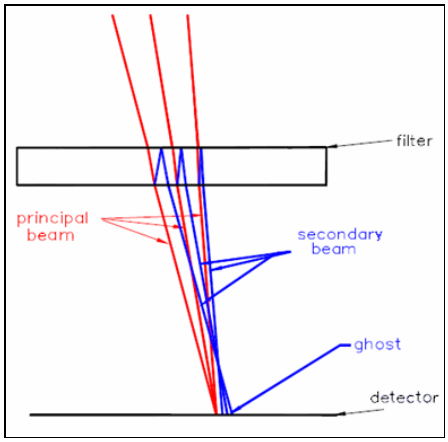

Figure 61: Internal ghost sketch.

Internal ghosts are the most critical ones, due to their high energy density which derives from the small attenuation (only two reflections) and the reduced area extension.

2. Narcissus ghosts: they are produced by reflections from the detector surface, which redirects a light portion towards the filters. This light contribution experiments direct and internal filter reflections determining the production of two different types of secondary ghosts (Figure 62):
    a. Primary Narcissus ghosts;
    b. Secondary Narcissus ghosts.

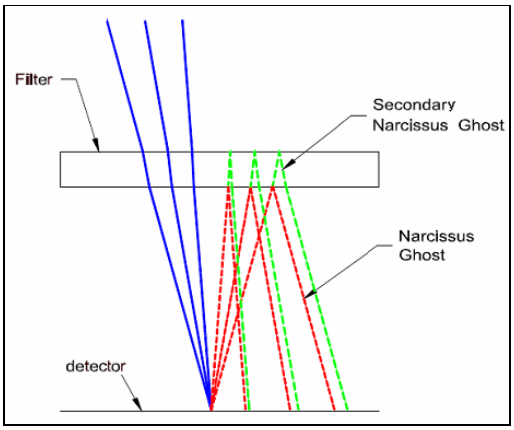

Figure 62: Narcissus ghosts sketch.

Secondary Narcissus ghosts are more critical with respect to the primary one: even though they have a lower energy density (one more reflection), secondary Narcissus ghosts are spread on a larger surface affecting a greater number of detector pixels.

Considering the HRIC filter strip manufacturing process (see Section 3.3.1), HRIC ghost analysis is important to determine the best optical configuration with respect to coating positioning (blocking filter; narrowband filter) on the two faces of the filter.

The HRIC ghost analysis has been performed by means of ZEMAX ray tracing tool in order to determine the diffraction limited spots (Airy disk) vs. ghosts dimensions and the energy density ratio with respect to the two possible filter coating configurations reported in Table 12.

Side	Case 1	Case 2
Space	Narrowband filter	Blocking filter
Detector	Blocking filter	Narrowband filter

Table 12: Filter coatings configurations.

Analyses have been done considering optical specifications in Table 10 and the following filter position specifications:

Parameter	Value
Filter thickness [mm]	1 ± 0.03
Detector-Filter distance [mm]	1.343 ± 0.356
Filter material	Fused-silica

Table 13: Filter design parameters.

Table 14 reports the HRIC ghost analysis results; in bold (case 1) the selected optical configuration:

Ghost	Filter	Ghost / spot area	Ghost / spot intensity
Internal	FPAN	60	$1.52 \cdot 10^{-6}$
	F550	26	$1.1 \cdot 10^{-5}$
	F750	39	$2.05 \cdot 10^{-5}$
	F880	74	$2.05 \cdot 10^{-6}$
Primary Narcissus	FPAN	229	**$5.5 \cdot 10^{-7}$ (case 1)**; $1.8 \cdot 10^{-6}$ (case 2)
	F550	286	**$3.2 \cdot 10^{-7}$ (case 1)**; $6.6 \cdot 10^{-6}$ (case 2)
	F750	149	**$4.7 \cdot 10^{-7}$ (case 1)**; $6.8 \cdot 10^{-6}$ (case 2)
	F880	96	**$1.25 \cdot 10^{-6}$ (case 1)**; $2.26 \cdot 10^{-5}$ (case 2)
Secondary Narcissus	FPAN	525	**$7.6 \cdot 10^{-7}$ (case 1)**; $2.3 \cdot 10^{-7}$ (case 2)
	F550	647	**$2.9 \cdot 10^{-6}$ (case 1)**; $1.3 \cdot 10^{-7}$ (case 2)
	F750	339	**$2.9 \cdot 10^{-6}$ (case 1)**; $1.6 \cdot 10^{-7}$ (case 2)
	F880	218	**$9.8 \cdot 10^{-6}$ (case 1)**; $4.8 \cdot 10^{-7}$ (case 2)

Table 14: HRIC ghost analysis results.

Table 14 reveals a conflicting results: **case 1** is the best solution to minimize the Primary Narcissus ghost density energy; on the contrary, Secondary Narcissus ghost minimization requires the choice of **case 2**. Anyway, considering the ghost vs. spot dimension ratio, **case 1** is the preferred solution, since the area ratio for Narcissus Ghost is half that of the Secondary Narcissus Ghost. So, considering both ghost dimensions and energy density minimisation, for all filters **case 1** is the preferred solution.

3.3.2 HRIC external baffle

The HRIC external baffle design (see Section 2.2.2) is based on the Stavroudis concept. The profile derives from the intersections of ellipsoids and hyperboloids increasing in size that share the two focuses (Figure 63).

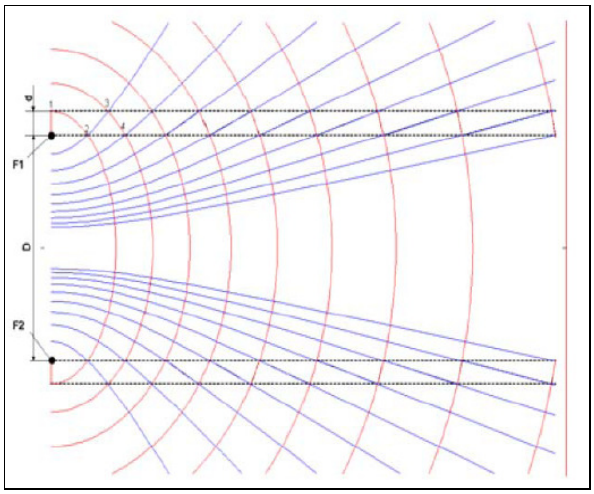

Figure 63: Stavroudis profile concept. F1 and F2 are the ellipsoid and hyperboloid focus positions. Point 1 is the starting position of the first ellipsoid; point 2 is the intersection between the first ellipsoid and the first hyperboloid; point 3 is the intersection between the first hyperboloid and the second ellipsoid, and so on.

Stavroudis near in-field intersections between the ellipsoids and hyperboloids (points 2, 4 etc. of Figure 63) may become secondary annular straylight sources directly visible by the detector. Therefore, a cylindrical and a conical configurations have been studied to analyse energy input due to annular sources reaching the HRIC detector. The two Stavroudis layouts are reported in Figure 64.

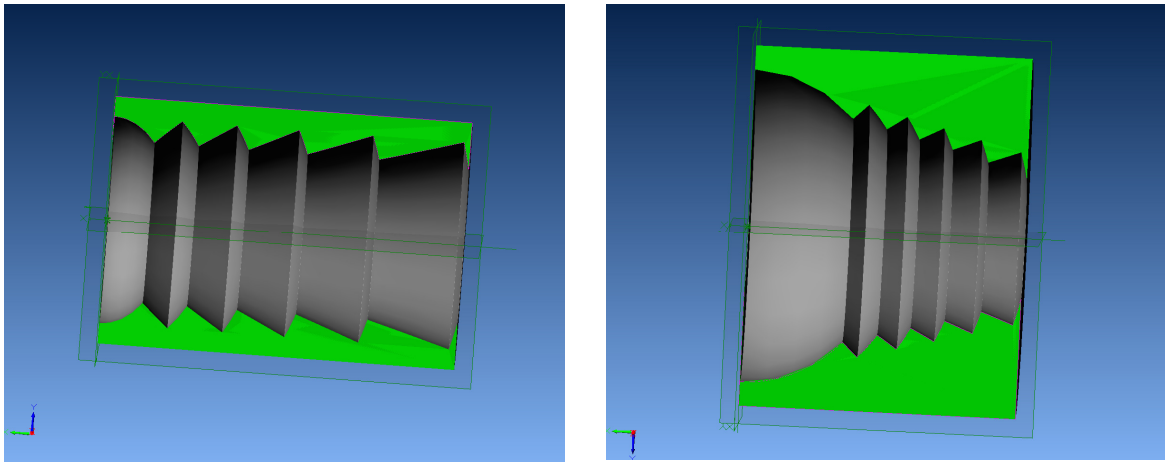

Figure 64: Cylindrical (left) and Conical (right) Stavroudis layouts (images are at different scale; the two baffle are equal in length but the aperture of the conical one is almost double wrt. the cylindrical one).

3.3.2.1 HRIC external baffle optical response

A comparative ray-tracing analysis has been performed for the two Stavroudis layouts starting from the following assumptions:

- Stavroudis internal surfaces are perfectly mirror-like (100% reflective);
- each Stavroudis intersection between the ellipsoid and hyperboloid surfaces (annulus) is modelled by a link with radius 0.1 mm;
- the internal cap surface (in front of the Stavroudis entrance) is perfectly absorbing.

It is important to underline that assuming a reflection of 100% for the Stavroudis internal surfaces represents a worst case in terms of light attenuation for two reasons:

1. each reflected ray maintains its original energy (no losses due to absorptions);
2. such a "lossless approach" allows several out-of-field rays to exit the Stavroudis baffle, by means of unlimited number of reflections, so contributing as "secondary" straylight.

The ray tracing analyses have been performed considering differently oriented elliptical collimated beams with increasing number of rays (from 10^5 to 10^6) in order to carry on a Straylight sensitivity analysis. Each beam is sized to the Stavroudis entrance shape visible from 5 different entering angles (2.5, 5, 10, 20, 40, degrees) in order to maximize incoming power flux.

Table 15 reports the simulation outputs of ray-tracing analyses performed with OptiCAD.

Cylindrical							**Conical**					
Incidence angle: 0 deg; Beam dimensions: 53x53 mm												
In rays	Density [ray/mm²]	Direct out rays	Refl out rays	Out/In [%]	Out_ref/In [%]		In rays	Density [ray/mm²]	Direct out rays	Refl out rays	Out/In [%]	Out_ref/In [%]
30308	3.5	28321	68	93.44	0.22		30308	3.5	28304	50	93.39	0.16
36733	4.3	34268	92	93.29	0.25		36736	4.3	34269	93	93.28	0.25
43729	5	40858	115	93.43	0.26		43732	5	40854	111	93.42	0.25
51376	6	47935	91	93.30	0.18		51376	6	47919	75	93.27	0.15
59612	7	55672	158	93.39	0.27		59612	7	55626	113	93.31	0.19
68444	8	63916	193	93.38	0.28		68456	8	63917	190	93.37	0.28
Incidence angle: 2.5 deg; Beam dimensions: 53x53 mm												
In rays	Density [ray/mm²]	Direct out rays	Refl out rays	Out/In [%]	Out_ref/In [%]		In rays	Density [ray/mm²]	Direct out rays	Refl out rays	Out/In [%]	Out_ref/In [%]
30284	3.5	25700	156	84.86	0.52		30284	3.5	25578	32	84.46	0.11
36686	4.3	31118	214	84.82	0.58		36684	4.3	30966	50	84.41	0.14
43704	5	37061	223	84.80	0.51		43706	5	36900	54	84.43	0.12
51336	6	43523	295	84.78	0.57		51336	6	43332	86	84.41	0.17
59552	7	50501	307	84.80	0.52		59550	7	50276	68	84.43	0.11
68386	8	58019	409	84.84	0.60		68386	8	57751	113	84.45	0.17
3056531	356	2593225	17020	84.84	0.56		3056542	356	2581058	3984	84.44	0.13
Incidence angle: 5 deg; Beam dimensions: 53x53 mm												
In rays	Density [ray/mm²]	Direct out rays	Refl out rays	Out/In [%]	Out_ref/In [%]		In rays	Density [ray/mm²]	Direct out rays	Refl out rays	Out/In [%]	Out_ref/In [%]
30205	3.5	22056	168	73.02	0.56		30206	3.5	21953	53	72.68	0.18
36590	4.3	26693	205	72.95	0.56		36590	4.3	26574	60	72.63	0.16
43572	5	31795	243	72.97	0.56		43572	5	31659	85	72.66	0.20
51174	6	37345	299	72.98	0.58		51174	6	37179	95	72.65	0.19
59386	7	43304	308	72.92	0.52		59386	7	43144	114	72.65	0.19
68206	8	49769	373	72.97	0.55		68206	8	49540	112	72.63	0.16
3047790	355	2223999	16824	72.97	0.55		3047802	356	2214394	5490	72.66	0.18
Incidence angle: 10 deg; Beam dimensions: 52x53 mm												
In rays	Density [ray/mm²]	Direct out rays	Refl out rays	Out/In [%]	Out_ref/In [%]		In rays	Density [ray/mm²]	Direct out rays	Refl out rays	Out/In [%]	Out_ref/In [%]
30432	3.6	15110	180	49.65	0.59		30432	3.6	15046	72	49.44	0.24
36852	4.4	18269	179	49.57	0.49		36854	4.4	18204	86	49.39	0.23
43896	5.1	21801	247	49.67	0.56		43894	5.2	21705	113	49.45	0.26
51562	6.1	25603	309	49.65	0.60		51562	6.1	25488	132	49.43	0.26
59832	7.1	29671	303	49.59	0.51		59830	7.1	29547	133	49.38	0.22
68709	8.2	34077	355	49.60	0.52		68710	8.1	33963	183	49.43	0.27
3070861	363	1525320	16759	49.67	0.55		3070872	363	1518335	7513	49.44	0.24
Incidence angle: 20 deg; Beam dimensions: 50x53 mm												
In rays	Density [ray/mm²]	Direct out rays	Refl out rays	Out/In [%]	Out_ref/In [%]		In rays	Density [ray/mm²]	Direct out rays	Refl out rays	Out/In [%]	Out_ref/In [%]
30200	3.8	2822	176	9.34	0.58		30202	3.8	2808	114	9.30	0.38
36576	4.6	3425	223	9.36	0.61		36.576	4.6	3373	129	9.22	0.35
43566	5.4	4108	298	9.43	0.68		43568	5.4	3998	128	9.18	0.29
51164	6.4	4813	343	9.41	0.67		51164	6.4	4699	153	9.18	0.30
59378	7.4	5557	359	9.36	0.60		59378	7.4	5464	190	9.20	0.32
68189	8.5	6383	411	9.36	0.60		68192	8.5	6272	218	9.20	0.32
3047220	377	285765	19257	9.38	0.63		3047242	377	280526	9846	9.21	0.32

Incidence angle: 40 deg; Beam dimensions: 41x53 mm											
In rays	Density [ray/mm^2]	Direct out rays	Refl out rays	Out/In [%]	Out_ref/In [%]		In rays	Density [ray/mm^2]	Direct out rays	Refl out rays	Out/In [%]	Out_ref/In [%]
30001	4.6	0	135	-	0.45		30002	4.6	0	103	-	0.34
36350	5.6	0	141	-	0.39		36350	5.6	0	135	-	0.37
43298	6.6	0	182	-	0.42		43298	6.6	0	139	-	0.32
50856	7.7	0	222	-	0.44		50856	7.7	0	189	-	0.37
59008	9	0	245	-	0.42		59012	9	0	198	-	0.34
67758	10.4	0	327	-	0.48		67760	10.4	0	219	-	0.32
3028576	460	0	12905	-	0.43		3028560	460	0	10796	-	0.36

Notes: "*In rays*" column refers to the number of rays entering the baffle; "*Density*" column reports the number of rays per area; "Direct out rays" column indicates the number of entering rays that exits the baffle without internal reflection; "*Refl. out rays*" column reports the number of entering rays that exits the baffle with at least one internal reflection; "*Out/In*" column shows the ratio between no-reflected outgoing rays and entering rays; "Out_ref/In" column reports the ratio between reflected outgoing rays and entering rays.

Table 15: Straylight analysis results for cylindrical and conical Stavroudis configurations.

As far as the sensitivity analysis is concerned, the most interesting results of Table 15 are those in the "*Out_ref/In*" column, as they represent the contribution of the Stavroudis profile (reflected rays with respect to input rays through conical or cylindrical baffles) to straylight. The "*Out/In*" column considers only the direct rays that can go through the Stavroudis baffles (both conical and cylindrical) without reflections (this contribution could be reduced only by increasing the length of the external baffle).

Another study has been performed to evaluate the performance changes when considering more realistic Stavroudis optical properties as follows:

- each internal surface is 88% reflecting and 12% absorbing;
- each annulus behaves as a perfect Lambertian surface (uniform distribution of reflected light).

Table 16 reports the comparison analysis between the ideal mirror-like and the realistic Stavroudis configuration for cylindrical and conical layouts. Note that an attenuation factor of 100 (~35 reflections) has been considered as ray-tracing reflection threshold in OptiCAD simulations.

Cylindrical					**Conical**			
Incidence angle: 2.5 deg; ray density: ~90 [ray/mm²]								
Entering power [mW]	Direct outgoing power [mW]	Ideal outgoing reflected power [mW]	Real outgoing reflected power [mW]		Entering power [mW]	Direct outgoing power [mW]	Ideal outgoing reflected power [mW]	Real outgoing reflected power [mW]
972.903	820.923	5.64463	1.37885		972.923	821.213	1.18021	0.593986
			1.36375					0.605559
			1.4111					0.60485
			1.36223					0.579633
Incidence angle: 5 deg; ray density: ~90 [ray/mm²]								
Entering power [mW]	Direct outgoing power [mW]	Ideal outgoing reflected power [mW]	Real outgoing reflected power [mW]		Entering power [mW]	Direct outgoing power [mW]	Ideal outgoing reflected power [mW]	Real outgoing reflected power [mW]
970.143	703.337	5.64463	1.35319		970.159	703.903	1.74544	0.739975
			1.36286					0.756392
			1.35729					0.750587
			1.35.688					0.754896
Incidence angle: 10 deg; ray density: ~90 [ray/mm²]								
Entering power [mW]	Direct outgoing power [mW]	Ideal outgoing reflected power [mW]	Real outgoing reflected power [mW]		Entering power [mW]	Direct outgoing power [mW]	Ideal outgoing reflected power [mW]	Real outgoing reflected power [mW]
977.519	480.435	5.48386	1.35788		977.532	481.446	2.34767	0.947506
			1.29886					0.95761
			1.3359					0.955075
			1.32662					0.949982
Incidence angle: 20 deg; ray density: ~95 [ray/mm²]								
Entering power [mW]	Direct outgoing power [mW]	Ideal outgoing reflected power [mW]	Real outgoing reflected power [mW]		Entering power [mW]	Direct outgoing power [mW]	Ideal outgoing reflected power [mW]	Real outgoing reflected power [mW]
969.883	84.9057	6.23155	1.77249		969.891	86.2505	3.13236	1.06713
			1.78048					1.06059
			1.79661					1.01946
			1.71197					0.999247

Incidence angle: 40 deg; ray density: ~115 [ray/mm²]								
Entering power [mW]	Direct outgoing power [mW]	Ideal outgoing reflected power [mW]	Real outgoing reflected power [mW]		Entering power [mW]	Direct outgoing power [mW]	Ideal outgoing reflected power [mW]	Real outgoing reflected power [mW]
963.799	0	4.15691	0.755742		963.811	0	3.4794	0.579372
			0.756013					0.553698
			0.743931					0.579942
			0.725279					0.592144

Notes: "*Entering power*" column reports the total power produced by all the entering rays in the baffle; "*Direct outgoing power*" column indicates the total power of no-reflected outgoing rays; "*Ideal outgoing reflected power*" column indicates the total power of reflected outgoing rays in the case of perfect mirror-like internal surface of the baffle; "*Real outgoing reflected power*" column reports the total power of reflected outgoing rays in the case of a more realistic Stavroudis optical properties.

Table 16: Power comparison between ideal mirror-like and realistic Stavroudis configurations for both layouts.

Comparing "*Ideal outgoing reflected power*" and "*Real outgoing reflected power*" columns (for both Stavroudis layouts) it can be seen that the Stavroudis straylight contribution reduces significantly when considering a more realistic baffle optical configuration. The results indicate also that in a realistic situation the straylight contributions induced by the two Stavroudis layouts are quite similar in orders of magnitude.

As a result, in HRIC external baffle architecture selection other rating parameter such as dimensions and/or weight must be considered.

Comparing the two architectures (cylindrical and conical) is quite evident that the less intrusive configuration is the cylindrical one. So, also to minimise the mass budget requirement, the cylindrical layout for the HRIC external baffle has been confirmed as baseline configuration.

CHAPTER 4

HRIC science operations

In this chapter the HRIC operative modes are discussed. After a brief introduction on the specifications of the main HRIC operative modes, we report the results of two simulations on the coverage capabilities of the instrument in terms of observation quality and produced data volume.

4.1 *HRIC operation definition strategy*

HRIC scientific objectives presented in Section 2.2.1 can be summarised in two macro-areas:

- Origin and evolution of a planet close to the parent star;
- Mercury as a planet: form, interior, structure, geology and composition.

The achievement of such scientific objectives requires to carefully plan HRIC science operations in order to maximise power and data volume resources usage. Such optimisation exercise becomes more critic if it is considered that, differently from the other channels of SIMBIO-SYS, HRIC science operations are driven by the selection of specific targets to be observed. Such a property represents an important degree of freedom for the instrument activity planning, but places several constraints in defining precise scientific operations schedules. In addition, many new interesting targets have been already observed by the MESSENGER probe and others will be certainly identified on the unknown face of Mercury. This will imply a continuous updating of the set of interesting targets to be observed by HRIC.

4.2 *HRIC operative modes*

Following the definition of HRIC science operation sub-theme (see Section 2.2.1), HRIC scientific operative modes have been identified as reported in Table 17.

Mode of operation	Scientific goal	Geometry: MTA range [deg]; spacecraft altitude [km] and latitude [deg]	Typical spatial resolution [m/pxl]	Data rate(1) [kbit/s]	Data volume per orbit(2) [Mbit]
1 Panchromatic high resolution imaging, compression 7x	Geomorphology characterization of selected areas	110-250 400<H<690 -70 ÷ 70	6.5	28 / 2100	250
2 Panchromatic high resolution imaging, compression 2x	Geomorphology characterization of selected areas; best image quality	110-250 400<H<690 -70 ÷ 70	6.5	112 / 8400	1000
3 Panchromatic low resolution imaging, compression 7x	Geomorphology characterization of selected areas; larger coverage	290-70 900<H<1500 -90 ÷ 90	15	7 / 500	95
4 Broadband high resolution imaging, compression 7x	Mineralogy mapping at small scales	130-230 400<H<545 -50 ÷ 50	6	21 / 1550	190
5 Full acquisition mode: panch + broad band, compression 7x	Parallel geomorphology and mineralogy mapping	130-230 400<H<545 -50 ÷ 50	6	50 / 3700	440

(1): Data volume per orbit (2.5 h) / Peak data rate on 1s.
(2): Given numbers are based on the assumption that up to 160 frames are acquired on a single periside orbit and up to 60 frames are acquired on a single aposide orbit.

Table 17: Details of HRIC operative modes and expected data rate and volume.

In the following sub-sections, details on the HRIC operative modes are reported with the aid of a schematic (not to scale) representation of MPO around Mercury.

Table 18, Table 19, Table 20, Table 21 and Table 22 present the data rate (peak and orbit-averaged) and data volume per orbit for each of the discussed operational modes. It is important to note that while the peak data rate gives a design parameter (as it refers to the expected worst case of observations from periherm), the averaged data rate and the data volume per orbit are only an indication of a possible result.

4.2.1 Mode 1: Panchromatic High Resolution Imaging

High resolution images of selected surface features (crater rims, crater ejecta, lobate scarps etc.) are acquired in the panchromatic filter with Mode 1. Mosaicing (both in across-track and along-track directions) is foreseen. Typical conditions for this observation mode are shown in Figure 65.

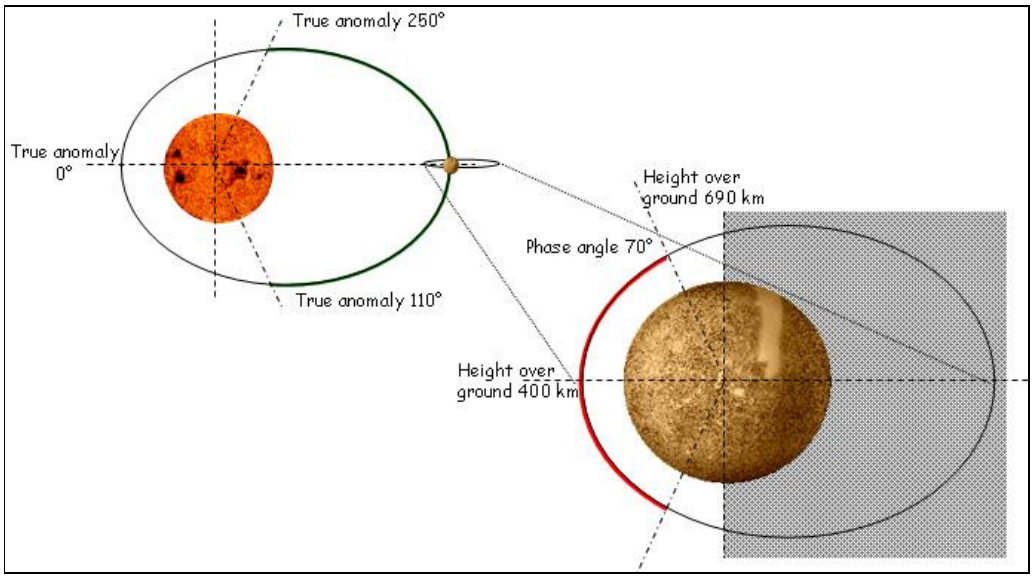

Figure 65: Sketch of the operative conditions for HRIC in the mode 1 and mode 2. The green segment of the Mercury orbit (left) represents the anomaly range; the red segment of the spacecraft orbit (right) represents the (potential) orbital segment of HRIC operation. The two orbital planes are orthogonal. Only at aphelion, the latitude corresponds exactly to the phase angle of observations.

In order to guarantee the coverage of the selected areas, it is possible that acquisitions shall be planned during different passages quite distant in time, but with almost identical observing geometry (including Sun phase angle). During the one year nominal mission, two passages are guaranteed with identical observing conditions and others with different characteristics.

(Compressed) Peak Data Rate	(Compressed) Mean Data Rate	(Compressed) Data Volume/orbit
2350 kbit/s	47 kbit/s	420 Mbit/orbit

Table 18: Summary of HRIC Data Rate characteristics for mode 1. Peak Data Rate refers to the worst case (observations from periherm). Data Volume/orbit and Mean Data Rate are given for the example described in note 2 of Table 17 and shall not be considered valid for average or typical orbit operations.

4.2.2 Mode 2: Panchromatic High Resolution Imaging (low compression)

High resolution images of selected surface features (crater rims, crater ejecta, lobate scarps etc.) are acquired in the panchromatic filter with Mode 2. Mosaicing (both in across-track and along-track directions) is foreseen. Typical conditions for this observation mode are shown in Figure 65. The only difference with respect to Mode 1 is the compression factor: to retrieve images with the best image quality, a lower compression factor (2 instead of 7) is adopted.

(Compressed) Peak Data Rate	(Compressed) Mean Data Rate	(Compressed) Data Volume/orbit
8400 kbit/s	163 kbit/s	1468 Mbit/orbit

Table 19: Summary of HRIC Data Rate characteristics for mode 2. Peak Data Rate refers to the worst case (observations from periherm). Data Volume/orbit and Mean Data Rate are given for the example described in note 2 of Table 17 and shall not be considered valid for average or typical orbit operations.

4.2.3 Mode 3: Panchromatic Low Resolution Imaging

Low resolution images of selected surface features (crater rims, crater ejecta, lobate scarps etc.) are acquired in the panchromatic filter, along the aposide arc and, therefore, with a larger surface coverage. Observations of surface structures at the poles are performed only in this mode. Typical conditions for this observation mode are shown in Figure 66.

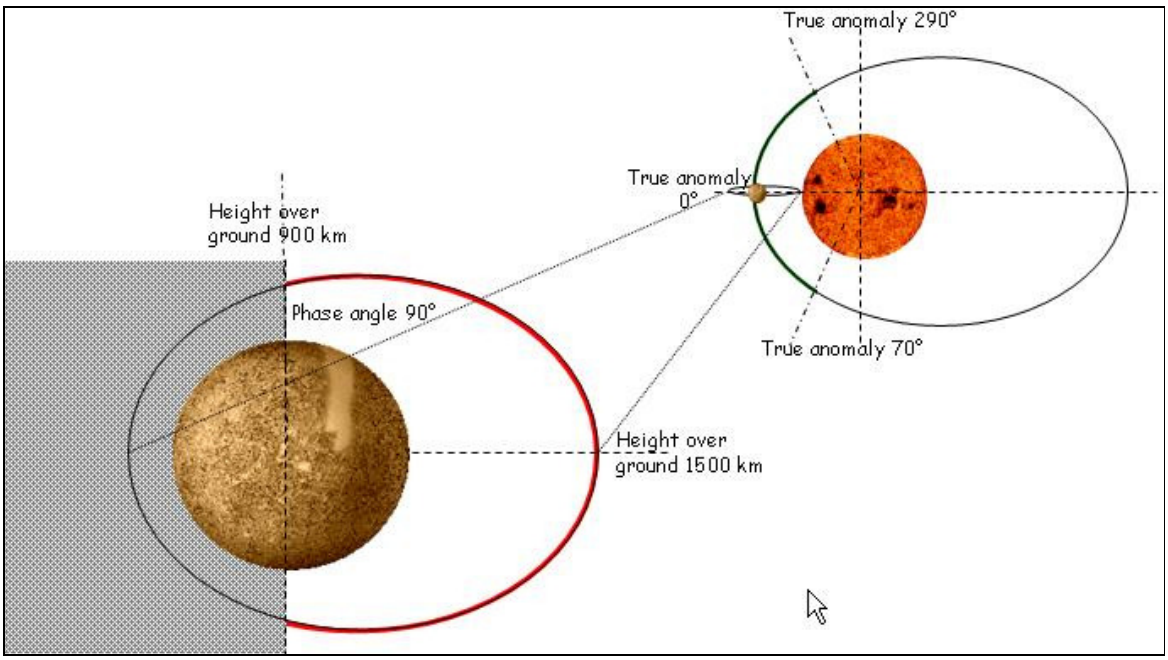

Figure 66: Sketch of the operative conditions for HRIC in the mode 3. The green segment of the Mercury orbit (right) represents the anomaly range; the red segment of the spacecraft orbit (left) represents the (potential) orbital segment of HRIC operation. The two orbital planes are orthogonal. Only at the aphelion, the latitude corresponds exactly to the phase angle of observations.

(Compressed) Peak Data Rate	(Compressed) Mean Data Rate	(Compressed) Data Volume/orbit
1000 kbit/s	17 kbit/s	158 Mbit/orbit

Table 20: Summary of HRIC Data Rate characteristics for mode 3. Peak Data Rate refers to the worst case (observations at poles). Data Volume/orbit and Mean Data Rate are given for the example described in note 2 of Table 17 and shall not be considered valid for average or typical orbit operations.

4.2.4 Mode 4: Broadband Filters High Resolution Imaging

High resolution images of selected surface features (crater rims, crater ejecta, crater floors etc.) are acquired in the broad-band filters. Typical conditions for this observation mode are shown in Figure 67.

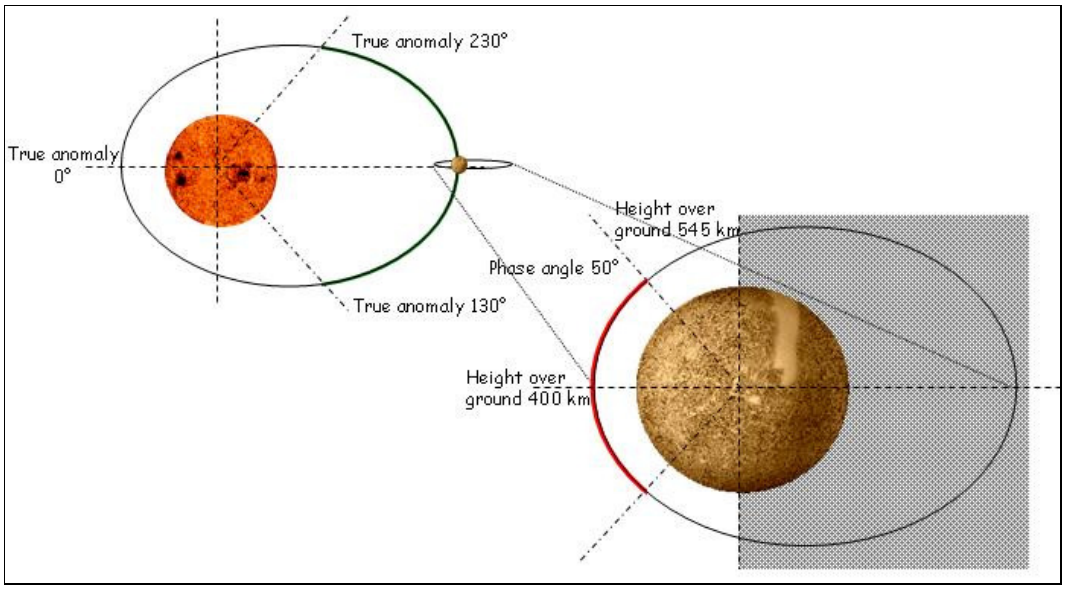

Figure 67: Sketch of the operative conditions for HRIC in the mode 4 and mode 5. The green segment of the Mercury orbit (left) represents the anomaly range; the red segment of the spacecraft orbit (right) represents the (potential) orbital segment of HRIC operation. The two orbital planes are orthogonal. Only at the aphelion, the latitude corresponds exactly to the phase angle of observations.

(Compressed) Peak Data Rate	(Compressed) Mean Data Rate	(Compressed) Data Volume/orbit
1770 kbit/s	21 kbit/s	190 Mbit/orbit

Table 21: Summary of HRIC Data Rate characteristics for mode 4. Peak Data Rate refers to the worst case (observations from periherm). Data Volume/orbit and Mean Data Rate are given for the example described in note 2 of Table 17 and shall not be considered valid for average or typical orbit operations.

4.2.5 Mode 5: Full Acquisition

High resolution images of selected surface features (crater rims, crater ejecta, crater floors, lobate scarps etc.) are acquired in all the 4 filters. Typical conditions for this observation mode are shown in Figure 67.

(Compressed) Peak Data Rate	(Compressed) Mean Data Rate	(Compressed) Data Volume/orbit
3890 kbit/s	67 kbit/s	608 Mbit/orbit

Table 22: Summary of HRIC Data Rate characteristics for mode 5. Peak Data Rate refers to the worst case (observations from periherm). Data Volume/orbit and Mean Data Rate are given for the example described in note 2 of Table 17 and shall not be considered valid for average or typical orbit operations.

4.3 *Coverage and image quality analysis*

HRIC operations shall be spread during one year of nominal mission duration. Specific targets identification shall be done on the basis of previous observations (including MESSENGER data) and the STC/VIHI mapping/spectral imaging indications and findings. On the basis of HRIC science minimum requirement of mapping at least 20% of Mercury surface at high resolution (pixel size between 5 and 8 m/pixel), a planning exercise of HRIC operations during mission has been performed by means of:

- Mapping And Planning Payload Science (MAPPS): it represents the ESA's tool for long-term mission operation planning. It provides (for each MPO instrument) the geo-referenced footprint position and gives all the observational parameters (e.g.: nadir altitude, spacecraft latitude and longitude, Earth reflection angle, Sun elevation and azimuth, perihelion angle, etc.) at any time of the mission.
- HRIC Radiometric Model (Section 3.1): it simulates the high resolution camera behaviour, giving information on the quality of the output images (SNR) with respect to acquisition geometry, detector properties and noise modelling parameters.

In the following, two cases are analysed:

1. Dürer Crater (21.9° N and 119° W): the coloured strips in Figure 68 represent the on-ground projected observations over the crater in adjacent orbits; the shade of strips colour represents the expected quality in terms of SNR. This example evidences how critical is to complete a target coverage at periside (high spatial resolution observations) as strips in subsequent orbits are on-ground separated by about 25 km, while across-track footprint size is about 10 km. On the other hand, with the best observational settings, the image quality is quite good as the SNR varies between 47 (darker shade – top right) and 49 (brightest shade – bottom left) (top value = 50: considering only the PRNU noise term in the RM of section 3.1.1);

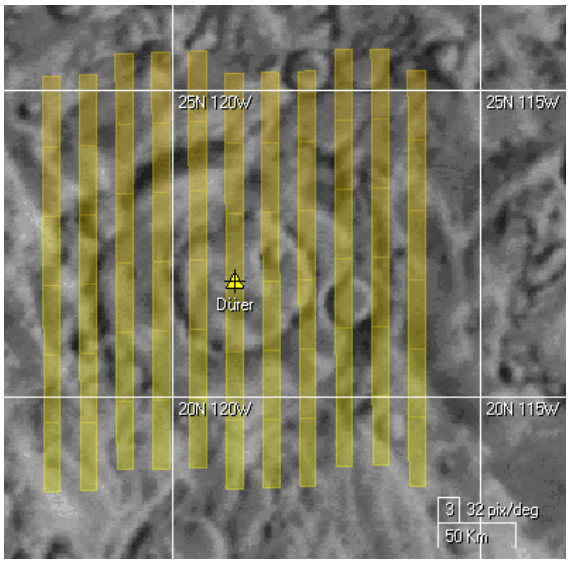

Figure 68: Dürer Crater estimated periside coverage.

2. Vallis Haystack (4.7° N and 46.2° W – Figure 69): this example shows that at aposide (low spatial resolution observations) it is possible to complete the coverage of a selected target (footprint across-track size of about 36 km). Again, considering the optimal observation settings, the image quality is quite good as the SNR varies between 46 (darkest shade – top right) and 48 (brightest shade – bottom left) (top value = 50: considering only the PRNU noise term in the RM of section 3.1.1).

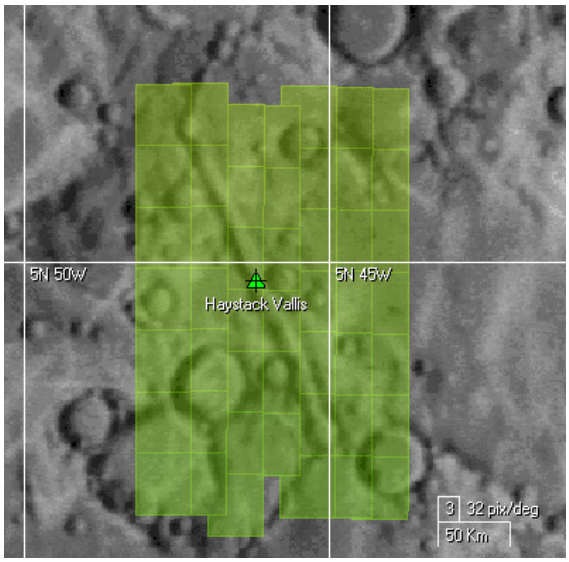

Figure 69: Haystack Vallis estimated aposide coverage.

4.4 *Data volume distribution simulation*

4.4.1 Starting assumptions

A simulation on HRIC data volume distribution with time has been performed in order to estimate the amount of data and the coverage percentage during HRIC operations. For such analysis it has been considered:

- HRIC science mode specifications (Table 17);
- Mapping And Planning Payload Science (MAPPS) tool;

In studying the distribution of the data volume produced by HRIC some assumptions have been done:

- 6 months operations;
- 100 targets randomly distributed over the Mercury surface;
- Targets Latitude range: 0° ÷ 70° (North and South);
- Targets cover 10% of planetary surface which correspond to the half of planned scientific operations;
- Distribution of coverage with different operative modes: 5% Panchromatic high resolution, 3% Panchromatic low resolution, 2% Full acquisition (Table 23);
- Target dimensions are randomly distributed in the range 1600 ÷ 250000 km^2;

Mode of operation	Code (HRIC science mode – Table 17)	Scientific goal	Coverage [%]	MTA (*) [deg]	Viewing conditions (*)
Panchromatic high resolution imaging	0 (1)	Geomorphology characterization of selected areas. Compression factor 7x	5	110-250	periside, phase angle < 70°
Panchromatic low resolution imaging	1 (3)	Geomorphology characterization of selected areas; larger coverage. Compression factor 7x	3	290-70	aposide, phase angle < 90°
Full acquisition mode (panch + broad-band)	2 (5)	Parallel geomorphology and mineralogy mapping. BB Filters binning (2x2); compression factor 7x	2	110-250	periside, phase angle < 50°

(*):Position is given in deg of true anomaly, starting from 0 at perihelion. Position range is given as a reference; observations outside the given range (high phase angle) can be considered.

Table 23: Details on data rate/volume of HRIC operative modes for data volume simulation.

Considering the above operations configuration, we have defined a set of 100 targets randomly distributed over the Mercury surface, with different dimensions and whose total area gives the 10% of planetary surface (Figure 70), which corresponds to the half of planned operations activities for HRIC minimum requirement of mapping at high resolution.

Starting from the "observable-target" list, MAPPS tool has been used to retrieve the coverage information for each target: the needed number of acquisitions, the geographical position, the relative position of the spacecraft, etc.

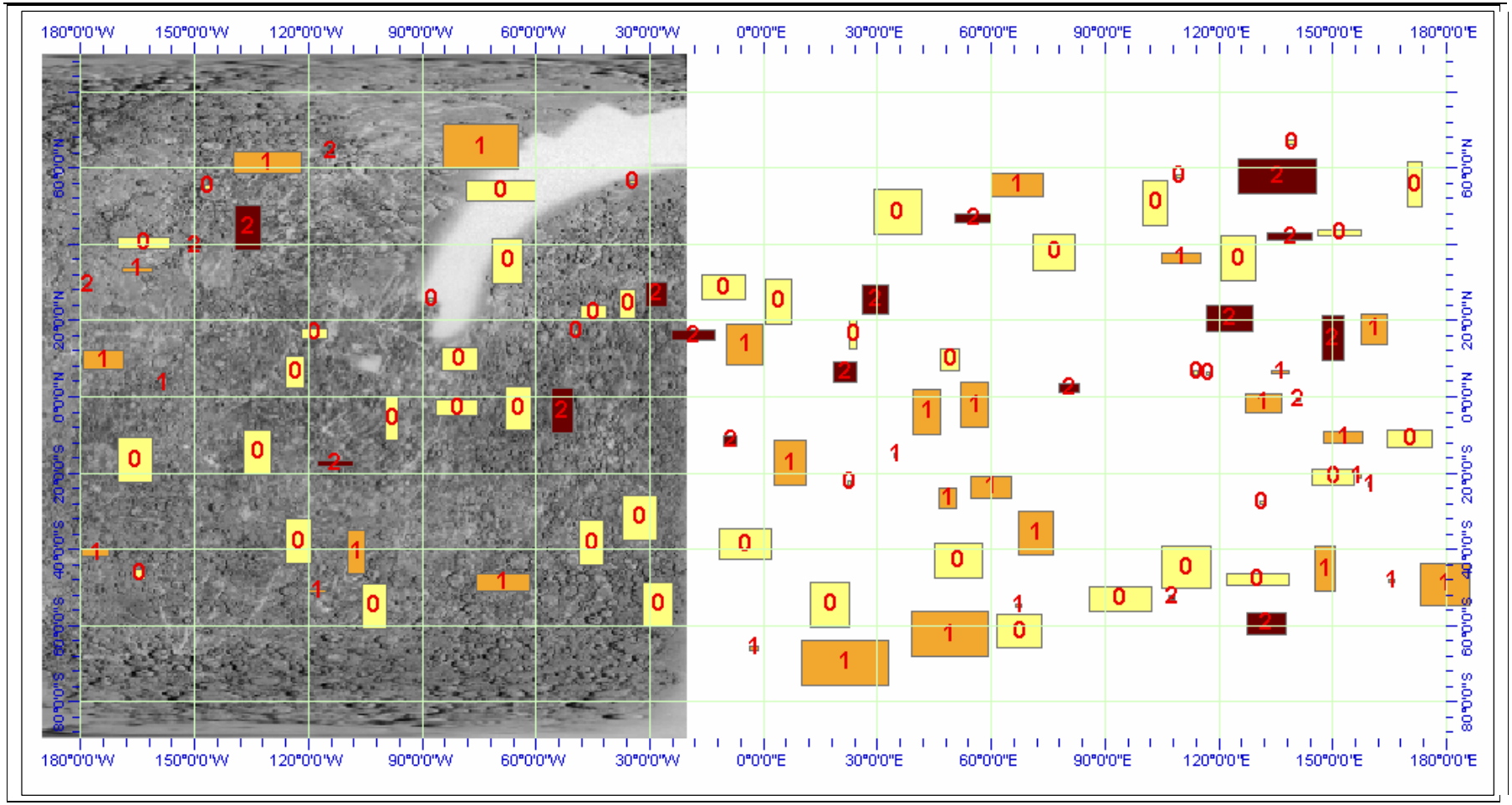

Figure 70: Simulated operative scenario: each target is characterised by a code (plus a colour) indicating the operation mode assigned (see Table 23). The code 0 (yellow) refers to the Pancromatic high resolution operative mode; the code 1 (gold) refers to the Pancromatic low resolution mode; the code 2 (brown) refers to the Full operative mode.

The MAPPS text output file for each target has been converted into a *shapefile*; each *shapefile* consists of rectangular box whose geographical coordinates correspond to the ones reported for each observation in the MAPPS text output file (Figure 71).

To each entity has been assigned some useful metadata (i.e., local resolution) necessary for determining the required data volume.

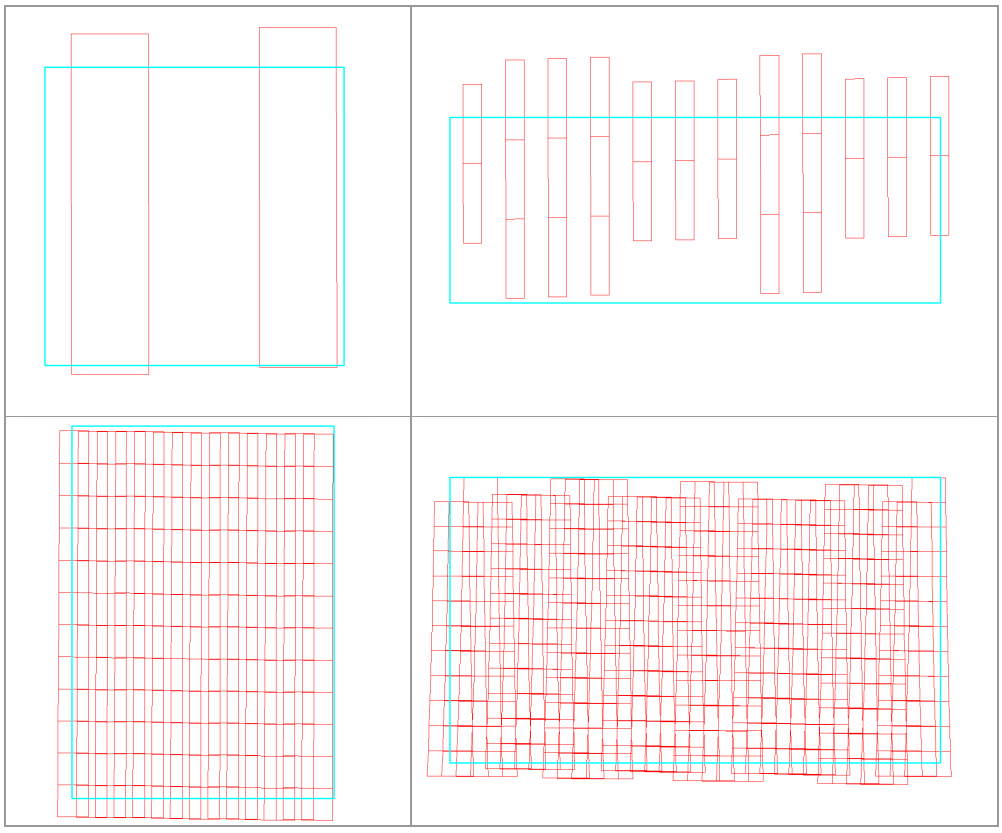

Figure 71: Examples of MAPPS output coverage estimation: critical observations (top) and extreme overlapping (bottom).

By means of ESRI ArcGIS[3] tool, each *shapefile* has been edited in order to reduce overlapping factor and then projected into a sinusoidal projection in order to correctly determine the area of each entity. Once known the correct area of each entity, the related data volume has been derived considering the local spatial resolution (stored as metadata) and the associated operative parameters (e.g., binning factor, compression factor).

[3] Suite of applications aiming to perform GIS tasks such as mapping, geographic analysis, data editing and management and geoprocessing.

4.4.2 Simulation results

Starting from the above assumptions, the simulation of HRIC data volume distribution has produced the following results. In order to simplify visualization, they have been grouped in 4 blocks of 25 targets each; for each block a graph shows two types of information are reported:

1. data volume per each target (purple bars);
2. ratio between assigned and observed area (blue line): values < 1 indicate that MAPPS produced observations for a total area lower than the required; = 1 means that MAPPS output fits to the area observation requirement; > 1 means that MAPPS indicates a set of observations whose total areas overcome the assigned one.

Figure 72 shows the first group of 25 targets. Mode of operation for targets 1-25 is Panchromatic High resolution (code 0 – see Table 23).

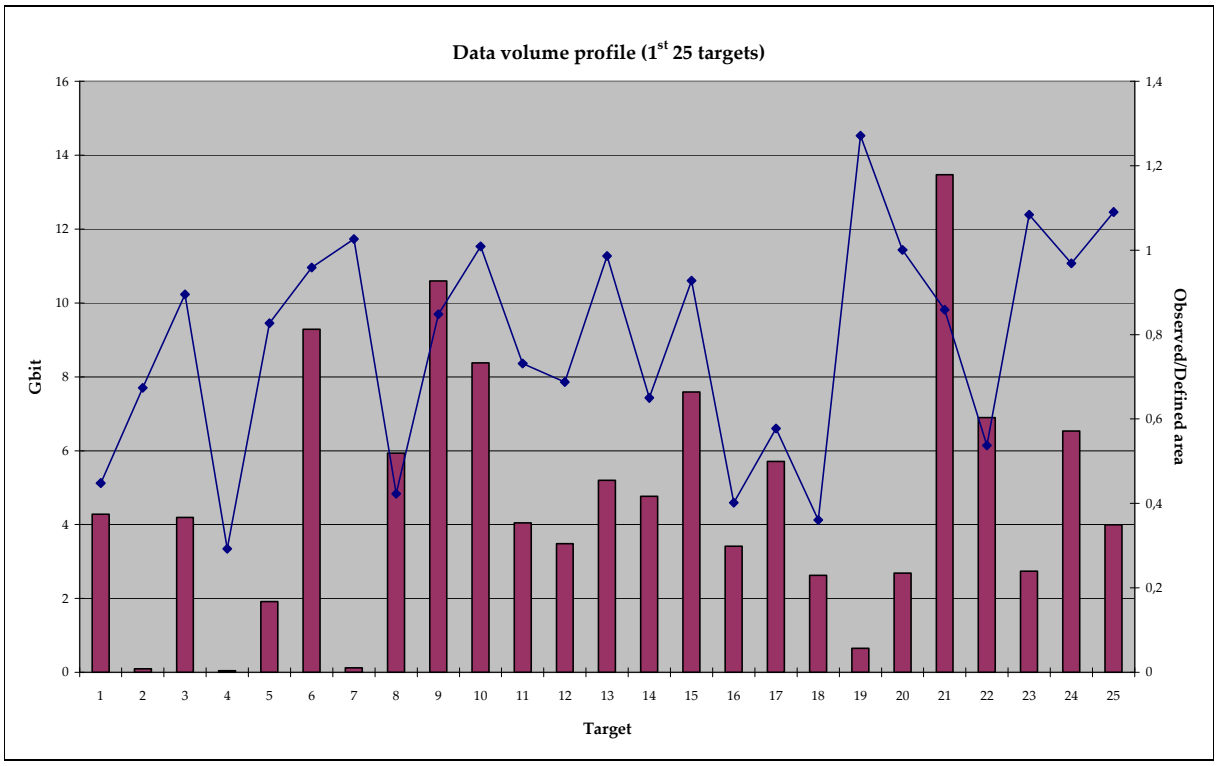

Figure 72: MAPPS-derived data volume profile for each of the first 25 targets. The blue line represents the observed vs. assigned area ratio.

Figure 73 shows the second group of 25 targets. Mode of operation for targets 25-48 is Panchromatic High resolution, while for targets 49-50 is Panchromatic Low resolution.

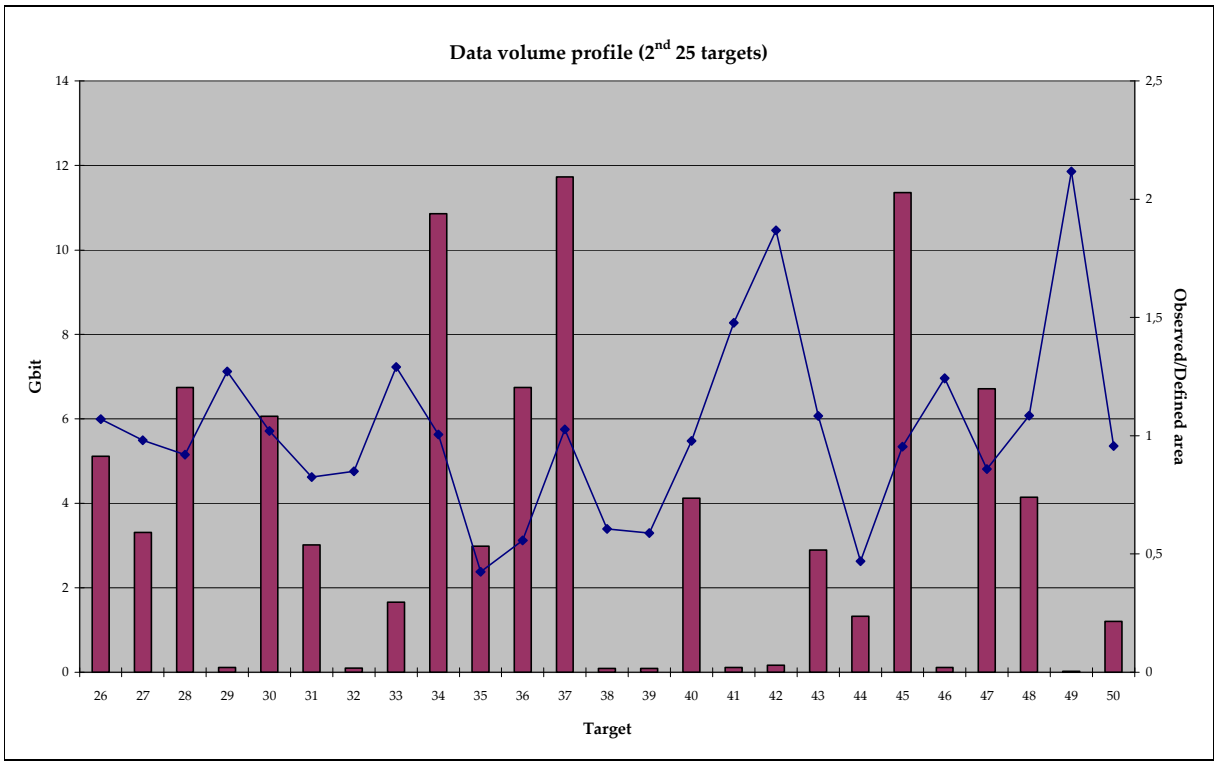

Figure 73: MAPPS-derived data volume profile for each of the second 25 targets. The blue line represents the observed vs. assigned area ratio.

Figure 74 shows the third group of 25 targets. Mode of operation for targets 51-75 is Panchromatic Low resolution.

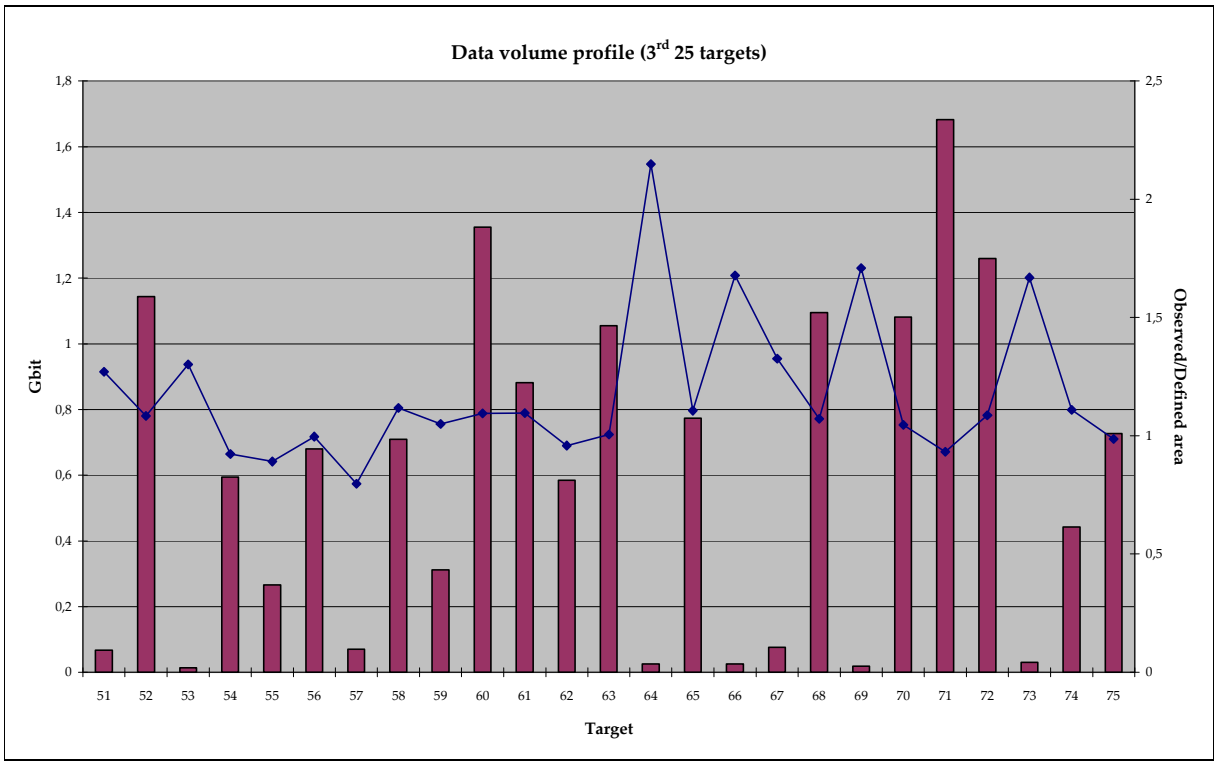

Figure 74: MAPPS-derived data volume profile for each of the third 25 targets. The blue line represents the observed vs. assigned area ratio.

Figure 75 shows the forth group of 25 targets. Mode of operation for targets 76-80 is Panchromatic Low resolution, while for targets 81-100 is Full Acquisition mode.

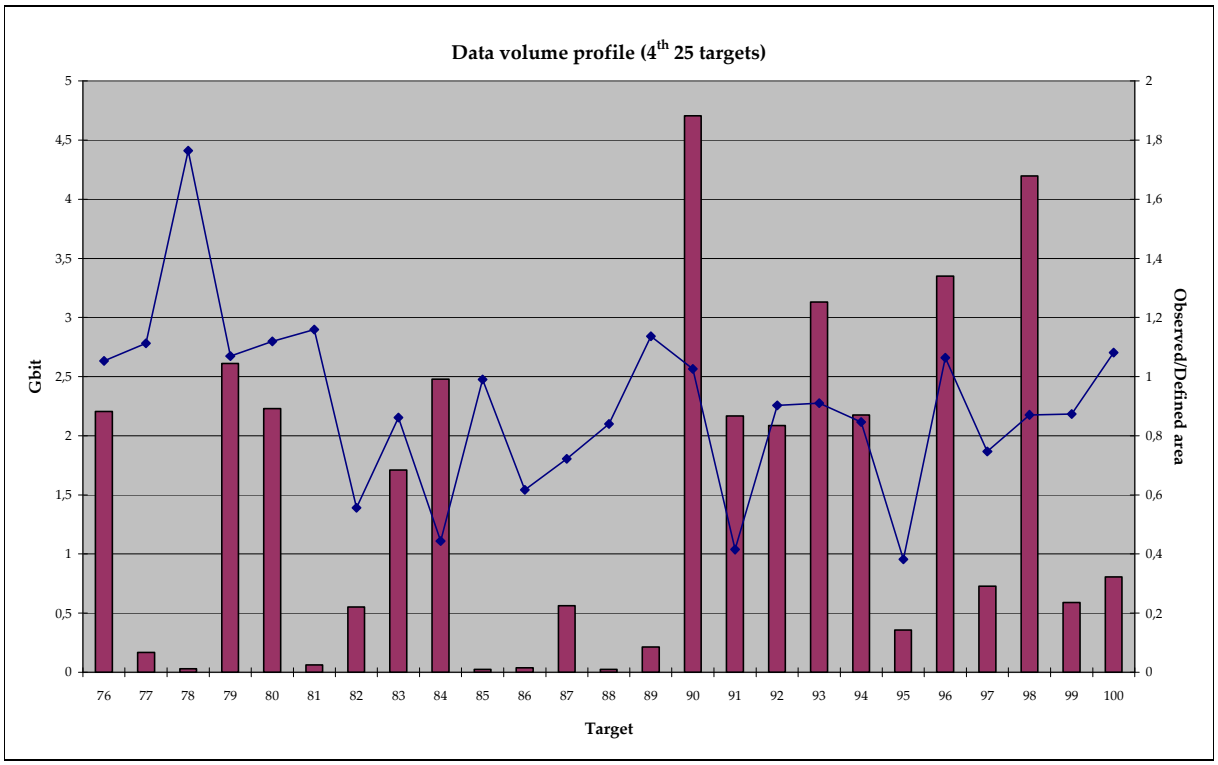

Figure 75: MAPPS-derived data volume profile for each of the fourth 25 targets. The blue line represents the observed vs. assigned area ratio.

Figure 76 reports the data volume behaviour vs. orbit relevant to the simulated acquisition scenario.

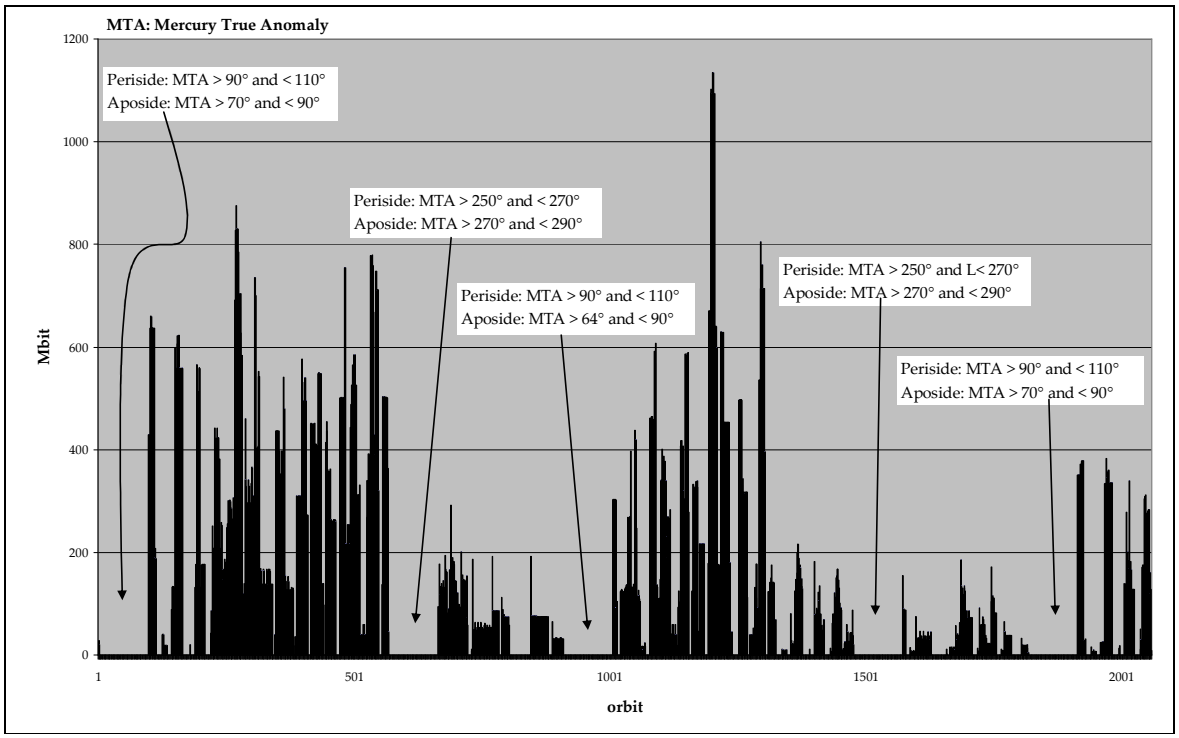

Figure 76: Data volume vs. orbit.

Figure 77 shows the cumulative data volume profile.

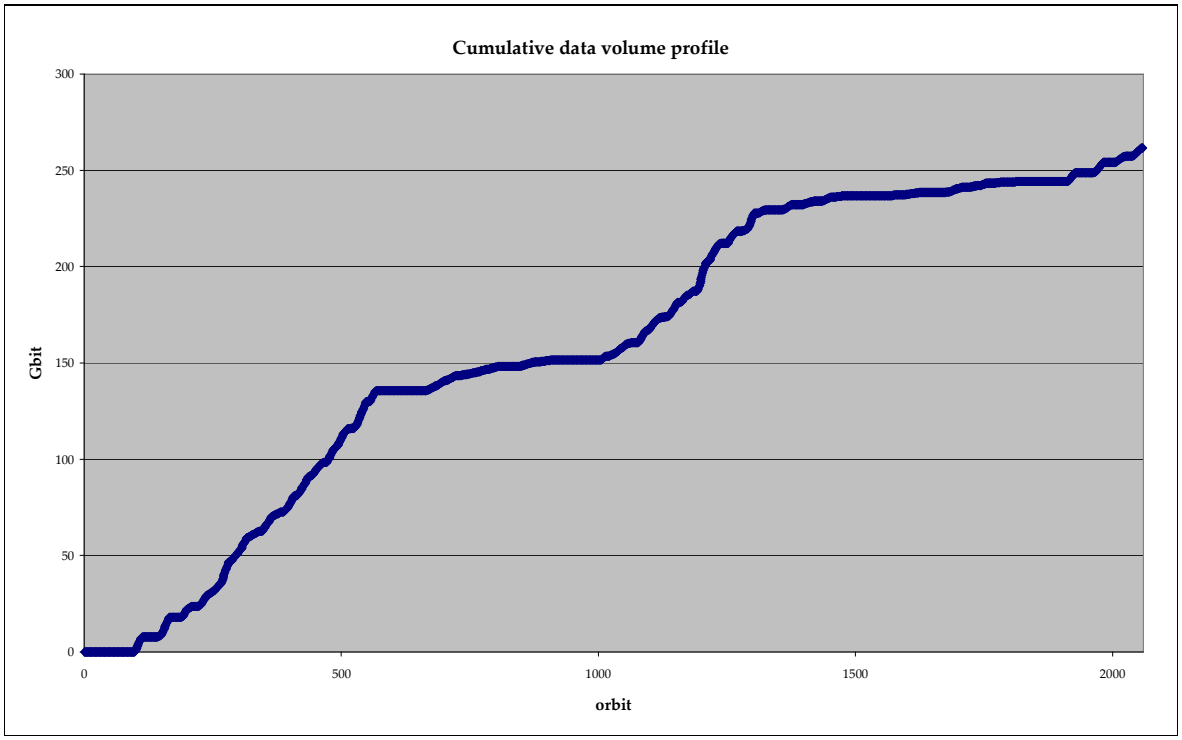

Figure 77: Cumulative data volume vs. orbit.

Finally, the comparison between the HRIC operation specifications reported in Table 24

Operative Mode	Number of filters	Binning	Compression factor	Typical pixel size [m/pxl]	Percentage of Mercury's surface
1	1	no	7	6.5	5 %
2	1	no	2	6.5	1 %
3	1	no	7	16	5 %
4	3	2×2	7	6	5 %
5	4	2×2 (no pan)	7	6	4%

Table 24: Science operative mode specifications.

(linked to Table 17) and the results of the simulation (grouped by operative modes) is reported in Table 25.

	MAPPS			Reference		
Science mode	Mean resolution [m/pxl]	Area [m²]	Data volume [Gbit]	Mean resolution [m/pxl]	Area [m²]	Data volume [Gbit]
Mode 1 (code 0)	6.16	$3.2 \cdot 10^{12}$ (4.27 %)	172	6.5	$3.7 \cdot 10^{12}$ (5 %)	177
Mode 3 (code 1)	16	$2.6 \cdot 10^{12}$ (3.48%)	19.3	15	$2.2 \cdot 10^{12}$ (3 %)	19.9
Mode 5 (code 2)	5	$8.9 \cdot 10^{11}$ (1.2%)	24.7	6	$1.5 \cdot 10^{12}$ (2 %)	36.4
Tot data volume [Gbit]	216			233		

Table 25: Comparison of data volume production between output MAPPS simulation and operation modes specification.

Data reported in Table 25 show that the simulation output fits quite well to the theoretical estimations of required data volume production for the specified operative modes. Differences in the data volume allocation derive essentially from two factors: the observed area percentage and the difference in mean spatial resolution.

4.4.3 Stressing operative conditions

Simulations of section 4.4.2 represent a possible operative scenario in which a set of realistic interesting targets are uniformly distributed over the planet surface. This distribution directly influences the estimation of the data volume production; this means that simulation outputs could change dramatically if particular constraints about targets distribution occur. As consequence, instantaneous (Figure 76) and cumulative (Figure 77) data volume profiles could be quite different, becoming particularly stressing with respect to spacecraft allocated resources. In the above simulation, the most critical operative condition regards the observation of target 21 because it represents the largest target between those producing the highest data volume (Figure 78-left).

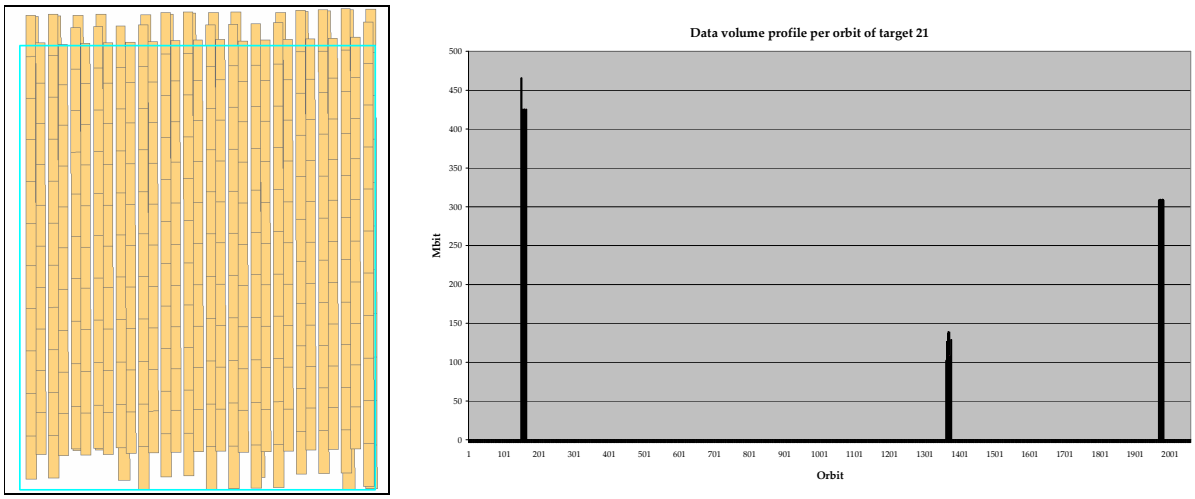

Figure 78: Left – the green box represents the defined area, while the gold rectangles represent the MAPPS observations for target 21. Right – instantaneous data volume profile vs. orbit for target 21.

Figure 78-right shows that, to observe 85% of target 21 surface (see Figure 72), HRIC will require (as MAPPS indicates) three operative orbit ranges (between orbit 151 and orbit 166, between orbit 1362 and orbit 1377 and between orbit 1968 and orbit 1982) with a peak data volume production of more than 450 Mbit per orbit.

Even though the case of target 21 is the most critical with respect to the data volume production per orbit in our scenario, it does not represent the worst possible case.

The most critical operative configuration, with respect to space-craft storage/downlink capabilities, is the one corresponding to a continuous pole-to-pole observation for several subsequent orbits. In particular, in the case of "mode 0" operative condition (see Table 23)

to reach the 5% of planetary surface in six operative months, about 34 orbits are required. Considering that a pole-to-pole operative condition implies about 4.5 Gbit of data volume (considering a mean spatial resolution of 7 m/pixel), to complete the 5% of planetary surface in 34 following orbits, 153 Gbit are required.

The resulting data volume from HRIC during the foreseen scientific operations is compatible with the HRIC data volume specifications (Table 24).

To be noted that the coverage problem, clearly shown in Figure 71 – top, from Figure 72 to Figure 75 (blue line) and in Figure 78 – left, suggests that it will be very difficult completing a high-resolution mosaic in half nominal mission period (6 months). It is also clear that in order to guarantee the possibility to build "large" mosaics (i.e., larger than few images along longitude) it is mandatory considering HRIC operational phases as long as possible during the whole mission, in order to increase the number of HRIC passages above each target and acquire data from the un-observed regions left from previous passages. A careful long-term (mission scale) planning is needed to obtain this result.

Conclusions

The research activity documented in this thesis concerns the design and the development of the high spatial resolution camera (HRIC) of the ESA Cornerstone mission BepiColombo to Mercury. In particular, the discussed subjects are:

1. Imaging system performances

   HRIC is the scientific instrument aboard the BepiColombo mission devoted to the visual investigation at high spatial resolution of the Mercury surface. Its main scientific objective is to characterise short scale planetary surface features in order to better understand the geological evolution of the planet (endogenic and exogenic processes). For this reason, several ad hoc tools have been developed with the aim of estimating the instrument imaging performances. In particular, it has been developed:

   - HRIC Radiometric Model (HRIC-RM): it consists of a mathematical description of the radiance-to-signal conversion process performed by the instrument with respect to the Mercury spectral radiance, acquisition geometry and system specifications (optical design, filter and detector specifications). In addition, the model contains a complete description of all the degradation terms that affect the output signal reducing its quality. One of the most important output of the HRIC-RM is the Signal-to-Noise-Ratio (SNR) which represents the standard parameter for imaging system performance analysis. By means of the HRIC-RM, the SNR parameter can be calculated in every operative condition and considering different surface targets (position and albedo coefficient) accordingly to the instrument scientific objectives and allocated resources.
   - HRIC Simulator (HRIC-SIM): with this tool it is possible to obtain an estimation of the output images of the HRIC instrument. It contains all the mathematical equations of the HRIC-RM, an analytical description of the HRIC optical design and the compression and preliminary post-processing

algorithms. Starting from a synthetic or realistic input scenario the simulator produces the expected output image with all the degradation effects due to optics, the HRIC-RM and image processing algorithms.

- Filter optical properties and Ghosts analysis: the scientific treatment of HRIC output data must consider key spectral and optical aspects. For this reason, a quantitative analysis of the out-of-band spectral radiance contribution on image signal has been done. This analysis has been extended considering internal FPA reflections in order to determine the effects of Ghosts in terms of spectral density power and spatial distribution.
- Analysis of external baffle optical properties: HRIC is equipped with an external baffle, whose principal function is to protect the camera optical entrance against out-of-field radiance. HRIC external baffle has been designed considering thermal aspects: its layout profile (Stavroudis configuration) has been selected to maximise the rejection of the thermal load coming from the Mercury surface. This design concept is critical from the optical point of view as it is characterised by several edges potentially becoming sources of straylight. A complete characterisation of the optical behaviour of the HRIC external baffle has been done by means of ray-tracing tool (OptiCad) on two different configurations (cylindrical and conical).

2. Operations

Operations have to be carefully planned to properly combine BepiColombo orbital characteristics, HRIC optical performances and allocated resources of power and data volume, in order to maximise the scientific return of the mission. For this purpose, two ad hoc MAPPS-based (the ESA's tool for mission operation planning) tools have been developed to estimate the HRIC coverage capabilities and data volume distribution along the mission lifetime:

- HRIC target coverage and data quality

  This tool allows us to determine the amount and the quality (in terms of SNR) of observations required or allowed by the orbital configuration to observe a specified surface target.

- HRIC data volume production

  Starting from a representative operative scenario with targets uniformly distributed on the planet surface, this tool allows us to determine, with a user defined overlapping percentage, the orbital and cumulative data volume production.

The HRIC imaging and operative performances investigation tools developed for the PhD research activity have been used to evaluate and to validate the HRIC imaging performances. The obtained results have demonstrated the high quality of the instrument design and its compliance with the scientific objectives and requirements. As a result, HRIC design has been frozen and its realization is in line with the ESA instrument design schedule.

In this context, the above described tools and analyses will be of paramount importance for the upcoming activities. In particular:

- Radiometric Model: HRIC-RM will be used to analyse and compare the instrument performances with respect to measured properties of the optical and detector components coming from the suppliers. In addition, HRIC-RM, thanks to its flexibility, will be used to define instrument calibration methodologies and measurement accuracy level;
- HRIC Simulator: its architecture allows us to directly interface the tool with other image processing software in order to evaluate the observations quality (or features reconnaissance);
- Coverage and data volume production tools: results of these tools will be used to design mission operative scenarios compatible with spacecraft orbital configuration, power and data volume resources and instrument scientific objectives.

Bibliography

[1] Encrenaz T. et al., *The Solar System*, Springer 3rd edition, pp. 26-30, 2004.

[2] Benz W. et al., *Collisional stripping of Mercury's mantle*, Icarus, Volume 74, Issue 3, pp. 516-528, 1988.

[3] Cameron A. G. W., *The partial volatilization of Mercury*, Icarus, Volume 64, Issue 2, pp. 285-294, 1985.

[4] Stevenson D. J., *Mercury's magnetic field – A thermoelectric dynamo?*, Earth and Planetary Science Letters, Volume 82, pp. 114-120, 1987.

[5] Christensen U. R., *A deep dynamo generating Mercury' magnetic field*, Nature 444, pp. 1056-1058, 2006.

[6] Stevenson D. J. et al., Magnetism and thermal evolution of the terrestrial planets, Icarus, Volume 54, pp. 466-489, 1983.

[7] Strom R. G. et al., *The cratering record on Mercury and the origin of impacting objects*, University of Arizona Press, pp. 336-373, 1988.

[8] Melosh H. J. et al., *The tectonics of Mercury*, University of Arizona Press, pp.374-400, 1988.

[9] Burns J. A., *Consequences of the tidal slowing of Mercury*, Icarus, Volume 31, pp. 221-243, 1976.

[10] Strom R. G. et al., *The geology of terrestrial planets*, NASA SP-469, 1984.

[11] Schultz P.H. et al, *Seismic effects from major basin formation on the Moon and Mercury*, The Moon, Volume 12, pp. 159-177, 1975.

[12] Hostetler G. J. et al., *On the early global melting of the terrestrial planets*, Proceedings LPSC, Volume 11, pp. 1915-1929, 1980.

[13] Jeanloz R. et al., *Evidence for a basal-free surface on Mercury and implications for internal heat*, Science, Volume 268, pp. 1455-1458, 1995.

[14] Broadfoot A. L. et al., *Mariner 10 – Mercury atmosphere*, Geophysics Res. Letters, Volume 3, pp. 577-580, 1976.

[15] Potter A. E. et al., *Discovery of sodium in the atmosphere of Mercury*, Science, Volume 229, pp. 651-653, 1985.

[16] Potter A. E. et al., *Potassium in the atmosphere of Mercury*, Icarus, Volume 67, pp. 336-340, 1986.

[17] Bida T. A. et al., *Discovery of calcium in the Mercury's exosphere*, Nature, Volume 404, pp. 159-161, 2000.

[18] McNutt R. L. Jr et al., *The MESSENGER mission to Mercury: development history and early mission status*, Advanced in Space Research, 2006.

[19] Hawkins S. E. et al., *The Mercury Dual Imaging System on the MESSENGER spacecraft*, Space Science Review, Volume 131, Issue 1-4, pp. 247-338, 2007.

[20] Goldsten J. O., *The MESSENGER Gamma-ray and Neutron Spectrometer*, Space Science Review, Volume 131, Issue 1-4, pp. 339-391, 2007.

[21] Schlemm C. E., *The X-Ray Spectrometer on the MESSENGER spacecraft*, Space Science Review, Volume 131, Issue 1-4, pp. 393-415, 2007.

[22] Anderson B. J., *The Magnetometer instrument of MESSENGER*, Space Science Review, Volume 131, Issue 1-4, pp. 417-450, 2007.

[23] Cavanaugh J. F., *The Mercury Laser Altimeter for the MESSENGER mission*, Space Science Review, Volume 131, Issue 1-4, pp. 451-479, 2007.

[24] McClintock W. E., *The Mercury Atmospheric and Surface Composition Spectrometer for the MESSENGER mission*, Space Science Review, Volume 131, Issue 1-4, pp. 481-521, 2007.

[25] Andrews G. B., *The Energetic Particle and Plasma Spectrometer Instrument on the MESSENGER spacecraft*, Space Science Review, Volume 131, Issue 1-4, pp. 523-556, 2007.

[26] Srinivasan D. K., *The Radio Frequency Subsystem and Radio Science on the MESSENGER mission*, Space Science Review, Volume 131, Issue 1-4, pp. 557-571, 2007.

[27] Solomon S. C. et al., *Mercury: the enigmatic innermost planet*, Earth and Planetary Science Letters, Volume 216, Issue 4, pp. 441-455, 2003.

[28] Thomas N., *The BepiColombo Laser Altimeter (BELA): concept and baseline design*, Planetary and Space Science, Volume 55, Issue 10, pp. 1398-1413, 2007.

[29] Iess L., *MORE: An advanced tracking experiment for the exploration of Mercury with the mission BepiColombo*, Acta Astronautica, Volume 65, Issues 5-6, pp. 666-675, 2009.

[30] Iafolla V., *Italian Spring Accelerometer (ISA): A fundamental support to BepiColombo Radio Science Experiments*, Planetary and Space Science, In Press, 2009.

[31] Glassmeier K. H., *The fluxgate magnetometer of the BepiColombo Mercury Planetary Orbiter*, Planetary and Space Science, In Press, 2008.

[32] Hiesinger H., *The Mercury Radiometer and Thermal Infrared Spectrometer (MERTIS) for the BepiColombo mission*, Planetary and Space Science, In Press, 2008.

[33] Mitrofanov I. G., *The Mercury Gamma and Neutron Spectrometer (MGNS) on board the Planetary Orbiter of the BepiColombo mission*, Planetary and Space Science, In Press, 2009.

[34] Fraser G. W., *The mercury imaging X-ray spectrometer (MIXS) on BepiColombo*, Planetary and Space Science, In Press, 2009.

[35] Huovelin J., *Solar Intensity X-ray and particle Spectrometer (SIXS)*, Planetary and Space Science, In Press, 2008.

[36] Chassefière E., *PHEBUS: A double ultraviolet spectrometer to observe Mercury's exosphere*, Planetary and Space Science, In Press, 2008.

[37] Orsini S., *SERENA: A suite of four instruments (ELENA, STROFIO, PICAM and MIPA) on board BepiColombo-MPO for particle detection in the Hermean environment*, Planetary and Space Science, In Press, 2008.

[38] Flamini E., *SIMBIO-SYS: The spectrometer and imagers integrated Observatory System for the BepiColombo Planetary Orbiter*, Planetary and Space Science, In Press, 2009.

[39] Baumjohann W., *Magnetic field investigation of Mercury's magnetosphere and the inner heliosphere by MMO/MGF*, Planetary and Space Science, In Press, 2008.

[40] Saito Y., *Scientific objectives and instrumentation of Mercury Plasma Particle Experiment (MPPE) onboard MMO*, Planetary and Space Science, In Press, 2008.

[41] Kasabe Y., *The Plasma Wave Investigation (PWI) onboard the BepiColombo/MMO: First measurement of electric fields, electromagnetic waves, and radio waves around Mercury*, Planetary and Space Science, In Press, 2008.

[42] Yoshikawa I., *Observation of Mercury's sodium exosphere by MSASI in the BepiColombo mission*, Planetary and Space Science, Volume 55, Issue 11, pp. 1622-1633, 2007.

[43] Nogami K., *Development of the Mercury dust monitor (MDM) onboard the BepiColombo mission*, Planetary and Space Science, In Press, 2008.

[44] Neukum G. et al., *Geologic evolution and cratering history of Mercury*, Planetary and Space Science, Volume 49, Issue 14-15, pp. 1507-1521, 2001.

[45] Martellato E. et al., C*ratering analysis and age determination of the Mercury's surface*, 37th COSPAR Scientific Assembly, p. 1927, 2008.

[46] Jehn R., et al., *Estimating Mercury's 88-day libration amplitude from orbit*, Planetary and Space Science, Volume 52, Issue 8, p. 727-732, 2004.

[47] Marra G. et al., *The optical design and preliminary opto-mechanical tolerances of the high resolution imaging channel for the BepiColombo mission to Mercury*, Opto-mechanical Technologies for Astronomy, Proceedings of the SPIE, Volume 6273, pp. 627328, 2006.

[48] Holst G. C., *CCD ARRAYS, CAMERAS and DISPLAYS* – 2nd edition, SPIE Optical Engineering Press, Washington, 1998.

[49] Fiete R. D., *Image quality and λFN/p for remote sensing systems*, Eastman Kodak Company, 1999.

[50] Zanoni V., *The Joint Agency Commercial Imagery Evaluation (JACIE) team and the product characterisation approach*, ISPRS commission I/WG2 international workshop on radiometric and geometric calibration meeting, 2003.

[51] Stanley T. et al., *Spatial resolution characterisation for aerial digital imagery*, Civil commercial imagery evaluation workshop, 2006.

[52] Pagnutti M., *Measurement sets and sites commonly used for high spatial resolution image product characterisation*, EO/IR Calibration and Characterisation Workshop, 2006.

[53] USGS team, *Current aerial mapping sensor test and evaluation activities and results*, American society for photogrammetry and remote sensing annual meeting, 2005.

Glossary

ADC	Analogue to Digital Conversion
APID	Application Process ID
Aposide	MPO orbit portion farther from the Mercury surface (1000-1508 Km of altitude)
ASI	Agenzia Spaziale Italiana
AU	Astronomical Unit
CMOS	Complementary Metal Oxide Semiconductor
CNES	Centre National d'Etudes Spatiales
CPM	Chemical Propulsion Module
CPCU	Command and Control Processor Unit
CU	Compression Unit
DC	Dark Current
DCNU	Dark Current Non Uniformity
DMC	Dark Mirror Coating
EE	Encircled Energy
EP	Entrance Pupil
ESA	European Space Agency
ER	Edge Response
FOV	Field Of View
FPGA	Field Programmable Gate Array
FPN	Fixed Pattern Noise
GIQE	General Image Quality Equation
GUI	Graphic User Interface
IFE	Instrument Front End
HK	HouseKeeping
HiRISE	High Resolution Imaging Science Experiment
HRIC	High Resolution Imaging Channel
HRIC-RM	High Resolution Imaging Channel – Radiometric Model
HRIC-SIM	High Resolution Imaging Channel – SIMulator
IACG	Inter-Agency Consultative Group
ISAS	Institute of Space and Astronautical Science
IDL	Interactive Data Language
IOBT	Instrument On-Board Time
JAXA	Japanese Aerospace eXploration Agency
MAPPS	Mapping And Planning Payload Science
ME	Main Electronics
MESSENGER	MErcury Surface Space ENvironment GEochemistry and Ranging
MEWG	Mercury Exploration Working Group
MMO	Mercury Magnetometric Orbiter
MORE	Mercury Orbiter Radio-science Experiment
MOI	Mercury Orbit Insertion
MPO	Mercury Planetary Orbiter
MRO	Mars Reconnaissance Orbiter
MTA	Mercury True Anomaly
MTF	Modulation Transfer Function
MTF-SYS	Modulation Transfer Function–SYStem
NASA	National Aeronautics and Space Administration
NIIRS	National Imagery Interpretability Rating Scale

OBT	On-Board Time
OTF	Optical Transfer Function
PE	Proximity Electronics
Periside	MPO orbit portion closer to the Mercury surface (400-900 Km of altitude)
PRNU	Photo Response Non Uniformity
PSF	Point Spread Function
PTF	Phase Transfer Function
RER	Relative Edge Response
RMS	Root Mean Square
ROIC	Read-Out Integrated Circuit
SCSS	Steering Committee of Space Science
SEPM	Solar Electric Propulsion Module
SIMBIO-SYS	Spectrometer and Imagers for Mpo Bepicolombo Integrated Observatory – SYStem
SPC	Science Programme Committee
SNR	Signal to Noise Ratio
SS	Solar System
TC	Tele-Command
TM	TeleMetry

Ringraziamenti

La realizzazione di questa tesi è stata possibile grazie alla disponibilità del Prof. Luigi Colangeli, direttore dell'Osservatorio Astronomico di Capodimonte e Co-Principal Investigator dello strumento HRIC della missione ESA BepiColombo che mi ha offerto l'opportunità di lavorare per un progetto all'avanguardia nel campo dell'esplorazione spaziale in un ambiente dinamico ed internazionale.

Oltre al Prof. Luigi Colangeli, desidero ringraziare il Prof. Pasquale Palumbo dell'Università Parthenope che in questi tre anni di attività di ricerca mi ha seguito con interesse spronandomi nello studio e nella caratterizzazione dello strumento HRIC.

Desidero, poi, ringraziare tutti i colleghi del Laboratorio di Fisica Cosmica e Planetologia dell'Osservatorio Astronomico di Capodimonte per il loro supporto (anche morale) in questi tre anni di vita e lavoro vissuti assieme.

Infine, volgo un pensiero anche alla mia famiglia che, forse anche per la lontananza, mi è stata sempre particolarmente vicina nei momenti di gioia e di difficoltà.